

Alma Mater Studiorum Università di Bologna
Archivio istituzionale della ricerca

Polarons in materials

This is the final peer-reviewed author's accepted manuscript (postprint) of the following publication:

Published Version:

Franchini C., Reticioli M., Setvin M., Diebold U. (2021). Polarons in materials. NATURE REVIEWS. MATERIALS, 6(7), 560-586 [10.1038/s41578-021-00289-w].

Availability:

This version is available at: <https://hdl.handle.net/11585/854883> since: 2022-02-10

Published:

DOI: <http://doi.org/10.1038/s41578-021-00289-w>

Terms of use:

Some rights reserved. The terms and conditions for the reuse of this version of the manuscript are specified in the publishing policy. For all terms of use and more information see the publisher's website.

This item was downloaded from IRIS Università di Bologna (<https://cris.unibo.it/>).
When citing, please refer to the published version.

(Article begins on next page)

This is the final peer-reviewed accepted manuscript of:

Franchini, C., Reticcioli, M., Setvin, M. et al. Polarons in materials. Nat Rev Mater 6, 560–586 (2021).

The final published version is available online at: <https://doi.org/10.1038/s41578-021-00289-w>

Terms of use:

Some rights reserved. The terms and conditions for the reuse of this version of the manuscript are specified in the publishing policy. For all terms of use and more information see the publisher's website.

This item was downloaded from IRIS Università di Bologna (<https://cris.unibo.it/>)

When citing, please refer to the published version.

Polarons in Materials

Cesare Franchini^{1,2,*}, Michele Retliccioli¹, Martin Setvin^{3,4}, and Ulrike Diebold³

¹University of Vienna, Faculty of Physics and Center for Computational Materials Science, A-1190 Vienna, Austria

²Department of Physics and Astronomy, Alma Mater Studiorum - Università di Bologna, Bologna, 40127 Italy

³Institute of Applied Physics, TU Wien, Wiedner Hauptstrasse 8-10/134, A 1040 Vienna, Austria

⁴Department of Surface and Plasma Science, Faculty of Mathematics and Physics, Charles University, V Holešovičkách 2, 180 00 Prague 8, Czech Republic

*e-mail: cesare.franchini@univie.ac.at

ABSTRACT

Polarons are quasiparticles that easily form in polarizable materials due to the coupling of excess electrons or holes with ionic vibrations. Polarons manifest themselves in many different ways and have a profound impact on materials properties and functionalities. As one of the most studied subject in physics, chemistry and material science, polarons have been the testing ground for the development of numerous theories, and their manifestations have been studied by many different experimental probes. This review aims to provide a map of the enormous amount of data and knowledge accumulated on polaron effects in materials, ranging from early studies and standard treatments to emerging experimental techniques and novel theoretical and computational approaches.

Introduction

Polarons are among the most studied and cross-disciplinary research subject in physics, chemistry and material sciences¹⁻³. The term polaron was coined by Solomon Pekar in 1946 to define the unit formed by an excess charge carrier (electron or hole) localized within a potential well, self-generated by displacing the surrounding ions^{4,5}. The resulting composite quantum object can be identified as a quasiparticle consisting of an electron or hole dressed by a cloud of virtual phonons: excess charge injected into a polarizable solid displaces the ions in its neighborhood and creates a polarization cloud that follows the charge carrier as it propagates through the crystal [see Fig. 1(a)]. Depending on the spatial extent of this polarization cloud, a general classification into small and large polarons can be made, whose different nature and properties originate from the range of action of the electron-phonon interaction. The distinct physical properties of small and large polarons are summarized in Box 1.

The concept of auto-localization in an ideally perfect crystal caused by lattice deformation was initially conceptualized by L.D. Landau in 1933⁶. Since then, several groundbreaking theories and experimental observations have gradually disclosed and described the importance of polaron formation in an exceptionally wide spectrum of systems including solids, liquids, polymers and cold gases¹. The development of polaron theories has its roots in the seminal works of Fröhlich⁷⁻⁹ and Holstein^{10,11}, who formalized the dichotomy between large-radius and small-radius polaronic states by establishing rigorous quantum-field Hamiltonians, which became the standard theoretical groundwork for successive advancements¹²⁻¹⁴ (for an overview see Tab. 1).

In parallel with continued theoretical progress, experimental evidence is rapidly accumulating that shows the pervasiveness of polarons in materials, and their key role in many different phenomena¹⁵. Polaron hallmarks have been measured in transition metal oxides^{3,16,17}, amorphous compounds¹⁸, organic semiconductors^{19,20}, conducting polymers²¹⁻²³, diluted magnetic semiconductors²⁴, manganites²⁵⁻²⁸, cuprates²⁹, hybrid perovskites^{30,31} and 2D materials³²⁻³⁴. Polaron-mediated effects have been identified as the key factor in physical phenomena such as charge transport^{19,35-37}, surface reactivity³⁸⁻⁴², colossal magnetoresistance^{25,43}, superconductivity^{44,45}, thermoelectricity⁴⁶, photoemission^{30,31,47}, and (multi)ferroism^{31,48} to name just the most relevant ones.

These achievements were made possible through innovations and improvements of experimental probes and computational approaches. Today, the presence of polarons in materials can be detected by a variety of experimental techniques including Scanning Tunneling Microscopy/Spectroscopy (STM/STS)⁴⁹ and Atomic Force Microscopy (AFM)⁵⁰, Angle Resolved Photoemission Spectroscopy (ARPES)⁵¹, various core level spectroscopies⁵², Electron Paramagnetic Resonance (EPR)^{53,54}, Raman scattering⁵⁵, muon spin relaxation⁵⁶, neutron scattering²⁸, luminescence⁵⁷, Infrared (IR) Spectroscopy⁵⁸, Time-Resolved Optical Kerr Effect (TR-OKE) spectroscopy³¹, transport measurements¹⁷, and many more (for an overview see Tab. 3).

On the other hand, the efficient implementation of polaron theories in computational codes has allowed the calculation of polaron-specific properties (polaron energy, polaron dispersion and effective mass, polaron wave function and polaron mobility, to name just a few, see Fig. 1) using a variety of approaches including analytical schemes^{59,60}, quantum Monte Carlo⁶¹⁻⁶³,

first principles density functional theory (DFT, and beyond)^{3,64–67}, dynamical mean-field theory (DMFT)^{68–70}, and multiscale modelling^{71,72}. A recent, rigorous *ab initio* computational theory of polarons developed by Giustino and colleagues combines the Landau-Pekar model with DFT^{14,73}.

After almost 90 years of polaron research, the concept of polarons continues to thrive and expand into new fundamental and applied areas^{31,33,35,41,44,45,47,48,50,60,67,74–85}. With this review we aim to provide an up-to-date survey of the historical milestones and a selection of the rapid contemporary developments from a joint theoretical and experimental perspective. We try to provide a comprehensive map of the theoretical models and experimental techniques, and present several paradigmatic examples of the different types of polarons and polaron-driven phenomena that can develop in materials. The primary focus is on small and large polarons, but we widen the context by including also other types such as bipolarons, magnetic polarons, Jahn-Teller/ferroelectric polarons and Zener polarons. Among the many materials discussed in this review, additional emphasis is given to TiO₂ and halide perovskites for the following reasons. For TiO₂ a vast number of solid data is available in literature, spanning roughly the last two decades, from the seminal first principles and EPR works of Pacchioni and Giamello^{53,64} to the most recent advances^{39,41,47,51,58,86–93}, some of which were conducted jointly by the authors of this review^{3,40,42,49,94–96}. Halide perovskites, on the other hand, represent the most rapidly developing research area where polarons play an essential role, and where many (even fundamental) aspects are the source of animated debates. At the end we discuss future perspectives on how to further improve the characterization and modelling of polarons, and suggest research directions to investigate novel polaronic effects in realistic systems.

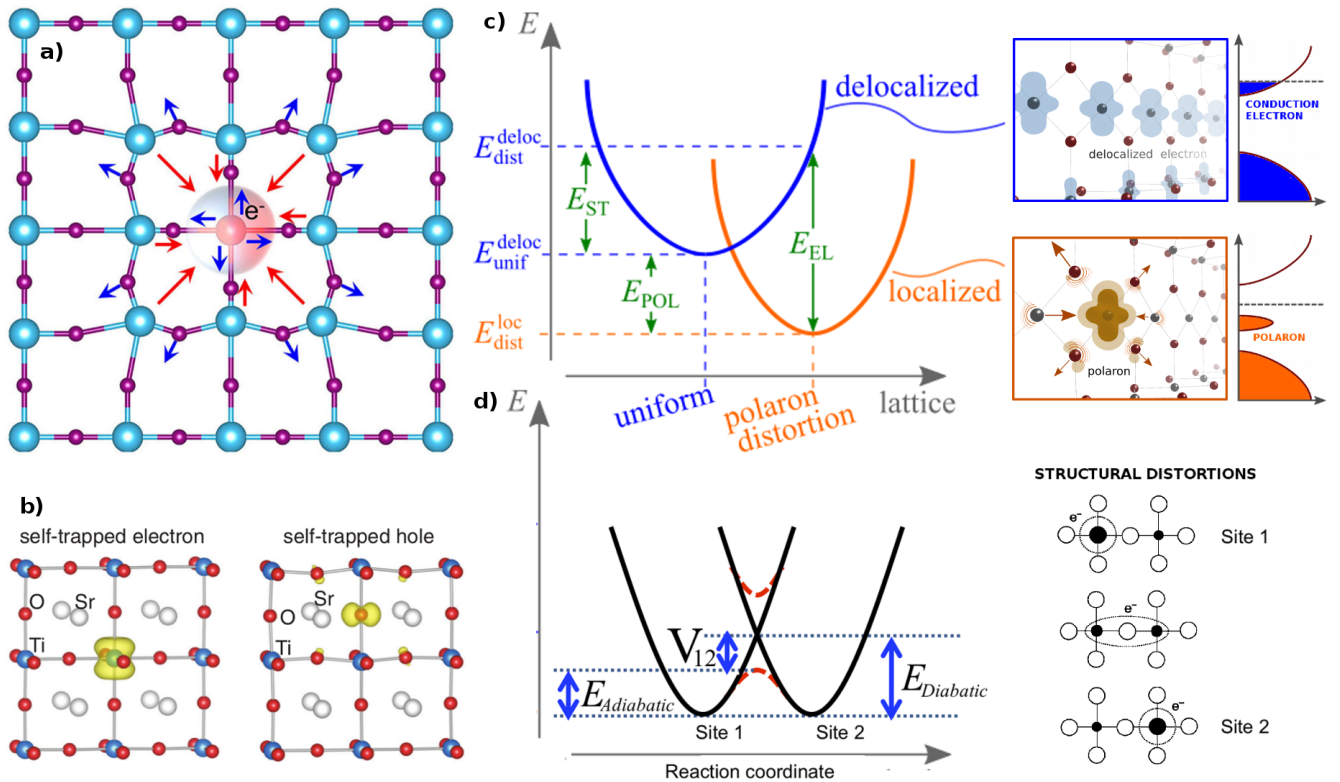


Figure 1. Pictorial representation of the basic properties of polarons. a | Schematic illustration of the polarization caused by the self-trapping of an electron at a lattice site and formation of a (small) polaron. Arrows represent attractive and repulsive forces (adapted from Ref. 35). b | Electron and hole polaron charge isosurfaces in SrTiO₃ (From Ref. 91). c | Configuration coordinate diagram depicting the energy balance (Structural Energy: E_{ST} ; Polaron Binding Energy: E_{POL} ; Electronic Energy: E_{EL}) as a function of lattice distortion for a conduction (delocalized) electron and for a localized polaron (adapted from Ref. 3). d | Charge density isosurfaces and corresponding schematic band structure of (upper panel) a delocalized conduction electron and (lower panel) a small polaron with the polaron peak localized below the Fermi Energy. d | General scheme of the Marcus-Emin-Holstein-Austin-Mott small polaron hopping theory showing the transfer of an electron from Site 1 to Site 2 via diabatic (finite electronic coupling strength V_{12}) or adiabatic (quantum tunneling) regime (adapted from Ref. 97 and 98.)

Theoretical account of polaron properties

This section provides a brief overview of the theoretical constructs and computational models developed in the last 90 years to describe, interpret and compute the properties of polarons loosely following a chronological order from the classical work of Landau to the *ab initio* theory of polarons (schematized in Tab. 1).

Theoretical models and computational approaches		
Year	Theoretical and Computational models	Polaron properties
1933 ⁶	Dielectric theory: charge moving in a dielectric crystal	Auto-localization due to lattice deformation
1946-1948 ^{4,99-101}	Self-consistent theory of a large polaron <i>Landau-Pekar model</i>	Enhancement of effective mass Localization of the wave function
1950 ^{7-9,102,103}	Quantum-mechanical variational theory of large polarons <i>Fröhlich large polaron Hamiltonian</i> (continuum approx.)	Effective mass, energy, mobility Intermediate electron-phonon interaction
1955-2017 ^{12,13,104-106}	All-coupling continuum polaron theory <i>Feynman variational path-integral formalism</i>	Energy, effective mass, mobility (large polaron)
1956 ¹⁰⁷ , 1980 ^{108,109}	Monte Carlo calculations	Large polaron ground-state energy
1958 ^{110,111} , 1959 ^{10,11}	'Holstein' small polaron theory <i>Holstein small polaron Hamiltonian</i> (lattice approx.)	Small polaron conduction mechanism Effective mass, energy
1963-2000 ¹¹²⁻¹¹⁵	Exact solution of the two-site Holstein polaron	dynamical characteristics
1969 ¹¹⁶ , 2000 ^{117,118}	<i>Emin-Holstein-Austin-Mott theory</i>	small polaron hopping
1980 ¹¹⁹ , 1985 ^{120,121}	<i>Marcus Theory</i>	Polaron hopping
1994 ¹²²	Exact diagonalization	Small polaron frequencies
1997 ¹²³	Hartree-Fock	Small polaron density of states
1998-2000 ^{61,62}	Diagrammatic Monte Carlo	Energy, effective mass, phonon distribution, spectral density
1999 ¹²⁴	random walk Monte Carlo	dispersive transport and recombination
2001 ¹²⁵ , 2010 ⁵⁹	Analytical variational approach (variational LDB many-polaron wave function ¹²⁶)	Many-polaron (large) optical conductivity
2001 ⁶³	Path-integral Monte Carlo	Large polaron energy (2D & 3D)
1995 ⁶⁸ , 1997 ⁶⁹ , 2003 ⁷⁰	Dynamical mean-field theory	small polaron energy, mass, spectral and transport properties
2000 ¹²⁷ , 2018 ⁹⁵	First principles molecular dynamics of small polarons	polaron configurations
2002 ⁶⁴ , 2006 ¹²⁸	Hybrid functionals	Small polaron spin density
2006 ¹²⁹	Analytical approximation for the Green's function	Energy, mass, dispersion, spectral weight
2006 ^{130,131} , 2009 ¹³²	DFT+U	Small polaron migration, DOS, bipolaron
2007-2010 ^{71,72}	Multiscale modelling-Kinetic Monte Carlo	charge transport
2014 ¹³³	Random Phase Approximation	small energy and hopping
2009 ⁶⁵ , 2011 ¹³⁴	Generalized Koopmans density functional	small polarons states
2015 ⁶⁷	Density-functional perturbation theory	Fröhlich electron-phonon vertex
2016 ¹³⁵	Renormalization group (large polaron)	Energy, effective mass
2019 ^{14,73}	<i>Ab initio</i> theory of polarons	Formation & excitation energies wave function (small & large polarons)

Table 1. Compendium of theoretical and computational models for studying polarons.

Pekar-Landau Model

Inspired by the seminal elaboration of Landau on an electronic carrier slowly moving through an ionic solid⁶ the first quantitative description of a single electron immersed in a dielectric medium was developed by Pekar⁴. The resulting Landau-Pekar (LP) model relies on the *continuum* approximation, where the ionic crystal is treated as a polarizable dielectric continuum, and the electron-electron interaction is treated within the effective-mass approximation. The main (Schrödinger-type) equation of the LP model is derived by minimizing the total LP energy functional $E(\psi)$ with respect to the polaron wave function $\psi(\mathbf{r})$ ¹:

$$\left(-\frac{\nabla^2}{2m} - e^2 \left(\frac{1}{\epsilon_\infty} - \frac{1}{\epsilon_0} \right) \int d\mathbf{r}' \frac{|\psi(\mathbf{r}')|^2}{|\mathbf{r}' - \mathbf{r}|} \right) \psi(\mathbf{r}) = E_0 \psi(\mathbf{r}) \quad (1)$$

where m is the band mass, and ϵ_0 and ϵ_∞ are the static (electronic and ionic) and high-frequency (electronic, ion-clamped) dielectric constants. Despite its simplicity, this model provides a ready-to-use formula to estimate the polaron ground state energy, the polaron radius (spatial extension of the polaron wavefunction) and the polaron effective mass, also representable in term of the dimensionless electron-phonon interaction α :

$$\alpha = e^2 \left(\frac{1}{\epsilon_\infty} - \frac{1}{\epsilon_0} \right) \sqrt{\frac{m}{2\omega_0}} \quad (2)$$

where ω_0 represents the characteristic longitudinal optical phonon frequency (acoustic phonons are not considered). However, an intrinsic contradiction restricts the applicability of the Landau-Pekar model: it is designed to treat continuum Fröhlich polarons but formally justified results can only be obtained in the strong electron-phonon coupling regime, where the polaron radius is small, a situation hardly realizable in realistic materials^{1,14}. Also, for a bound polaron solution, the electron-phonon coupling α must be positive. This implies $\epsilon_0 > \epsilon_\infty$. The LP model is thus only applicable to polar crystal, but polarons also exist in non-polar crystals. In this respect the term 'polaron' is a misnomer and does not reflect the correct nature of this quasiparticle.

In 2019 Giustino and coworkers have recasted the LP equations in a DFT formalism with a Bethe-Salpeter formalism^{14,73} and showed that the resulting (variational) first principles theory of polarons overcomes the limitations of the original LP model. It allows for a material specific description of *small* and *large* polarons within a unified formalism, taking into account the coupling with both acoustic and optical phonons¹⁴ and treating both short-range and long-range electron-phonon interaction (an example of the calculated small and large polaron wavefunction is given in Box. 1).

Historically, the models describing polarons are usually divided into two classes and are based on the original theories of Fröhlich^{7,102,103} (continuum large polarons) and Holstein^{10,11} (lattice small polarons), which are succinctly reviewed in the next section.

Holstein & Fröhlich Hamiltonians

The Fröhlich and Holstein models constitute the historical backbone of polaron theory. The Fröhlich approach follows the continuum approximation and neglects the discreteness of the crystal lattice. It allows the description of large polarons in ionic, polar and ferroelectric materials, caused by the long-range component of the electron-phonon interaction. In these materials, the static dielectric constant ϵ_0 is necessarily larger than the high-frequency (optical) ϵ_∞ , implying that the Fröhlich model is not formally applicable to non-polar systems, similarly to Pekar's model. The Holstein theory, on the other hand, considers short-range electron-phonon interactions resulting from the coupling between a carrier and the strain where it resides. This model explicitly takes into account the discreteness of the lattice. In principle it can describe polarons with different spatial extension; as such it is suitable to describe strongly coupled small and large polarons. The Fröhlich and Holstein theories are formalized in terms of the fundamental effective Hamiltonians given in Box 1 (equation B1 and B2), where the various terms (electronic bands, phonons and electron-phonon coupling) are typically treated by means of approximate parametric expressions (i.e. non *ab initio*).

All attempts to find exact solutions for the Fröhlich model have been fruitless, and the Holstein model can be solved exactly only in the two-sites case^{112,114,115}; analytical and numerical solutions are unavoidable. Extensive studies have been devoted to solving and understanding the properties of small and large polarons at all coupling strengths (weak, intermediate and strong)^{1,136}. These are summarized in Table 1 and briefly recapped below. The first groundbreaking and influential approach was the Feynman variational path-integral formalism for the large polaron introduced in 1955¹² and, among the various many-body propositions, the diagrammatic Monte Carlo⁶¹ method turned out to be an efficient and accurate scheme to solve both the Holstein and Fröhlich Hamiltonians^{62,129,137}.

Feynman's path-integral approach

In analogy with quantum electrodynamics Feynman reformulated the polaron problem into a variational path-integration for a system composed of an excess charge carrier coupled with a cloud of independent phonons through a harmonic interaction.

Starting from a polaron Lagrangian, Feynmann integrated the phonon field to obtain an effective Euclidean polaron action $S[\mathbf{r}(t)]$, which includes retardation effects (i.e. non-local in time) arising from interaction of the electron with the phonon disturbance it has previously created in travelling through the lattice (which exponentially dies out in time). Within this model, the free energy F of the polaron system at finite temperature $k_B T = 1/\beta$ can be expressed as a path integral of the form

$$e^{-\beta F} = \int \mathcal{D}\mathbf{r}(t) e^S, \quad (3)$$

where \mathcal{D} denotes integration over all paths. In order to solve this electron path integral analytically Feynman has employed an original variational principle, in which the exact polaron action was replaced by an approximate, but exactly solvable, quadratic

action dependent on two model parameters. These parameters are then varied to minimize the ground state energy, for a given α and phonon frequency.¹²

This path-integrated harmonic model provides one of the most accurate analytical approximations for the ground-state energy and effective mass of the Fröhlich polaron for all coupling strengths α ^{1,105}. The integral cannot be performed in closed form but it is possible to obtain approximate expressions in the weak and strong coupling limit, which for the ground-state energy E_0 and effective mass m^* takes the forms:

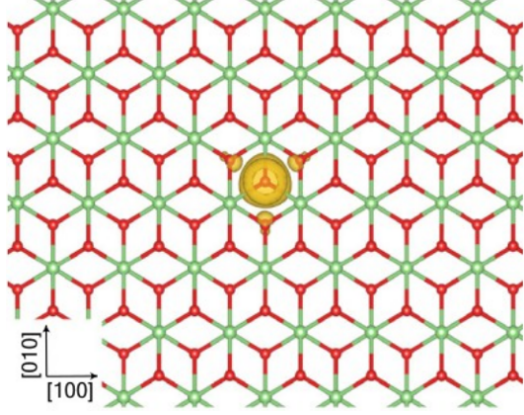
$$\frac{E_0}{\omega_0} = \begin{cases} -\alpha - 0.0123\alpha^2 + O(\alpha^3) & \alpha \rightarrow 0 \\ -0.106\alpha^2 + O(1) & \alpha \rightarrow \infty \end{cases} \quad (4)$$

$$\frac{m^*}{m} = \begin{cases} 2 + \frac{\alpha}{6} + O(\alpha^2) & \alpha \rightarrow 0 \\ 0.106\alpha^4 + \dots & \alpha \rightarrow \infty \end{cases} \quad (5)$$

An accurate solution of the Feynman integral requires numerical integration, which can be executed by means of Monte Carlo (MC) techniques^{63,107–109}. Figure 2(a) shows the MC-derived evolution of polaron ground state energy and effective mass as a function of α for the large Fröhlich polaron, compared to recent data obtained by Diagrammatic MC scheme (DiagMC)⁶¹, one of the most successful scheme to solve different types of (single and multiple) polaron problems^{62,83,137,138}. The basic idea behind DiagMC are discussed below.

Small "Holstein" Polarons

$$H = \sum_{\mathbf{k}} \epsilon_{\mathbf{k}} \hat{c}_{\mathbf{k}}^{\dagger} \hat{c}_{\mathbf{k}} + \hbar \omega_0 \sum_{\mathbf{q}} \hat{a}_{\mathbf{q}}^{\dagger} \hat{a}_{\mathbf{q}} + \frac{g}{\sqrt{N}} \sum_{\mathbf{k}, \mathbf{q}} \hat{c}_{\mathbf{k}+\mathbf{q}}^{\dagger} \hat{c}_{\mathbf{k}} (\hat{a}_{\mathbf{q}} + \hat{a}_{-\mathbf{q}}^{\dagger})$$



Short-range electron-phonon interaction

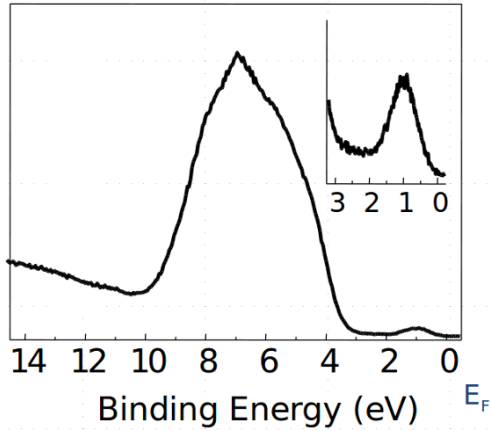
Polaron radius \approx lattice parameter

Narrow mid-gap electronic state (≈ 1 eV below E_F)

Incoherent motion (phonon assisted)

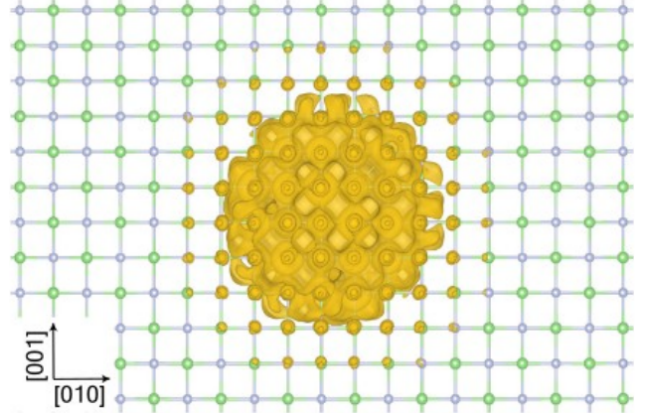
Thermally activated hopping mobility $\mu \ll 1 \text{ cm}^2(\text{Vs})^{-1}$

Mobility increasing with temperature



Large "Fröhlich" Polarons

$$H = \sum_{\mathbf{k}} \epsilon_{\mathbf{k}} \hat{c}_{\mathbf{k}}^{\dagger} \hat{c}_{\mathbf{k}} + \hbar \omega_0 \sum_{\mathbf{q}} \hat{a}_{\mathbf{q}}^{\dagger} \hat{a}_{\mathbf{q}} + \sum_{\mathbf{k}, \mathbf{q}} V(\mathbf{q}) \hat{c}_{\mathbf{k}+\mathbf{q}}^{\dagger} \hat{c}_{\mathbf{k}} (\hat{a}_{\mathbf{q}} + \hat{a}_{-\mathbf{q}}^{\dagger})$$



Long range electron-phonon interaction

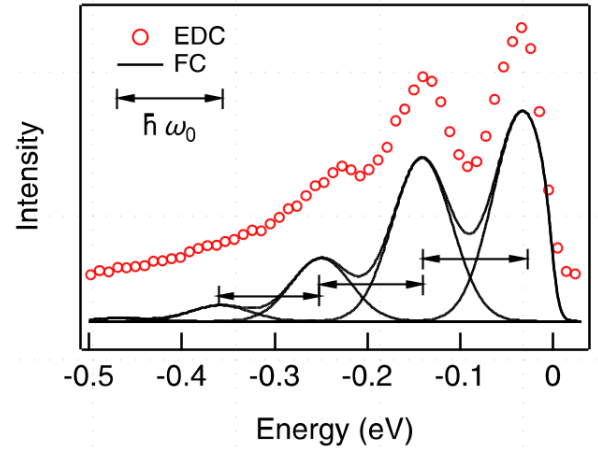
Polaron radius \gg lattice parameter

Shallow electronic state (≈ 10 meV below E_F)

Coherent motion

Free carrier mobility $\gg 1 \text{ cm}^2(\text{Vs})^{-1}$

Mobility decreasing with temperature



BOX1: Basic characteristics of small and large polarons. From top to bottom: effective Holstein and Fröhlich Hamiltonians [$c_{\mathbf{k}}$ and $a_{\mathbf{q}}$ are annihilation operators for a particle with wave vector \mathbf{k} and a phonon with wave vector \mathbf{q} , respectively, $\epsilon_{\mathbf{k}}$ represent the band energies, N is the total number of unit cells, whereas g and $V(\mathbf{q}) = \left(\frac{2\sqrt{2}\pi\alpha}{V} \right)^{\frac{1}{2}} \frac{1}{q} \left(\frac{\hbar^5 \omega_0^3}{m} \right)^{\frac{1}{4}}$ are the short- and long-range electron-phonon coupling terms, the latter given in terms of the volume of the system V and of the electron-phonon parameter α (Eq. 2)]; charge isosurface of a small polaron in Li_2O and a large polaron in LiF (adapted from Ref. 73); characteristic features and properties of small and large polarons; valence band photoemission spectra of a small polaron in reduced rutile TiO_2 (taken from Ref. 139) and an energy distribution curve (EDC) of a large polaron in n -doped anatase TiO_2 measured Ref. 51 (FC = Frank-Condon line shape), note the different energy scales.)

Diagrammatic Monte Carlo

The Diagrammatic Monte Carlo method is a type of quantum Monte Carlo method for strongly correlated systems based on the stochastic sampling of Feynman diagrams^{61,140}. Feynman diagrams are a powerful tool in many-body physics which appear in perturbative expansions of quantum statistical averages. From a mathematical point of view, diagrammatic expansion of a function of interest $Q(\{y\})$ (typically a Green's function) is a series of integrals of the type

$$Q(\{y\}) = \sum_{n=0}^{\infty} \sum_{\xi_n} \int \cdots \int \mathcal{D}_{n,\xi_n}(\{y\}; x_1, \dots, x_n) dx_1 \dots dx_n, \quad (6)$$

where n labels the order of the perturbation (potentially infinite), $\{y\}$ are external parameters, ξ_n indexes different diagrams of the same order n and the x 's are the integration variables.

The overall idea behind the DiagMC method is to represent the functions \mathcal{D} by Feynman graphs and interpret $Q(\{y\})$ as a distribution function for the external variables $\{y\}$ ⁶¹. The whole space of Feynman diagrams are generated stochastically using a standard Markov chain MC and a Metropolis-Hastings update scheme^{61,62,141}.

To solve the polaron problem, the DiagMC procedure is applied to the perturbative expansion of the one-electron-N-phonon Green's function used to solve a general polaron Hamiltonian (e.g. Eqs. B1 and B2), by mapping the function $Q(\{y\})$ into the polaron Green's function $G^{(N)}$:

$$G^{(N)}(\mathbf{k}, \tau, \{\tilde{\mathbf{q}}_i\}) = \sum_{n=0}^{\infty} \sum_{\xi_n} \int \cdots \int \mathcal{D}_{n,\xi_n}(\mathbf{k}, \tau, \{\tilde{\mathbf{q}}_i\}; \mathbf{x}) d\mathbf{x}, \quad (7)$$

where \mathbf{k} is the wave vector and $\mathbf{x} = (\tau_1, \dots, \tau_n, \mathbf{q}_1, \dots, \mathbf{q}_k)$ is a vector of integration variables (times of interaction vertices and internal phonon wave vectors). The integrands \mathcal{D}_{n,ξ_n} are given as a product of free electron Green's functions, free phonon Green's functions and squared electron-phonon interaction vertices, and are clearly representable by a series of Feynman diagrams.

Equation 7 represents therefore a conventional diagrammatic expansion for the polaron Green function, which can be efficiently calculated by DiagMC. In the original formulation, the lowest energy eigenvalues $E_0(k, \alpha)$ (polaron spectrum) are obtained through an exponential fit of the asymptotic behavior of the Green's function at long imaginary times:

$$G^{(N)}(\mathbf{k}, \tau \rightarrow \infty, \{\tilde{\mathbf{q}}_i\}) \propto e^{-E_0(\mathbf{k})\tau}. \quad (8)$$

Other polaron quantities of interest can be calculated in the framework of quantum DiagMC including effective mass, self-energy, mobility⁸³ and spectral function¹⁴². An example of the application of DiagMC to the Fröhlich and Holstein polaron is provided in Fig. 2(a-b), showing the polaron dispersion and the polaron effective mass as a function of the electron-phonon coupling strength, which includes a direct comparison with Feynman path-integral approach and a few other analytical approximations.

From model phonon Hamiltonians to first principles

Besides DiagMC, other sophisticated approaches have been adopted to solve the Fröhlich and Holstein Hamiltonians. Noteworthy are the fundamental studies by Ciuchi and coworkers using the dynamical mean-field theory (DMFT)^{63,68–70} [an example of DMFT-derived results is the temperature-dependent resistivity for a small polaron displayed in Fig. 2(d) showing the crossover from classical activated motion at high temperatures to coherent motion at low temperatures], exact diagonalization¹²², renormalization group¹³⁵, and many important analytical studies, not only those mentioned in relation to Fig. 2(b) but also other models such as those inspired by the variation method of Lemmens, Devreese, and Brosens for many-polaron systems^{59,60,125,126}. A representative illustration of the predictive power of (semi)analytical methods is shown in Fig. 2(c), where the measured optical conductivity for n -doped SrTiO₃ is compared with memory-function results of Klimin and colleagues⁶⁰ (here combined with first principles inputs).

Numerical and analytical solvers are powerful and versatile approaches and can allow for the inclusion of many-body effects (DiagMC, DMFT, etc.). However, a direct comparison with material-specific experimental data is often hindered by the intrinsic limitations of effective Hamiltonians approaches, namely the parametric or phenomenological treatment of the individual physical terms of the Hamiltonian: (i) the *single particle band structure*, (ii) the *full phonon dispersion* and (iii) the *electron-phonon interaction*. The Fröhlich and Holstein model Hamiltonians are simplifications of the more general electron-phonon Hamiltonian, and these terms are treated in an approximate way. In the Fröhlich model the one-particle band energies are replaced by a model parabolic dispersion, the phonon terms involve a single dispersion free phonon mode, which is coupled with the wave vector dependent coupling term $V(\mathbf{q})$ (dependent on the coupling parameter α). Similarly, the Holstein model involves a single local mode and the local displacement couples (through the trivial coupling term q) to the electronic

bands, typically described within a tight-binding picture. A natural improvement (albeit of great complexity) would be the extension to many electron and phonon bands and a realistic account of all terms including the short-range and long-range electron-phonon interaction. From a numerical perspective all these contributions can be calculated by first principles methods: the energy bands can be computed accurately within the GW approximation^{143,144} (a reasonable compromise are also hybrid functionals^{145,146} or the DFT+U method^{147,148}), whereas phonon properties including electron-phonon interactions can be estimated by density functional perturbation theory^{149,150}, including the Fröhlich term⁶⁷. Also properties such as the spectral function, a natural output of diagrammatic Monte Carlo⁶², can be mapped to first principles techniques as shown by Nery *et al.*⁷⁹ using cumulant expansion.

The time is ripe to develop new techniques and numerical procedures to combine first principles methods with quantum-field phonon Hamiltonians, merging the distinct benefits of each approach into a general realistic many-body quantum framework allowing for a truly complete first-principles calculations of polarons.

To complete the overview of the theoretical approach, we summarize a few aspects of first principles methods for polarons in the next section.

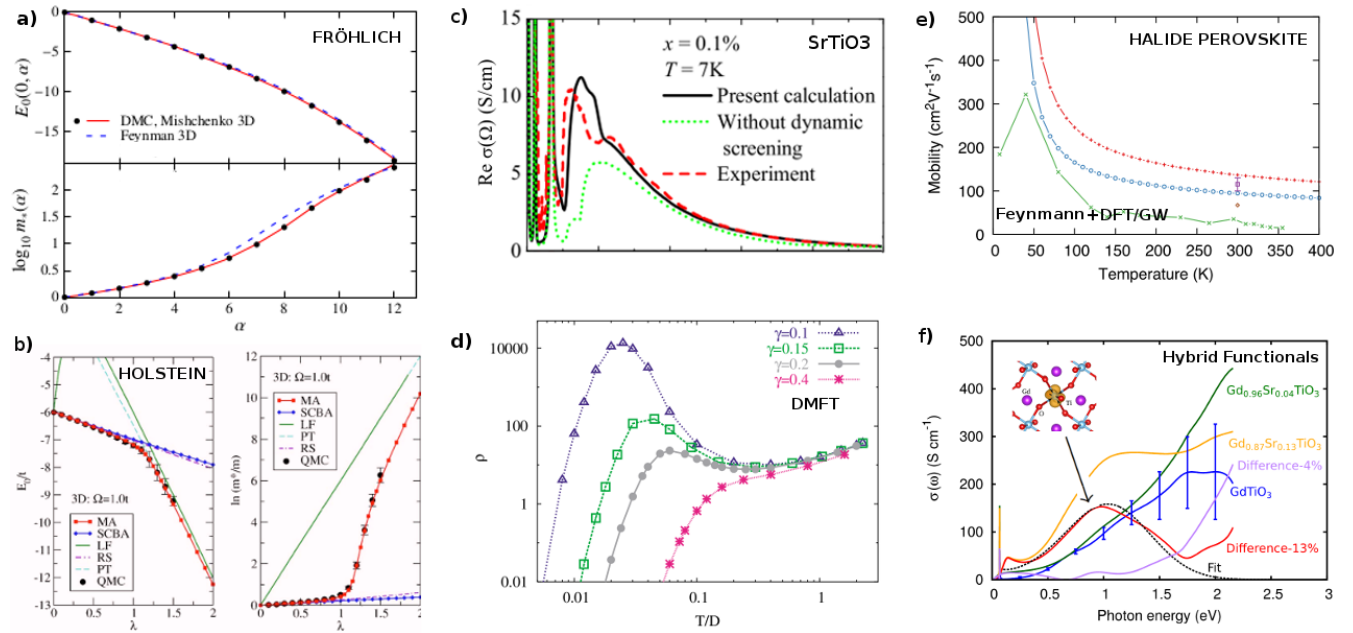


Figure 2. Polaron-specific properties predicted by different theoretical and computational models Selected examples of predicted polaron quantities. a & b | Diagrammatic Montecarlo: effective mass and ground state energy for the large (Fröhlich polaron, compared with MC data¹⁰⁵) and small (Holstein, QMC) polaron (adapted from Ref. 137 and Ref. 129). Holstein's data are compared to other analytical techniques: momentum average (MA) approximation, self-consistent Born approximation (SCBA), Lang-Firsov (LF) expression, Rayleigh-Schrödinger (RS) perturbation theory and second order perturbation theory (PT) (see Ref. 129 and references therein). c | Analytical dielectric function approach: comparison between measured and calculated optical conductivity in *n*-doped STiO₃ (including comparison with experiment, adapted from Ref. 60). d | DMFT: temperature-dependent resistivity for different degree of adiabaticity γ within the Holstein model (adapted from Ref. 70). e | Feynman variational method (parameter-free, inputs opbatined by GW and DFT calculations): temperature-dependent large polaron mobility in Methylammonium lead iodide perovskite (including comparison with experiment: crosses, diamond and square), adapted from Ref. 106. f | First principles (hybrid functionals): effects of hole small polaron in the optical conductivity of Gd_{1-x}Sr_xTiO₃ showing the onset of an polaron peak: theory (fit) compared to experiment (red: difference between the spectra at $x = 0$ and $x = 0.13$); adapted from Ref. 151.

First principles: DFT and beyond

Most electronic structure schemes used to study polaron properties in real materials have their roots in Kohn–Sham (KS) DFT, where the many-body interactions are embedded into an approximated exchange-correlation (xc) functional within a mean-field

fashion¹⁵², resulting in a system of single-particle Schrödinger equations:

$$\left(-\frac{1}{2}\Delta + V_{\text{ext}}(\mathbf{r}) + V_H(\mathbf{r}) + V_c(\mathbf{r}) + V_x(\mathbf{r})\right)\phi_i(\mathbf{r}) = \varepsilon_i\phi_i(\mathbf{r}) \quad (9)$$

where the Hamiltonian is split into kinetic, Hartree (V_H), External (V_{ext}), and exchange-correlation (V_x and V_c) terms, $\phi_i(\mathbf{r})$ are the single-particle KS orbitals and ε_i the corresponding eigenvalues.

Despite its great success^{153,154}, DFT within the simplest local (LDA) and semi-local (GGA) functionals exhibits systematic failures due to self-interactions errors, manifested by the wrong variation of the energy functional E as a function of the orbital occupation n ($d^2E/dn_i^2 > 0$ instead of the correct $d^2E/dn_i^2 = 0$ behavior). These shortcomings are particularly substantial for the description of localized states and band gaps, two crucial quantities in polaron physics. To attenuate these difficulties different improvements have been proposed involving an orbital selective inclusion of additional electronic correlation or incorporating non-local terms in the xc functionals. The most widely used extensions of DFT, successfully used in the study of polaron properties, are the renowned DFT+U method¹⁴⁷ and generalized KS (GKS) schemes¹⁵⁵.

In DFT+U the DFT energy functional is corrected in the target correlated orbital space (typically the $l = 2$ manifold) by adding an on-site Hubbard U . The polaron formation energy can be computed as the difference between the localized (i.e. polaronic) and delocalized solution, as sketched in Fig. 1(c) (for more details see Ref. 3). The first applications of DFT+U to the polaron problem dates back to the mid 2000s, to study the formation of hole localization in Al-doped SiO_2 ¹³¹ and the migration of small polarons in olivine Li_xFePO_4 ¹³⁰. In these early studies, polaron hopping was described within the Marcus theory^{121,156}, where charge transfer occurs via tunneling from two independent Born-Oppenheimer surfaces around the initial and final polaron site [see Fig. 1(d)]. Alternative models to account for polaron mobility are briefly reviewed in the next section.

Since then, DFT+U has been adopted in many polaron studies yielding generally good agreement with observations^{49,98}. It should be noted, however, that the results (polaron energy, degree of localization, hopping barrier, energy levels, etc.) are typically highly sensitive on the choice of the U parameter^{49,97,157–159}, which is generally chosen by means of a fitting protocol (e.g., good match with the measured band gap). This degree of arbitrariness on the choice of U limits the predictive power of DFT+U and validation with experimental data is vital for achieving a proper account of polaron properties. To cure the parametric-nature of this scheme a few prescriptions have been proposed to compute U values entirely ab initio, such as the Cococcioni scheme¹⁶⁰ or the constrained Random Phase Approximation (cRPA)^{49,161}. These solutions lead to a parameter-free framework, but it should be considered that a single (orbital-selective) U correction is in some case not sufficient to account simultaneously for all ground state properties of a system (e.g. band gap, vacancy formation energy, volume, etc.). This limitation can be rectified by consistently acting on all orbitals with orbital-dependent single-particle corrections as done in the self-interaction correction method¹⁶² or, more commonly, adopting GKS.¹⁵⁵

In this GKS theory, the original interacting system is mapped into a *partially* interacting system. Hybrid functionals are arguably the most popular GKS scheme, and involve the replacement of a fraction of local (LDA/GGA) exchange with the exact Hartree-Fock (HF) form:

$$\left(-\frac{1}{2}\Delta + V_{\text{ext}}(\mathbf{r}) + V_H(\mathbf{r}) + V_c(\mathbf{r})\right)\phi_i(\mathbf{r}) + \int V_X^{\text{Hybrid}}(\mathbf{r},\mathbf{r}')\phi_i(\mathbf{r}')d\mathbf{r}' = \varepsilon_i\phi_i(\mathbf{r}) \quad (10)$$

where $V_X^{\text{Hybrid}}(\mathbf{r},\mathbf{r}')$ represents the non-local HF exchange that assume different forms depending on the specific hybrid recipe¹⁶³. Commonly used prescriptions are the PBE0/HSE and B3LYP hybrids, which have been applied for a wide range of polaron properties ranging from early works on defective TiO_2 ^{53,64} and doped quartz¹⁶⁴ to the interpretation of the optical conductivity in doped $\text{Gd}_{1-x}\text{Sr}_x\text{TiO}_3$ in terms of hole polaron induced features¹⁵¹ (see Fig. 2(f)). Alternative GKS schemes relies on a formal recovery of the correct $d^2E/dn_i^2 = 0$ linear behavior by means of on-site potential perturbations that removes the (de)localization bias intrinsic to DFT approximations, as done in the Lany-Zunger model^{65,92,134,165,166}.

An additional critical issue in DFT calculations using periodic boundary conditions (PBC) is the spurious self-interaction of the localized charge (polaron and, in general, point charge defects) with its periodic image. These finite size effects can be prevented by adopting large unit cells, typically with several hundreds of atoms, with large distance between point defects and images, at the cost of performing very demanding calculations. In order to alleviate the computational cost of this supercell approach, one could use progressively larger cells and extrapolate to the dilute limit, or implement *a posteriori* corrections¹⁶⁷, such as the one recently proposed by Kokott and colleagues, based on a proper account of long-range polarization effects⁶⁶. Alternatively to the PBC technique, polaron formation has been successfully studied by solid state embedding approaches, where a small cluster of atoms around the polaronic site is described at quantum mechanical level and embedded in a molecular mechanics (QM/MM) or polarizable continuum (QM/continuum) environment tuned to reproduce the long-range interactions of the crystal^{168–171}. This approach has the advantage to reduce the computational cost (as the QM cluster are typically smaller

than the supercells in PBC) and to completely remove the spurious interactions of the PBC technique; on the other hand, the results are very sensitive to the cluster size and shape, which dramatically influence the prediction of polaron properties^{172,173}.

It is important to note that also the already mentioned *ab initio* theory of polarons, combining the Pekar-Landau ansatz with DFT does not require supercells and the self-interaction problem is addressed by including a suitable self-interaction correction term in the standard DFT functional.^{14,73}

We complete this theoretical overview by addressing polaron transport and mobility.

Polaron mobility

In polaronic materials, charge transport is largely affected by polaron diffusion, which is of great fundamental and technological interest^{35,174}. Several diffusion mechanisms have been identified for both large and small polarons, with distinct regimes depending on temperature, strength of the electron-phonon coupling, electronic band width and characteristic phonon frequency^{70,83,175}. Despite this complex scenario, a simplified picture can be drawn to highlight the general tendencies of small and large polarons¹⁷⁶. Small polarons are likely to undergo phonon-assisted hopping, as the charge carrier localization is destabilized by the thermally-induced atomic distortions around the trapping site, resulting into occasional hops. This incoherent motion shows a mobility μ typically much smaller than $1 \text{ cm}^2(\text{V} \cdot \text{s})^{-1}$, which increases upon raising temperature, due to the enhanced thermal distortions. Conversely, large polarons tend to sustain a free-carrier-like coherent motion: The large effective mass of the large polarons determines a high mobility, as it preserves the polaron motion from occasional scattering with the phonon field; the mobility decreases by raising the temperature, since the scattering becomes more effective (see also Box 1 and Fig. 5).

Small polarons

Hopping mobility is typically studied in the framework of Marcus theory^{119–121}. The conceptual basis of this theory was settled in the 1980s and was further developed by Emin-Holstein-Austin-Mott (EHAM)^{116–118}. Both theories represent the initial and final polaron states with (parabolic) potential-energy surfaces [see Fig. 1(d)]⁹⁸. The associated electrical conductivity σ is expressed by the general form:

$$\sigma = \kappa e^{-\beta E_{\text{act}}}, \quad (11)$$

where the prefactor κ and the activation energy E_{act} assume different forms in the *adiabatic* and *non-adiabatic* (diabatic) regime. In the adiabatic regime, polarons move much faster than the phonon field, hence their propagation time is much smaller than that of the local lattice distortions; polarons hop via tunneling from site to site. Conversely, in the non-adiabatic regime, polarons move much slower than the lattice polarization, with a hopping frequency smaller than the corresponding phonon one. The activation energies and, to some extent, also the pre-factor can be calculated directly from first principles schemes defining specific polaron transfer pathway within nudged elastic band methods or linear interpolation schemes^{98,133}. A concise but detailed discussion of the Marcus and EHAM models can be found in Refs.^{35,98,177,178}.

Complementary insights on the motion of small polarons can be achieved by first principles molecular dynamics (FPMD)^{42,49,95,127}. FPMD allows to study the hopping dynamics of single and multiple small polaron systems at different temperatures and to extract the most favorable spatial polaron configurations⁹⁵. The analysis of the FPMD energy landscape with statistical tools allow to interpret the energy balance and work out the driving mechanisms favoring specific polaron configurations. The energy contributions essential in self-trapping processes are summarized in Fig. 1(c), and involve the energy cost to locally deform the lattice to accommodate an excess charge (so called structural energy E_{ST}) and the energy gain arising from the electron-phonon assisted charge-localization and formation of occupied mid-gap states (so called electronic energy E_{EL}). For multipolaron systems, the situation is complicated by the polaron-polaron interaction, which involves two effects: (i) direct Coulomb repulsion between like-charged quasiparticles and (ii) the interference of their atomic deformation patterns¹⁷⁹. To clarify the interaction between two adjacent polaron distortions let us consider the case of two like-charged polarons [Fig. 3(left)]. The polarons exert counteracting forces on the atoms between them, at large separation this interaction is repulsive. At short separation (approximately one lattice constant) it may become attractive as both polarons co-act to displace the surrounding ions into the same direction; if this attractive interaction is larger than the Coulomb repulsion of the two like-quasiparticles, the pair of small polarons may bind together forming a bipolaron. Applying a similar rationale to the case of oppositely charged polarons yields to the process schematized in Fig. 3(right); here increased short-range repulsion opposes electron-hole recombination.

We have already mentioned that small polaron hopping can be described within DMFT (see Fig. 2(d)), which allows the treatment of local many-body effects and the quantum nature of phonon and nicely describes the loss of coherence at high T⁷⁰ (see Fig. 2(d)). The full identification of the different regimes for the dynamic and static small polaron mobility as a function of α and T (band-like, incoherent metallic, hopping, and high-temperature saturation region) has been only recently achieved for the one dimensional Holstein model in the framework of DiagMC¹⁷⁵.

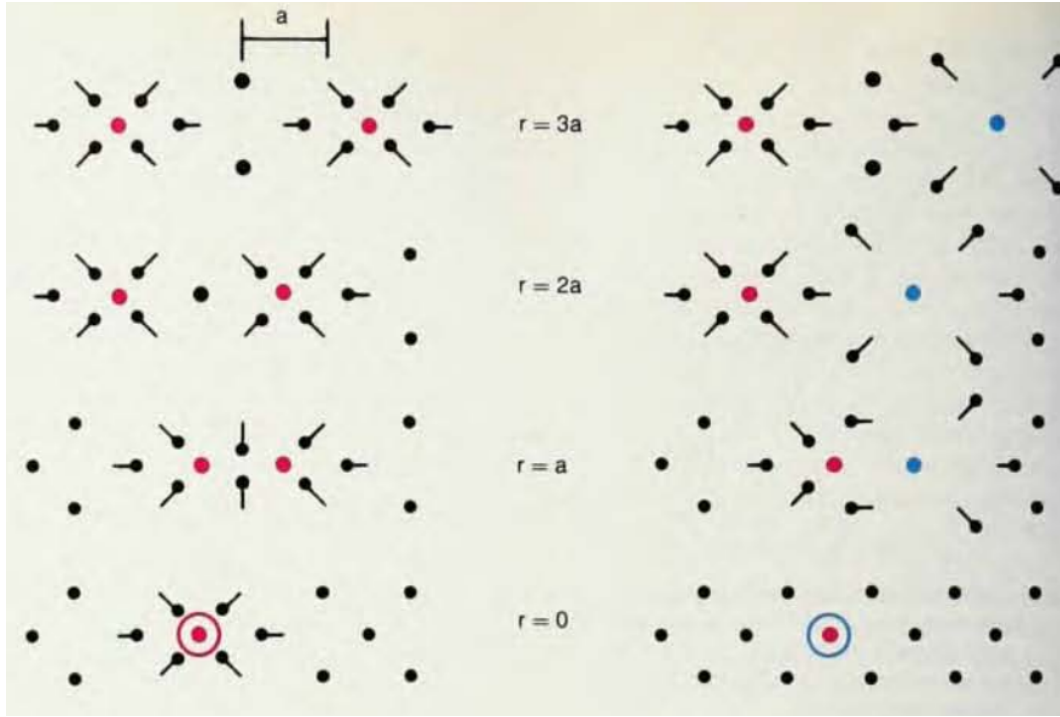


Figure 3. Interaction between two small polarons. (left) Interaction between like-charged polarons. By progressively reducing the interpolaron-distance the interaction between overlapping polaron deformation patterns transforms from repulsive to attracting. If this interference energy gain is larger than the Coulomb repulsion between like-charged polarons, the two polarons glue together, forming a bipolaron. (right) Interaction between hole and electron polarons. In this case, the short-range, repulsive overlap between the deformation patterns can strongly affect the recombinative properties (taken from Ref. 179).

Another approach for modeling polaron transfer and transport is continuous-time random walk combined with Monte Carlo simulations¹²⁴, particularly useful to describe dispersive transport and recombination effects in nanocrystalline materials, since it can consider both energetic and configuration disorder.

Large polarons

Large-polaron (coherent) transport can, to some extent, be likened to that of free carries with two important differences: large polarons have a large effective mass and a generally bigger thermal momentum¹⁷⁶; they move slowly and are only weakly scattered by phonons. The study of large polaron mobility and the calculation of materials specific transport properties are typically conducted following the Boltzmann equation^{180,181} or the Feynman, Hellwarth, Iddings, and Platzman (FHIP) approach^{104,106,182}.

In a recent article, Frost has instructively summarized the most widely used formulas to compute large polaron mobilities and developed a versatile computer code for the variational solution of the Feynman polaron model at finite temperatures.¹⁰⁶

The originally-proposed, low-T approximation for the FHIP mobility μ_{FHIP} is given by (in S.I.):

$$\mu_{FHIP} = \left(\frac{w}{v}\right)^3 \frac{3e}{4m} \frac{\exp(\beta')}{\Omega \alpha \beta'} \exp\left(\frac{v^2 - w^2}{w^2 v}\right) \quad (12)$$

where w and v are Feynman variational parameters m represents the band effective mass, Ω is the phonon frequency, α the coupling constant and $\beta' = \hbar\Omega/k_B T$.

A first attempt to extend the validity of this formula at higher T was introduced by Kandoff, who derived a similar equation using the Boltzmann formalism extended to all coupling strengths α within the relaxation-time approximation¹⁸⁰, showing the intrinsic compatibility of the Feynman and Boltzmann language. This approach has been recently used in conjunction with kinetic Monte Carlo simulations to estimate the mobility in lead-halide perovskites⁷².

A more recent improvement has been proposed by Hellwarth *et al.*¹⁰⁴, who extended the FHIP formalism beyond the low-T

limit and derived the following expression

$$\mu_H = \left(\frac{w}{v}\right)^3 \frac{3e}{m} \frac{\sqrt{\pi} \sinh(\beta'/2)}{\Omega \alpha \beta'^{\frac{5}{2}}} K^{-1} \quad (13)$$

where K is an integral providing the polaron response to a first order change in the driving force. The first complete numerical evaluation of this integral was recently achieved in Ref. 106 for the calculation of the large polaron mobility in Methylammonium lead iodide perovskite (MAPI) using a first principles extension of the Feynmann variational expression within the Ōsaka's finite-temperature variational solution¹³. A representative result of this study is displayed in Fig. 2(e), which shows a comparison between the calculated μ_H and single crystal terahertz conductivity measurements. A good quantitative agreement is obtained at room-temperature. We will briefly discuss the polaron properties in halide perovskites in a dedicated section.

Finally, we would like to spend a few words on charge transport beyond the quasi-particle scattering regime, where the inelastic scattering rate exceeds the thermal energy of quasiparticles (QP) and the kinetic equation (suitable for the coherent regime) cannot be applied anymore⁸³. Also in this case DiagMC appears to be a superior method, capable to reveal the main beyond-QP features and to provide the fundamental basis for the interpretation of mobility data in materials with strong electron-phonon coupling⁸³. From a first principles perspective, Zhou and Bernardi⁸² have proposed a finite-temperature retarded cumulant diagram-resummation technique (including higher-order electron-phonon interactions) which delivers an overall good picture of beyond-QP mobility in SrTiO₃ in the range 150-300 K.

Types of polarons

The previous sections have introduced general types of polarons: small and large (see Box 1), hole and electron polarons [see Fig. 1(b)] and single- or bi-polaron (see Fig. 3). This section extends the classification of polarons by discussing the most notable types that can form in materials, their origin and role, and provides selected examples of their manifestations

List of polarons		
Polaron	Signification	Reference
Electron or hole polaron	Self-trapped electron or hole coupled with phonons	Reviews ^{1, 168, 176, 179, 183, 184}
Large Fröhlich polaron	Long-range el-ph interaction, spatially extended (see Box1)	Theory ^{7-9, 102, 103} , Expt. (<i>n</i> -doped a-TiO ₂) ⁵¹
Small Holstein polaron	Short-range el-ph interaction, spatially confined (see Box1)	Theory ^{10, 11, 110, 111} , Expt (UO _{2+x}) ¹⁶
Bipolaron	Bound pair of two polarons (Holstein or Fröhlich) similar to superconducting Cooper-pair ¹⁸⁸	Theory ^{29, 185-187} (manganites, cuprates) Expt. & DFT (BaK _x Bi _{1-x} O ₃) ^{132, 189, 190}
Magnetic (spin) polaron	Small polaron coupled with localized spins	Theory ^{191, 192} , Expt. & DFT (EuO ^{193, 194} Fe ₃ O ₄ ⁸¹ , (La _{1-x} A _x) _{2/3} Ca _{1/3} MnO ₃) ^{25, 195}
Jahn-Teller polaron	Polarons stabilised by Jahn-Teller effects	Expt. (La _{1-x} Sr _x MnO ₃) ²⁸ , cuprates ²⁹ Expt. & DFT (ABO ₃) ^{196, 197} , Theory ^{198, 199}
Ferroelectric polaron	Polarons stabilised by ferroelectric distortions	Expt. & DFT (Halide perovskites) ^{31, 48} DFT (SrTiO ₃) ^{200, 201} , strained BaTiO ₃) ²⁰²
Zener polaron	Two spin polarons coupled by double exchange (FM polaron dimer)	Theory ²⁶ , doped manganites (Expt. ^{26, 27} HF ²⁰³ , DFT ^{204, 205})
2D polaron	polaronic self-trapping confined in 2D	Theory ^{183, 206} , Expt. (MoS ₂) ³³ DFT (Hf/ZrO ₂) ³⁴
Polaron exciton (self-trapped exciton ²¹¹)	Bound pair consisting of an <i>e</i> -polaron and <i>h</i> -polaron	Theory ²⁰⁷⁻²⁰⁹ , Expt. (ZnO ²¹⁰ , C60 ⁵⁷), Review (conjugated polymers ²¹²)
Dopant/defect polarons	(small) polarons bound to dopants and defects	Expt & Theory (TiO ₂) ⁴⁹ , Book ¹⁷⁶
Molecular polaron	Self-trapping caused by short-range chemical bond formation	Theory ²¹³ , Expt (DEH molecule) ²¹⁴ Review (conducting polymers) ²

Table 2. List of different types of polarons in materials.

The focus is on *dielectric* polarons, namely self-trapping of an excess charge arising from the electron/hole coupled with the (self-induced) polarization field developed in a polarizable medium. For the sake of completeness we mention that, in the context of molecular solids, biological materials and polymers, the commonly used jargon is *molecular* polarons, to designate polaron whose self-trapped electronic charge carrier is primarily confined within a single molecule¹⁷⁶. The embedding medium

can contain displaceable ions and polar molecules causing a strong interaction between the excess charge carrier with molecular vibrations (which makes the formal difference between dielectric and molecular forms disputable). A relevant manifestation in this context is the so called charge carrier solvation in which the polaron formed in a semiconducting unit immersed in a polar solvent interacts with the solvent and modifies its polarization, leading to a modification of the optical absorption spectra and carrier mobility.^{215,216}

The most evident polaron forms reported in literature are listed in Tab. 2, which also includes a basic definition of the distinct signification. In addition to differences arising from the size (small and large) or the charge (positive or negative), the main characteristic distinction among the various polaron entities originates from the characteristic coupling with the surrounding environment, alternative to the standard short- or long- range electron-phonon (el-ph) coupling:

- Specific types of structural/electronic distortions, e.g. static and dynamic Jahn-Teller (JT) effect, or ferroelectric instabilities. For instance the lattice polarization around a JT center is enhanced by the spontaneous breaking of the local point symmetry caused by the lifting of a carrier's orbital degeneracy.
- Entanglement with a cloud of magnetic (or antiferromagnetic) excitations, namely the intrinsic spin of the extra electron or hole can couple with the surrounding spin-lattice and can induce a magnetic polarization through a variety of spin-spin interactions (a peculiar type of magnetic polaron is the coupling between two spin-polarons by double exchange, known as Zener polaron).
- Dimensionality. The strength and intensity of the el-ph coupling can be confined in two dimensions giving rise to two-dimensional (2D), surface, or interface polarons.
- Interaction with defects or dopants. In this case polaron formation is driven (or enhanced) through the interaction with chemical defects (a common case are oxygen vacancies⁴⁹), dopants (for example Li and H¹⁷), structural defects (steps or domains⁹⁴) or with muons⁵⁰. The interaction of polarons with water can also be grouped in this category^{86,128,217}.
- Polaron-polaron bound states. The most notable examples are bipolarons and polaron excitons (schematically introduced in Fig. 3). Bipolarons are similar to Cooper-pairs in the Bardeen-Cooper-Schrieffer (BCS) theory of superconductivity, but the two electrons (or holes) are bound by the exchange of virtual phonon in real space (and not in \mathbf{k} -space as in BCS)^{1,188,218}. A polaron exciton is instead a bound state formed by the combination of an electron and hole polaron. In this case the properties of the excitonic bound pair is affected by the lattice deformations accompanying the (re)combination process. Self-trapped excitons (STE)²¹¹ are attracting a great deal of attention in particular for their relevance in light-electric interconversion and photoluminescence. Ubiquitous in organic molecular crystals, STE have been recently observed and characterized in halide perovskites^{219,220} and van der Waals interfaces formed by transition-metal dichalcogenides²²¹. The theoretical account of excitonic properties requires further extensions of the polaron theories reviewed above. In the context of *ab initio* methods one of the most accurate scheme is non-equilibrium many-body perturbation theory, which can describes processes activated by ultra-short laser pulses including coherent and non coherent dynamics of excitons.²²²

The nomenclature proposed here is a general classification guided by the observations and idioms reported in literature, but should not be taken too rigidly. Other mixed-states composed by different types of polaron can form and are encountered in materials. For instance JT effects in a magnetically active background give rise to JT-magnetic polarons as recently observed in magnetite⁸¹. Similarly, it is natural to extend the concept of ferroelectric polarons to multiferroics^{202,205}. Also, any of the polaron types listed in Tab. 2 can be related to a defect or can be confined in 2D²²³. An illustration of selected examples are collected in Fig. 4.

Many materials (in particular transition metal oxides) exhibit polaron formation and their properties are affected by the formation and mobility of polarons: manganites, cuprates, titanates, bismutates, iron oxides etc. (see Tab. 2). The number of articles dealing with polarons in materials continues to grow. Before moving on to the specific cases of TiO₂ and halide perovskites, and for the sake of completeness, additional recent advances should be mentioned: Metal peroxides⁷⁷, BiVO₄^{224,225}, WO₃⁷⁸, CeO₂^{75,97,226}, BaCeO₃²²⁷, GdTio₃²²⁸, SrTiO₃^{229,230}, YTiO₃²³¹, KTaO₃²³², BaSnO₃²³³, BiFeO₃²³⁴, Iron oxides^{85,235,236}, ZnO⁸⁰, Co₃O₄²³⁷, BiVO₄²³⁸, Ga₂O₃²³⁹, and layered compounds²⁴⁰.

Experimental detection and characterization of polarons

Polarons manifest themselves in many different ways and can be probed with a large array of experimental techniques; a partial overview is given in Tab. 3. This section briefly discusses the most common methods as well as emerging techniques, using examples of prototypical polaronic systems, and illustrate the impact of polarons on specific materials properties. Each method has its own strengths, yet obtaining a complete picture of polaron behavior in a specific material typically requires a combination of complementary techniques and, when possible, a direct comparison with theoretical simulations.

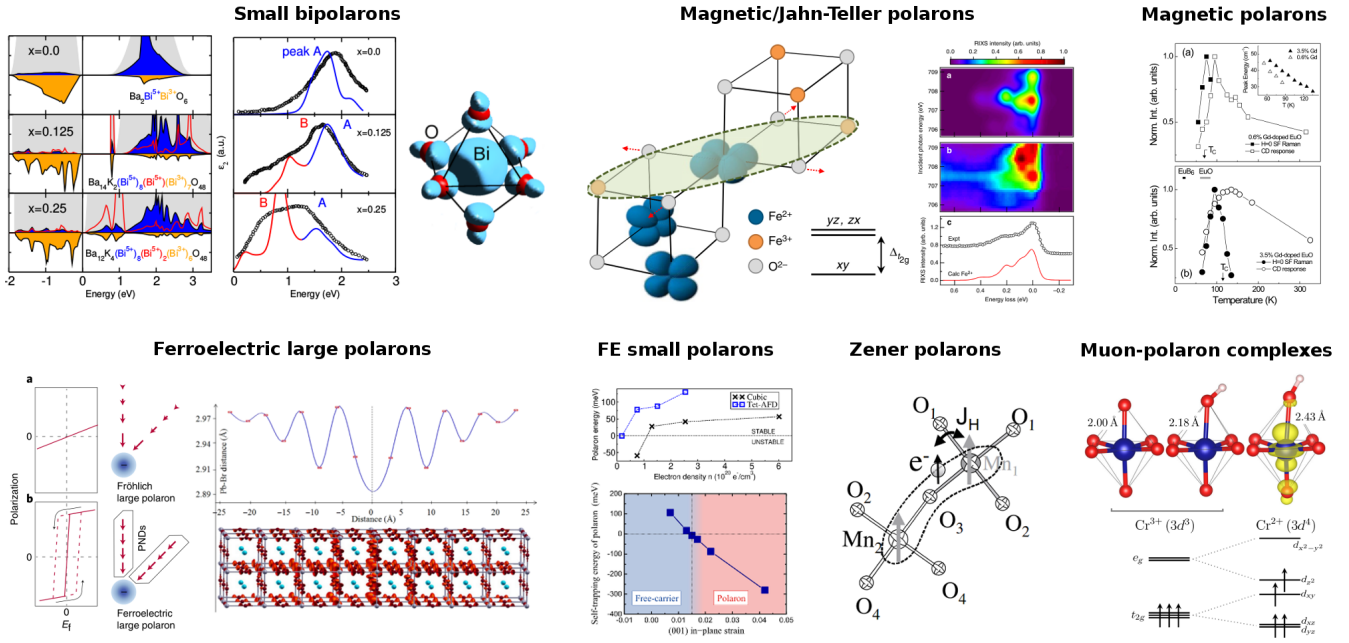


Figure 4. Collection of theoretical and experimental visualizations of different types of polarons. Insulator-to-metal (IMT) transition mediated by small bipolarons in $\text{BaBi}_{1-x}\text{K}_x\text{O}_3$ ¹³²; Jahn-Teller distortions coupled with magnetic polarons in magnetite⁸¹; temperature evolution of magnetic polarons through the IMT in $\text{Eu}_{1-x}\text{Gd}_x\text{O}$ ⁵⁵; ferroelectric large polaron in halides perovskites^{31,48}; dependence of the (small) polaron binding energy on ferroelectric instabilities and strain in SrTiO_3 ²⁰⁰ and BaTiO_3 ²⁰²; Zener polaron in half-doped manganites²⁷; octahedrally coordinated Cr atom in antiferromagnetic Cr_2O_3 (left) without the muon, (middle) with the positive muon, and (right) a neutral-charge muon-polaron complex⁵⁰.

Transport Measurements

Polarons dictate the transport properties of materials, and, historically, **electrical resistivity measurements** gave the first direct proof for polaron formation¹⁶. Figure 5a illustrates the typical characteristics of small and large polarons in the two TiO_2 polymorphs rutile and anatase, respectively⁴⁹. The dopant, Nb^{5+} , replaces a Ti^{4+} ion and donates a single electron. It causes negligible lattice distortions that would otherwise lead to additional electron trapping. The resistivity of TiO_2 anatase (Fig. 5a) decreases at low temperatures, and the material remains conducting; large polarons are predominant⁴⁹ and coherently propagate through the lattice⁵¹. In contrast, the resistivity of TiO_2 rutile (Fig. 5a) increases with cooling, as self-trapped electrons require an activation energy for hopping.

Hall measurements provide the necessary complementary information about mobility and carrier concentration, n , see Figure 5. In anatase, n is temperature-independent; all dopants are ionized and the electrons contribute to electrical conduction. The electron mobility shows a metal-like behavior, increasing at low temperature when scattering at phonons is suppressed. In rutile, n shows Arrhenius behaviour and the activation energy can be estimated (here 75 and 88 meV for two different samples). This activation energy is not related to donor ionization, but to polaron hopping to neighboring sites. Other techniques (such as XPS, STM, or DFT) can prove that the electron polarons leave the dopant^{49,243}, reside on lattice Ti sites (creating the characteristic Ti^{3+} state), and the attractive coupling to the original donor is small^{95,244}.

The different behaviors of rutile and anatase affect applications. For example, n -doped anatase is a transparent conductive oxide²⁴⁵ while rutile becomes opaque upon doping, and anatase is the preferred electrode in dye-sensitized solar cells²⁴⁶ because of its favorable transport behavior. A general consensus on the polaron behaviour in anatase and rutile has only been achieved during the past decade, using a combination of transport measurements,²⁴¹ ARPES results⁵¹ and DFT calculations⁴⁹. Previous literature mostly assumed that the anatase polymorph had higher polaron formation energies, which was a misinterpretation of the strong coupling between large polarons and optical phonons visible in optical spectroscopies.

A more complex polaronic behavior is shown in Figure 5b on the example of perovskite-based manganites, materials known for the colossal magnetoresistance effect (CMR). Here Sr is used as a p -dopant, introducing hole polarons into the material and inducing mixed $\text{Mn}^{4+}/\text{Mn}^{3+}$ valence. The high magnetic moment of Mn and its interaction with the lattice result in a rich variety of competing ground states. For instance, for a Sr doping level of 15% the material undergoes a successive transition from polaron liquid (insulator) \rightarrow Fermi liquid ("metal") \rightarrow polaron lattice.^{28,242} Pressure-dependent transport and

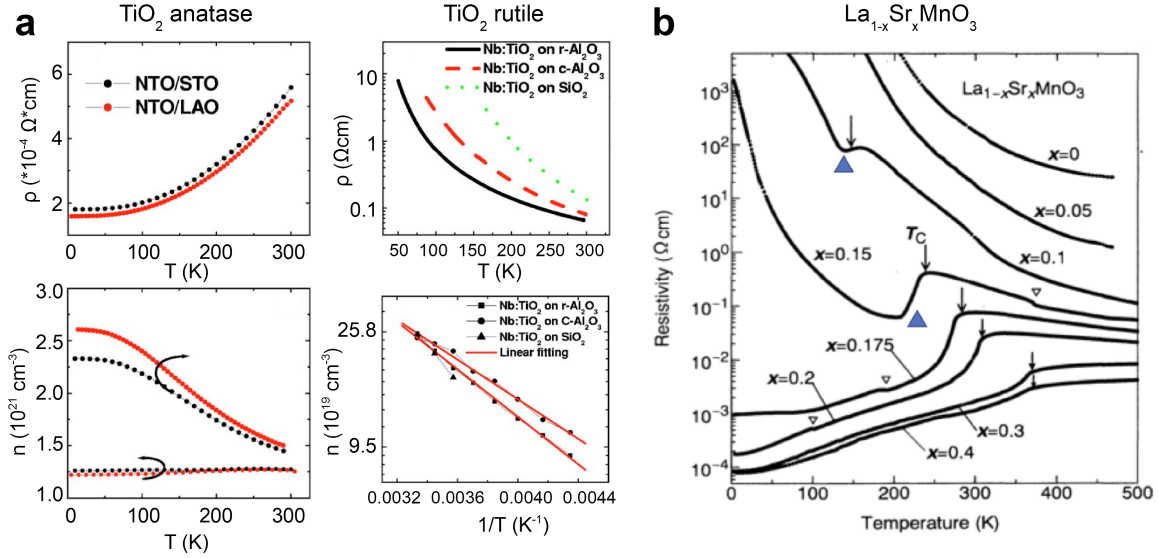


Figure 5. Transport measurements. a | Anatase and rutile TiO₂ thin films doped by 5% Nb. The resistivities of the two polymorphs show opposite behaviour with temperature. Hall measurements show that the carrier concentration is constant in anatase, while it appears activated in rutile. This behavior is typical for large and small polarons, respectively. Adapted from Ref. 241. b | Hole polarons, introduced by doping Sr into the perovskite manganite LaMnO₃, have a dramatic effect on resistivity. The arrows indicate the Curie temperature, open and filled triangles indicate structural phase transitions and polaron ordering, respectively. Adapted from Refs. 242, 28

magnetization experiments²⁶ were instrumental in mapping out the role of orbital ordering and Zener polarons (see Figure 4).

In addition to electronic transport, **thermal transport** is equally affected by polaronic behaviour. The relation between the **Seebeck coefficient** and electrical conductivity can distinguish band-like conduction from small polaron hopping,²⁴⁷ and identify the major scattering mechanisms of charge carriers²⁴⁸. Seebeck measurements are especially useful in materials with low conductivity, where Hall measurements are not possible.

Optical Spectroscopies

Optical reflectivity and photoconductivity. Optical measurements are well suited to explore the role of electron-phonon coupling. Such measurements are best performed over a wide span of photon energies, ranging from the THz regime to the visible. An instructive example is given in Fig. 6a, where the reflectivity and transmission was measured on SrTiO₃ single crystals doped with different levels of Nb²⁴⁹. The conductivity, derived from the inversion of the Fresnel equation and Kramers-Kronig analysis, shows several features: When going from high to low photon energies, one observes absorption across the optical band gap, sub-band gap excitation at 2.4 eV from dopant electrons occupying the t_{2g} states, and optically active phonons; the softest phonon experiences a significant hardening with doping. The narrow Drude peak (dots in Fig. 6) is due to the coherent part of the polaronic conduction, and the mid-infrared band spreading from 0.1 to 1 eV is due to a multi-phonon side band of the Drude response, here assigned to the 'incoherent' contribution²⁴⁹. A detailed analysis of these spectra, based on Fröhlich many-body large polaron theory was given in Ref. 59.

Raman spectroscopy. Inelastic or Raman scattering is an ideal complement to such photoconductivity measurements, and examples are shown in Fig. 6. The Raman spectra in Fig. 6b were taken on a doped manganite sample that experiences a phase transition from a high-temperature, semiconducting paramagnetic to a ferromagnetic metallic state at 145 K²⁵⁰. Above the transition temperature the spectrum shows three phonon bands on a low-frequency background (dashed line), which disappears below T_C . It is attributed to collision-dominated scattering from incoherent hopping of carriers, *i.e.*, to small-polarons. More detailed analysis indicated a co-existence of large and small polarons in the low-temperature metallic state²⁵⁰. In semiconductors, the Raman scattering cross section is dramatically enhanced when the exciting wavelength is in resonance with the band gap. In pioneering work, Scott et al.²⁵¹ reported an empirical relationship between the number of excited, optical phonons and the coupling constant α under such conditions. (This is clearly seen in Fig. 6c, where the 5th longitudinal optical phonon mode is observed for ZnS at resonant conditions.) This relationship can be used to, *e.g.*, evaluate the anisotropy of α in solids²⁵².

In recent years, advancements in synchrotron-based measurements (high brilliance of sources and detector resolution) have lead to a analogous experiments being possible with x-rays as the excitation source. The so-called **resonant inelastic**

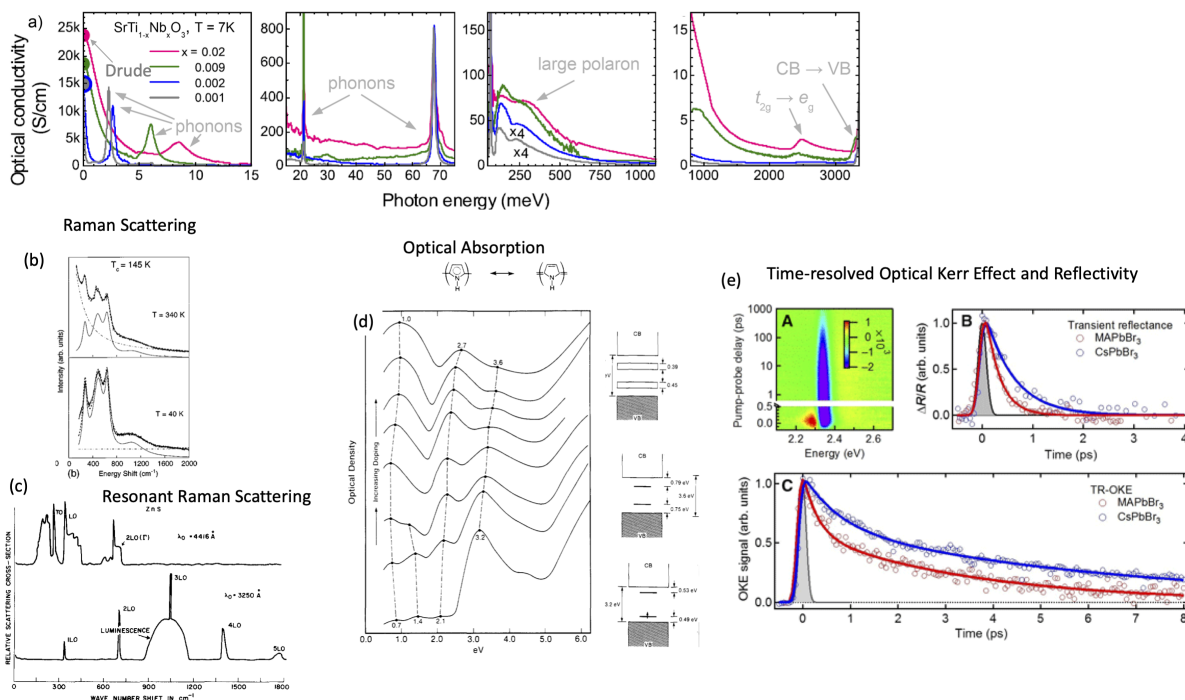


Figure 6. Optical Spectroscopies a | Photoconductivity measurements on SrTiO₃ with various Nb doping levels. Arrows indicated features due to various excitations. Adapted from Ref. 249. b | Raman scattering of a Pr_{0.7}Pb_{0.21}Ca_{0.09}MnO₃ single crystal. The diffusive electronic response (dashed curve) in the high-temperature paramagnetic phase disappears below the transition temperature to the metallic, ferromagnetic phase. Adapted from Ref. 250. c | Raman spectra from ZnS taken with optical radiation tuned to energies on (bottom) and off (top) resonance, adapted from Ref. 251. d | Optical absorption from the conducting polymer polypyrrole that forms bands of bipolarons with increased doping. Adapted from Ref. 2 e | Time-resolved optical spectroscopy measurements on two lead halide perovskites. The fast decay time of the transient absorption (upper right), reflectivity (upper left), and transient optical Kerr effect (OKE) signal (lower panel) is interpreted as the formation time for large polarons. Adapted from Ref. 31.

X-ray scattering (RIXS)²⁵³ is a powerful emerging technique. Here the x-rays are tuned to resonantly excite an electron from a specific core level to an unoccupied state, as this state decays it emits x-rays that are measured. During the lifetime of the intermediate state, the lattice responds to the additional electron with itinerant distortions. The impressive energy resolution achievable with modern spectrometers allows an analysis of the resulting phonon contribution, and evaluation of the electron-phonon coupling in an element- and momentum-resolved fashion.²⁵⁴

The presence of polaron-induced gap states is reflected in **photoabsorption**. The example in Fig. 6d is drawn from the instructive paper by Bredas², which lays out the comparison between the radical states in ionized polymers (which are distorted as compared to a neutral molecule) and polaron physics. The polymer polypyrrole, examined in Fig. 6d becomes conducting upon doping (or, in chemical language, oxidation) with ClO₄. For low doping levels, polaronic states form at the band edges (see sketch in Fig. 6d). These give rise to the three absorption peaks in the lowest trace in Fig. 6d, with excitation from the VB to the lower and upper polaronic levels, and transitions in between these states. As the doping level is increased, bipolarons (see sketch in Fig. 3) become energetically favorable and eventually form bands. These bipolaron bands dominate the transport behavior in the conducting polymer, an assignment strengthened by EPR²⁵⁵ (see below), where the signal of the unpaired spin in the polaronic state disappeared when bipolarons with paired spins were formed.

Photoluminescence is widely applied to powder materials synthesized for photocatalysis²⁵⁶ and organic molecules and polymers with applications in optoelectronics^{2,257}. Full interpretation of photoluminescence data is often difficult: Both electrons and holes can form a polaron, providing photoluminescence signals at longer wavelength than the excitation photons. The many configurations include polarons, bipolarons, solitons (in organic terminology radical ions, divalent ions, and ions, respectively²⁵⁸), additionally charges may trap at defects. On single crystals at low temperatures the hyperfine structure can be resolved and the type of polarons²⁵⁹ can be identified, but often photoluminescence is used for a quick comparison of samples that have been prepared or treated in different ways.

Performing optical measurements in a **time-resolved** manner provides information about polaron dynamics and the polaron

formation time. In **transient absorption spectroscopy** the system is pumped with a femtosecond pulse, and the optical absorbance in the UV-VIS region is monitored as a function of time delay. The difference spectra (see also Fig. 7) reflect the time evolution of different ground and final states after photoexcitation. Figure 6e shows a recent example from lead halide perovskites (MAPbBr₃ and CsPbBr₃).³¹ Here electrons, pumped from the valence band to the conduction band, form large polarons. The lower panel shows the **transient optical Kerr effect (TR-OKE)** signals as a function of time delay from the probe pulse. (The OKE signal is due to the rotation of the polarization of the IR probe pulse, caused by the transient non-linearity introduced by the pump pulse.) From an FFT of such transients, the phonons involved in lattice distortions become apparent, e.g., for sub-band gap excitation the Raman active modes are clearly visible. The upper two panels in Fig. 6e show the transient absorption/reflectivity of a white probe pulse, again as a function of time delay to the same pump pulse. All types of signals show an initial decay with similar time constants, 0.3 and 0.7 ps for MAPbBr₃ and CsPbBr₃, respectively, which is interpreted as the polaron formation time, in agreement with the DFT analysis of the displacement frequencies (although a correct localization of large polarons in these materials is technically hard to achieve). For the TR-OKE, the fast initial decay is followed by a longer-lived anisotropy, attributed to polaron motion³¹.

Valence Band Photoemission

Photoelectron spectroscopy (PES) of the valence band is a well-established technique for analysis of electronic structure of materials in general, and for polaronic effects in particular²⁶⁰. The emission of photoelectrons is fast compared to the motion of atoms, *i.e.*, the lattice does not relax while the electron is removed. Thus the apparent binding energy E_{EL} measured by photoemission corresponds to the sum of the polaronic energy E_{POL} and the lattice strain E_{ST}

$$E_{EL} = E_{POL} + E_{ST} = h\nu - E_K - \Phi, \quad (14)$$

where $h\nu$ is the incident photon energy, E_K is the kinetic energy of the emitted electron and Φ is the work function of the spectrometer.

Representative spectra are already shown in Box 1 for the prototypical examples of rutile and anatase TiO₂. Small polarons (rutile) manifest themselves as deep states (with an $E_{EL} \approx 1$ eV below E_F) reflecting the larger energy stored in lattice distortions. Large polarons (anatase) typically appear as a shallow sharp peak, in order of tens of meV below the Fermi level, with tail in a characteristic peak-dip-hump structure²⁶⁰.

It is instructive to consider angle-resolved photoemission measurements for these two cases, see Fig. 7. Note that the two experiments were conducted with different photon energies $h\nu$. Figure 7a shows **angle-resolved photoemission spectroscopy (ARPES)** results on the large-polaron material anatase⁵¹. As the parallel component of the emitted photoelectron is preserved, the k -dispersion is directly measured. The polaronic band is located 40 meV below the Fermi level and has multiple images at higher binding energies, see also Box 1. These image bands originate from the strong coupling to longitudinal optical (LO) phonons, *i.e.*, the electron is emitted and one or multiple LO phonons are excited during the photoemission process. Strong coupling with LO phonons is typical for large polarons and is often used to identify the presence of polaronic effects²⁶⁰ in shallow bands and distinguish polarons from other phenomena (this behaviour was confirmed by DFT for anatase TiO₂⁴⁷).

Small polarons are localized at a single lattice site. The momentum k is not a good quantum number, and small-polaron features appear flat in k -space in ARPES. Nevertheless, angle-resolved photoemission can provide information about the preferential location of such small polarons. When photoelectrons have several hundred eV, interference effects lead to 'forward focusing' and an enhanced intensity behind a scatterer. In **x-ray photoelectron diffraction (XPD)** the intensity is strongly increased along the direction from the emitter to its nearest neighbor. If the emitter is at the top surface, then the intensity is uniform in space. If the emitter sits in sub-surface layers, its position can be triangulated from the maxima in polar plots.

Figure 7b shows such the results for such an XPD measurement²⁴³ on rutile TiO₂(110); plotted is the the intensity of the gap state at 1 eV (see Box 1). To increase the cross section for this state, resonance effects were exploited; the photoemission data were taken with a photon energy of 462 eV, *i.e.*, at the Ti2*p* – 3*d* transition. Bright spots in the polar plot in Fig. 7b correspond to directions between different atom pairs, the atom labeling is explained in the structural model in Fig. 7c. The work in Ref. 243 brought the first direct experimental evidence that polarons on rutile (110) are preferentially located at subsurface sites, and even provided a quantitative estimate for the occupancy of the different Ti atoms.

Core Level Spectroscopies

Core level spectroscopies probe the electronic structure in an element-specific way. Various combinations of incoming and outgoing radiation are possible, leading to an array of techniques that can be used to characterize polarons; for a review the reader is referred to Ref. 52.

X-ray photoemission spectroscopy (XPS) is a well-established method to determine the oxidation state (or valence) of atoms. In a highly simplified, initial-state picture the binding energy of a core level electron shifts to smaller values when the

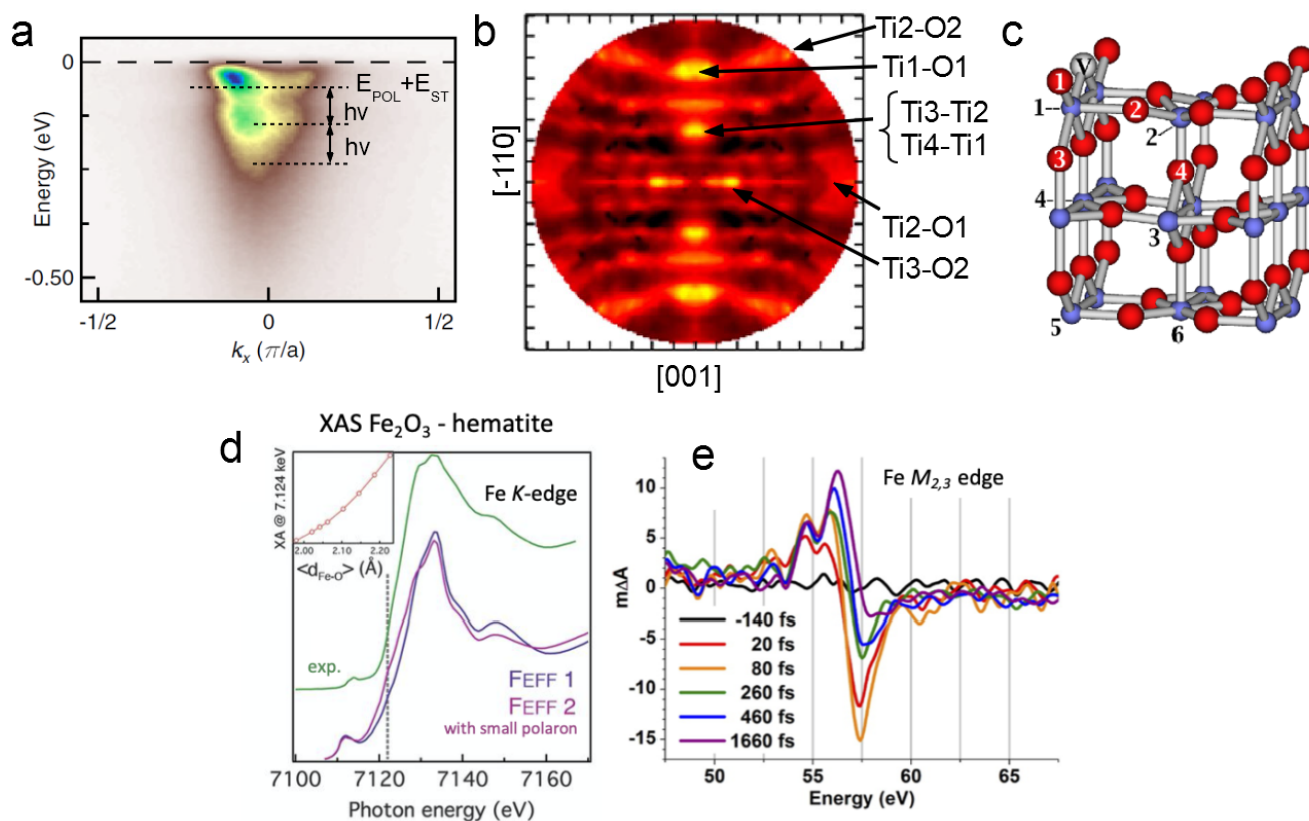


Figure 7. ARPES, XPD and XAS measurements of large and small polarons. a | k -dispersion of large polarons measured on the anatase TiO_2 (101) surface by angle-resolved photoemission ($h\nu=84$ eV). Adapted from Ref. 51. b | X-ray photoelectron diffraction data of the small-polaron state on the rutile TiO_2 (110) surface ($h\nu=462$ eV). The plot shows the intensity of the gap state with a binding energy of 1 eV (see box), taken along different crystallographic directions. Interference leads to 'forward focusing' and the spots marked in the plot correspond to directions along pairs of atoms, as labelled in the cluster shown in c. Adapted from Ref. 243. d | X-ray adsorption (XAS) measurements of hematite Fe_2O_3 , Fe K -edge. The purple spectra were calculated with a full multiple scattering code, the intensity at the onset is sensitive to the average Fe-O bond length (inset), which is elongated by the presence of small electron polarons. e | Transient $M_{2,3}$ XAS after e-h pair excitation across the band gap, a polaron formation time of 240 fs was extracted. Adapted from Ref. 261.

Coulomb attraction of the positive nucleus is screened by adding valence electrons. Since small electron/hole polarons are essentially local centers with increased/reduced valence, their presence causes a down/upshift in the XPS binding energies. Electron-phonon interactions lead only to a broadening of XPS peaks²⁶², however.

X-ray absorption spectroscopy (XAS), where a core electron is promoted to an excited state in the conduction band, gives more information about polaronic states and, increasingly, also the polaron dynamics using ultrafast pump-probe setups. The position of an absorption edge shifts with the oxidation state of an atom, and the fine structure reflects the signatures of its environment, *e.g.*, the crystal field splitting caused by the surrounding ligands in ionic compounds⁵². The shape of the XAS peak is thus sensitive to local distortion. Fig. 7d shows the Fe K -edge of Fe_2O_3 hematite²⁶³. The purple spectra were calculated considering increased Fe-O bond lengths induced by a small electron polaron (see inset). Fe_2O_3 would be a promising material for photoelectrochemical water splitting, but the sluggish charge transport and trap states induced by polaronic effects are a severe limitation. The formation of the polarons introduced by direct photoexcitation across the Fe_2O_3 band gap is followed in Fig. 7e. In this case the Fe $M_{2,3}$ edge was probed in such **XAS transients**²⁶¹. The initial excitation involves charge transfer from the O ligand to the Fe $3d$ states, and the excited Fe^{2+} state decays to a long-lived trap state in 240 fs. In addition to monitoring absorption, one can analyze the x-rays emitted when the core hole is filled (in **x-ray emission spectroscopy, XES**) or the energy loss (**Resonant inelastic x-ray scattering, RIXS**) in the scattered x-ray beam in the normal state and after charge injection^{52,84}.

X-ray free electron lasers (XFEL) bring a much higher brilliance, shorter time signature, as well as spatial and temporal coherence to such experiments; as more facilities come online, they promise a bright future for characterizing polarons in

novel ways. One pertinent example is the **time-resolved XAS** experiment on TiO₂ anatase described in Ref. 264, conducted with an XFEL. Here the time signature of the photo-excited electron polaron could be followed; it would be very exciting to see similar insights for the hole polaron as well. An important feature is the high coherence of these sources, e.g., in **X-ray photon correlation spectroscopy (XPCS)**²⁶⁵, the evolution of consecutive speckle patterns is measured and allows following the dynamics of a disordered system as a function of wave vector transfer, q , and time. Together with **diffuse x-ray scattering**, this should allow mapping out and visualizing the ultrafast dynamical processes that lead to polaron formation.

Spin Resonance Techniques

Electron Paramagnetic Resonance (EPR) detects unpaired spins (more specifically, their resonance when excited by microwave radiation while tuning an external magnetic field) and through their g tensor the coupling with their environment (these quantities can be obtained by computer simulations, providing useful insights to interpret EPR signals²⁶⁶). Since the EPR signal intensity is a direct measure of the number of unpaired spins it was useful in confirming the bipolarons in conducting polymers (see also Fig. 6d); the continuous wave EPR signal did not scale with dopant density²⁵⁵. Another example are defects in ionic solids that disturb the charge balance and result in localized charges or 'trap states'. A prominent example is BaTiO₃, where impurities that introduce paramagnetic centers were extensively characterized by EPR²⁶⁷. Spurious Na⁺ replacing lattice Ba²⁺ results in a polaronic hole on the neighboring lattice O²⁻ ion. The natural isotope ²³Na has a nuclear moment $I = 3/2$, and the hyperfine interaction of the spin on the resulting O⁻ ion allows its identification; conversely a Nb⁵⁺ donor atom in the lattice results in an additional spin at a Ti³⁺ site. EPR measurements can be easily combined with other types of radiation. Once these EPR signatures were established for BaTiO₃, the electrons and holes that are induced by photoexcitation could be studied, and their trap sites and temporal behaviour was followed²⁶⁷. This approach is particularly interesting for photocatalytic materials. For TiO₂, Chiesa et al.²⁶⁸ reviewed how EPR can be used to determine the degree of wave function localization, taking advantage of pulsed techniques and of enriching the material with ¹⁷O (which has nuclear spin, other than the naturally much more abundant ¹⁶O). This results in a rich lineshape due to the resulting hyperfine coupling.

A different type of isotope effect was used in establishing Jahn-Teller polarons in the CMR material La_{1-x}Ca_xMnO_{1+y}²⁶⁹ (see Tab. 2). Here comparative EPR measurements were conducted after replacement of ¹⁶O with ¹⁸O, both with a nuclear spin $I = 0$, but the latter with an increased mass. Doped manganites have mixed valency, Mn³⁺ and Mn⁴⁺, and the electron couples via the O between two neighboring Mn, so the mass of the O matters for the charge transport. From the temperature dependence of the line width of the EPR signal, the exchange integral J could be determined quantitatively; the measurements supported the Jahn-Teller polaron model.

Nuclear magnetic resonance (NMR) spectroscopy, principally similar to EPR, was particularly useful for mapping out the complex behavior of Jahn-Teller polarons in doped La_{1-x}Ca_xMnO_{1+y} manganites²⁷⁰. The most abundant isotope ¹³⁹La has a nuclear spin of $I = 7/2$ and is thus well suited for NMR studies. In the perovskite structure it couples to the magnetic moments of its eight neighboring Mn ions, and their ferromagnetic alignment leads to a strong shift in the resonance frequency. In addition, the quadrupole moment of the La nucleus interacts with the local electric field gradient due to the surrounding ions, and is thus sensitive to local distortions indicative of polarons. In the ordered paramagnetic phase the resulting field-induced Zeeman splitting leads to an angular-dependent fine structure in single crystals, and to a broad background in polycrystalline samples; the temperature-dependence of this background reflects the transition from the high-temperature paramagnetic to the low-temperature ferromagnetic phase. Fast and inhomogeneous spin relaxations diminish the NMR signal, and with appropriately pulsed fields (*spin echo measurements*), it was established that the wipeout of the NMR signal observed for lightly doped, insulating materials, is due to diffusion of short-range charge excitations coupled to lattice distortions, i.e. polarons²⁷⁰.

A complementary technique for investigating the local magnetic and electronic environment around a nucleus is **muon spin relaxation (μ SR)**. Here a beam of low energy (a few keV) positive muons with 100% spin polarization is directed on a sample. The muons preserve their spin polarization upon implantation into the material, and decay with a mean lifetime of 2 μ s by emitting a positron. During this time the spin interacts with its surroundings, and the angular correlation of the emitted positrons reflects the spin relaxation, similar to the information gained by pulsed NMR. Because μ SR is very sensitive it can be used to detect small magnetic polarons, i.e., a localized electron with its spin ferromagnetically aligned with the localization center (see Tab. 2). In ref. 56 this was shown for Eu-based magnetic semiconductors; a fast relaxation of the muon in the paramagnetic materials was related to the local magnetic field of the magnetic polaron⁵⁶.

Diffraction techniques

As polarons, in particular small polarons, induce sizeable structural distortions in the lattice, they become observable by diffraction with x-rays, electrons, or neutrons. Long-range ordering of polarons results in superstructures, and structural refinements give bond lengths, which reflect charge carrier localizations. **Neutron diffraction**, which is additionally sensitive to magnetic ordering, was instrumental in clarifying the behavior of polarons in the rich phase diagrams of doped manganites,

for example the charge order transition from metallic to insulating $\text{La}_{0.85}\text{Sr}_{0.15}\text{MnO}_3$ (Figure 5b) was attributed to the hole polaron ordering²⁸ based on neutron diffraction data.

As phases often condense into small, twinned domains, the local information afforded by high-resolution *transmission electron microscopy* (TEM) is helpful. As an example²⁷¹ the right panels in Figure 8 show TEM results from $\text{Pr}_{0.5}\text{Ca}_{0.5}\text{MnO}_3$. With *selected area diffraction* the superstructure was resolved, atomically-resolved *Scanning Transmission Electron Microscopy* shows ordering, and column-resolved *energy electron loss spectroscopy* (which yields a similar information to XAS discussed above) all played together to refine the ordering²⁷ of the Zener polarons.²⁶

Scanning Probe Techniques

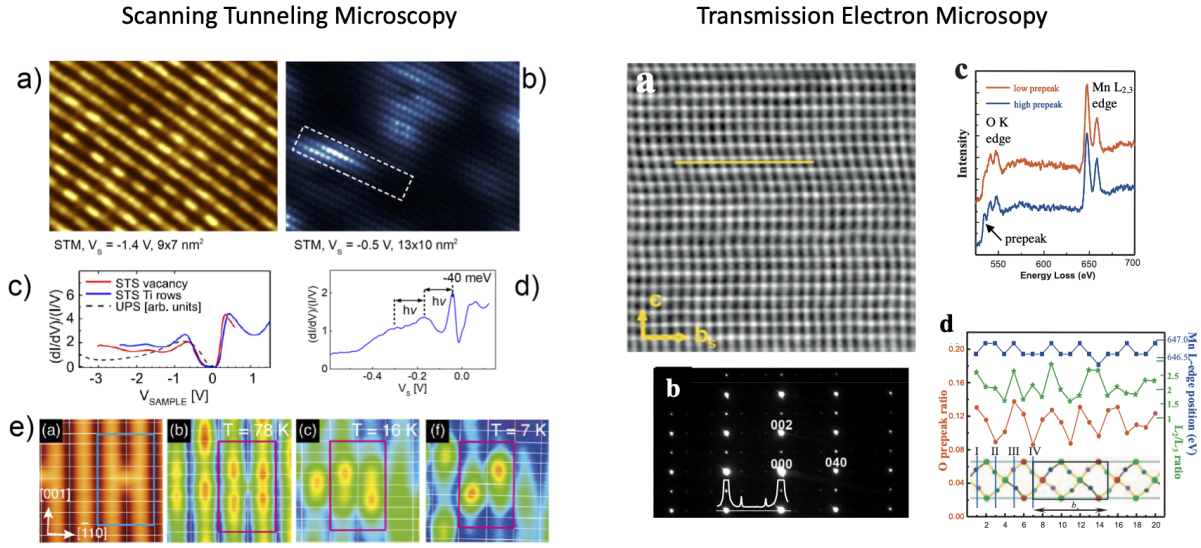


Figure 8. Real space observations of polarons. Left panels: STM and STS of small and large polarons on TiO_2 . a | Filled-states STM images of rutile $\text{TiO}_2(110)$ measured at $T = 78$ K and b | anatase $\text{TiO}_2(101)$ measured at $T = 5$ K, respectively. Adapted from Refs. 42, 49. c | STS spectra on the rutile surface, showing a deep state at ≈ -0.7 V. d | STS spectra measured on the anatase, showing a shallow peak at -40 meV and coupling to LO phonons. e | Series of STM images of a rutile TiO_2 surface taken in the vicinity of a single oxygen vacancy (left image, empty states) and the spatial distribution of polaronic states around the vacancy at 78, 16, and 7 K (filled states images). Adapted from Ref. 244. Right panels: Transmission Electron Microscopy results on $\text{Pr}_{0.5}\text{Ca}_{0.5}\text{MnO}_3$ with ordered Zener polarons. a | Scanning transmission electron microscopy measurements along the [001] direction showing pairing of Mn ions. b | Selected area electron diffraction established the periodicity of the ordered phase c | EELS measurements showing the O K and Mn $L_{2,3}$ edges d | Site-resolved EELS signatures across the yellow line in panel a, showing evidence for polaron ordering as depicted in the sketch. Adapted from Ref. 271.

With *Scanning Tunneling Microscopy* spatially-resolved information can be obtained at the atomic scale. Accessing the polaronic states is technically more challenging than traditional STM imaging of ionic materials. Many of them are n-type doped and STM images are typically acquired in empty states (tunneling into the conduction band), while the states of electron polarons lie below the Fermi level. Filled-state imaging requires lower tunneling currents mainly due to low density of states and the corresponding measurements are often performed in the constant height mode, because the LDOS can be locally too low for maintaining the feedback loop.

The following should be considered when interpreting STM images of polarons: First, the polarons have many equivalent positions in the crystal lattice. Second, the tunneling currents used in STM are typically in order of picoamps, *i.e.*, $\approx 10^7$ electrons per second. STM therefore provides a weighted average of all possible polaronic configurations. This is illustrated in the set of left panels in Fig. 8. Fig. 8a shows a filled-state STM image of a strongly reduced rutile $\text{TiO}_2(110)$ surface²⁴⁴. Rutile forms small polarons, but the density of states appears distributed over all surface Ti_{5c} sites due to the rapid polaron hopping at $T = 78$ K. Spatial confinement of the small polarons can be observed upon cooling to lower temperatures near oxygen vacancies, see Fig. 8e, when the attractive coupling between the polaron and the vacancy becomes comparable to the thermal energy $k_B T$. The characteristic elongated spot observed at low temperature on rutile surfaces can be explained by comparing the experiment with STM images simulated by DFT for polarons localized on sub-surface sites (see also Fig. 9)⁴². At higher temperature, the spatially distributed character of the experimental STM signal can be recovered by averaging simulated images

obtained for different localization sites⁹⁵. The comparison between experiment and theory could be challenging in other cases, where the interaction between sample and tip, typically neglected in DFT calculations, alters the measurement or induces additional polaron hopping^{40,42,244}.

The image in Fig. 8a shows periodic modulations in density of states. This was attributed to a tendency of polarons to arrange in a periodic pattern due to repulsive interactions⁴². Periodic patterns are often observed in systems with charge density waves²⁷², which can be interpreted as ordered arrays of large polarons. STM can also reveal specific places that allow formation of polarons, such as defects²⁷² or step edges⁹⁴.

An example of a large-polaronic system is shown in Fig. 8b. Here the occupied LDOS is enhanced in the vicinity of subsurface defects and the shape and size of these regions match well with the size of large polarons estimated from theory⁴⁹ and photoemission⁵¹. While it took about a decade to find a consensus on interpretation of STM images of small polarons in systems such as rutile TiO₂²⁷³ or CeO₂,²⁷² images of large-polaronic systems are still debated.

For identifying polaronic behavior, *scanning tunneling spectroscopy (STS)*, is an essential complement to imaging. Electron tunneling follows similar rules as photoemission, so peaks in STS spectra typically match photoemission measurements; e.g., compare the PES spectra in Box 1 with the STS spectra on TiO₂ rutile and anatase in Fig. 8c,d.

A rapidly developing Scanning Probe Microscopy technique is *non-contact atomic force microscopy (nc-AFM)*²⁷⁴, especially in combination with the STM function. It allows investigation of highly insulating materials without the requirement for any tunneling current, yet keeps, or even surpasses, the excellent atomic resolution of STM. Combined AFM/STM can separate topographic from electronic structure effects, which is helpful to investigate complex materials²⁷⁵. The excellent force sensitivity allows the detection and manipulation of single electrons²⁷⁶. In principle, nc-AFM should be able to directly address and manipulate single small polarons, although these authors are not aware of published work in this direction. Recent developments offer advanced approaches for investigating electronic states of insulating materials²⁷⁷ and measuring small electric fields with high precision and spatial resolution²⁷⁸. nc-AFM has high potential for addressing many of the open questions behind polarons, and interesting results are likely to evolve in the next years

Experiment				
Year	Material	Source	Exp. technique	Detected polaron
1963 ¹⁶	UO ₂	oxidation	conductivity measurements	small
1964 ²⁷⁹	SrTiO ₃	O vacancies, Nb	conductivity and Seebeck	large
1970 ²⁵¹	ZnS, ZnSe	photoexcitation	Raman spectroscopy	large
1976 ¹⁹³	EuO	O vacancies	optical absorption	small
1977 ²⁴⁷	CeO ₂	O vacancies	conductivity and Seebeck	small
1987 ²⁸⁰	conjugated polymers	photoexcitation	photoluminescence	small
1994 ²⁶⁷	BaTiO ₃	Nb doping	EPR	small
1996 ²⁸	LaMnO ₃	Sr doping	Neutron scattering	small
2001 ²⁷⁰	LaMnO ₃	Ca doping	NMR and muon spin rotation	small
2005 ²⁷²	CeO ₂	O vacancies	STM	small
2007 ²⁷¹	PrMnO ₃	Ca doping	Transmission electron microscopy	small (Zener)
2007 ²⁴¹	a-TiO ₂ and r-TiO ₂	Nb doping	conductivity and optical measurements	large (a), small (r)
2008 ²⁴³	r-TiO ₂	O vacancies	Resonant photoelectron diffraction	small
2010 ⁵⁹	SrTiO ₃	Nb doping	Optical Conductivity	large
2013 ⁵⁴	r-TiO ₂	O vacancies	EPR	small
2013 ⁵¹	a-TiO ₂	O vacancies	ARPES	large
2014 ⁴⁹	r-TiO ₂	O vacancies	STM and STS	small
2015 ⁵⁸	r-TiO ₂	UV/H adatom	infrared spectroscopy	small
2016 ²⁸¹	LiNbO ₃	photoexcited	infrared spectroscopy	small
2017 ³¹	CH ₃ NH ₃ PbBr ₃ and CsPbBr ₃	photoexcited	TR-OKE	large
2017 ²⁶⁴	a-TiO ₂	photoexcited	TR-XAS	large
2020 ⁸⁴	Fe ₂ O ₃	photoexcitation	RIXS	small

Table 3. Overview of experimental works reviewed in the main text. EPR - electron paramagnetic resonance, NMR - nuclear magnetic resonance, STM and STS - scanning tunneling microscopy and spectroscopy, ARPES - angle resolved photoemission spectroscopy, TR-OKE - transient optical Kerr effect, TR-XAS - time-resolved x-ray absorption spectroscopy, RIXS - resonant inelastic X-ray scattering.

Case studies: TiO₂ and Halide Perovskites

This section presents a compact survey of the most important polaron properties of (i) TiO₂, the historically most studied polaron material^{41, 87, 93, 282, 283}, and (ii) halide perovskites, the most rapidly emerging class of materials in the field of photovoltaic technology and optoelectronics^{20, 174, 220}.

Polarons in TiO₂

The two most common polymorphs of TiO₂, rutile and anatase, show a broad range of different polaronic features, which impact their functionalities in electronic transport^{285, 286}, energy conversion²⁸⁷, memristive devices^{244, 288}, or (photo)catalysis^{40, 87, 96, 289–301}. Polarons in TiO₂ samples typically originate from defects and doping, or appear upon irradiation. As a pristine compound TiO₂ is a semiconductor with nominal Ti⁴⁺ and O^{2–} valence states. EPR suggests the presence of additional Ti³⁺ species, due mostly to the presence of naturally-occurring electron donors (interstitial Ti atoms, Ti_{int}, and oxygen vacancies, V_O)^{54, 266, 302}. These additional species reveal electronic charge localization at single atoms, and may correspond to polaron formation, with an important distinction depending on the polymorph (see Figure 9).

Rutile TiO₂ is prone to formation of small electron polarons¹¹⁸. In addition to EPR experiments (see Fig. 9b), pioneering experiments based on optical absorption delivered one of the first strong indications of polaron formation^{303, 304}. The polaron model has been invoked also to explain results obtained by charge transport experiments (see Fig. 5), including the temperature trend of the dielectric function³⁰⁵, the anisotropy of the conductivity³⁰⁶, and the dependence of conductivity on the oxidation state³⁰⁷ and the temperature²⁴¹. Several independent DFT studies have characterized the properties of these small electron polarons in detail^{64, 88, 89, 128, 159, 172, 308, 309}. Together with XPD and STM experiments, they identified sub-surface Ti atoms in the rutile TiO₂(110) lattice as the most favorable trapping sites^{95, 127, 310–312} (see Fig. 7), with the polaronic charge spreading also on neighboring Ti atoms on the surface (see the double spots measured by STM in Fig. 9a)⁴². The in-gap polaronic peak appears typically quite deep and sharp^{313, 314}, although the interactions with defects or other polarons may alter its

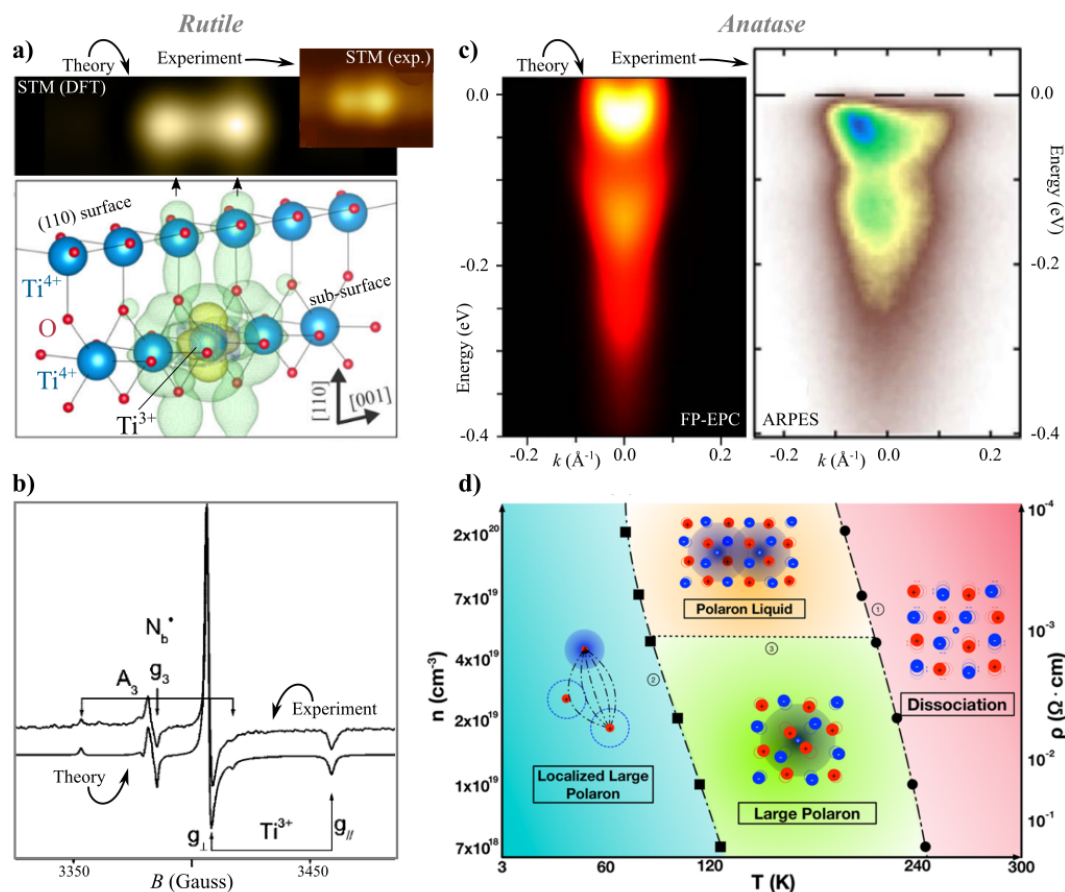


Figure 9. Polarons in rutile and anatase TiO_2 . a | Charge density (bottom) of a small polaron at the rutile $\text{TiO}_2(110)$ surface, and its STM signature (top), obtained from DFT calculations and experiments. b | Theoretical and experimental EPR signal of a Ti^{3+} site hosting a small polaron in rutile. c | Energy dispersion of large electron polarons in anatase, as obtained by first-principle electron-phonon-coupling calculations (left) and ARPES measurements (right). d | Phase diagram of polarons in anatase. Figure adapted from Refs. 42, 47, 51, 266, 284.

properties^{58,95,310,314}. At high polaron density, the repulsive polaron-polaron interaction determines an instability of the lattice structure, which may drive the system to a structural reconstruction^{42,244}. The diffusion of polarons has been reported by FPMD simulations to occur via nearest-neighbor hopping and via temporary delocalization (random flight model)^{95,124,127,312,315–317}. Concerning nearest neighbor hopping, two regimes have been reported, either diabatic⁹⁸ or adiabatic¹⁷⁸ (see also Fig. 1). Depending on the type of approximation used for the exchange and correlation functional, one or the other regime is favored¹³³, another critical example of the limits of numerical schemes to describe polaron properties⁹⁷.

In contrast to rutile, the formation of small polarons in anatase is more debated^{314,318}. DFT suggests that strong electron localization on bulk Ti sites is quite unfavorable in anatase, and would occur only when using unrealistic values for U or exchange mixing parameter^{49,92,133}, or on surfaces near lattice defects^{88,90,165,308,319,320}, or in nanoparticles³²¹. The trapping of immobile electronic states at lattice defects is also confirmed by UPS and ELS spectroscopies³²², and by surface-sensitive scanning-tunneling-microscopy experiments⁹⁴, which proposed a direct comparison with the distinct behavior of mobile small polarons on rutile⁴⁹ (see Fig. 8). Finally, singly ionized O^- species appear in EPR experiments upon hole doping in anatase, but these states are strongly bound to the defects rather than showing the mobility common to polarons³²³.

Interestingly, anatase seems instead more adapt to host large electron polarons, as suggested by the dispersed spatial extent of unpaired electron wavefunctions obtained by the EPR hyperfine signal³²⁴, and by electrical conductivity³²⁵ and dielectric function³²⁶ measurements (see Fig. 5). ARPES⁵¹ and RIXS³²⁷ data reveal shallow states below the conduction band, which can be attributed to large polaron satellites, as recently confirmed by first principles calculations accounting for the Frölich electron-phonon coupling⁴⁷ (see Fig. 9c). STM experiments reveal a large-polaron-like dispersion of the electronic charge on the anatase surface if donors affect the lattice structure only slightly (as in case of Nb substitutional doping, reported in Fig. 8, as opposed to the strongly-localized states trapped at V_O sites)⁴⁹. Moreover, magneto transport experiments identified a

phase transition going from a Fröhlich polaron regime to Fermi liquid, depending on the concentration of excess charge²⁸⁴ (see Fig. 9d).

Polarons in halide perovskites

Within the past decade, metal halide perovskites (MHPs) have emerged as a most appealing class of materials for optoelectronics, and have spurred intense research activities, ongoing to this date³²⁸. While this review is not the proper context to survey the latest developments, charge trapping and polaron formation have a large impact on the carrier transport in MHP. The following is thus intended to succinctly review the major highlights of this ongoing debate. For a more comprehensive discussion the interested reader is referred to recent reviews on this topic^{174,220}.

There is a general computational and experimental consensus that both small and large polarons can form in MHPs^{31,329–331} (see Figs. 4 and 6 for large polaron formation in MHPs) but how polarons affect carrier mobility is still a controversial issue. Small polarons are believed to have detrimental effects on MHPs causing photo- and material-degradation as well as the formation of macroscopic charge domains, which hinder efficient charge extraction in solar cell devices.¹⁷⁴ Conversely, long carrier lifetimes and diffusion lengths measured in MHPs have been associated with formation of large polarons. In fact, with their large effective mass (10–300 m_e at room temperature, with m_e being the mass of the free electron) and long coherence length, large polarons are believed to protect other carriers from scattering with longitudinal phonons³³². Moreover, large polarons have been invoked as a possible explanation of the low recombination rate in MHPs³³³: if the static dielectric constant is large enough the interaction between oppositely charged large polarons at short distance can become repulsive, thereby impeding electron-hole recombination (see also Fig. 3).

An interesting and still unresolved issue is the mechanism that favors either small or large polarons in MHPs. First principles calculations on mixed Lead-Tin HPs found that the modification of the metal halide bonds, correlated with the formation of small (short bond) or large (long bonds) polarons, can be controlled by chemical doping, suggesting that increasing Sn concentration should result in a progressive shift from a small to large polaron scenario³³⁴. Similar conclusions on the effect of cation alloying on the polaron binding energies has been obtained for Cs substitution in PbI_3 -based MHPs, which can be exploited to mitigate the formation of small polaron and therefore reduce their detrimental consequences on charge transport³³⁵.

This interaction between polarons and local structural distortions has also revealed that the binding energy of small electron polarons is significantly larger than the one of hole polarons. It is also enhanced by the coupling with local Jahn-Teller distortions in the metal halide octahedra³³⁶, leading to the formation of the already mentioned JT polaron (see Fig. 4).

These are not the only types of polarons detected in MHPs not directly categorizable as conventional small/large polarons. Evidence for the onset of ferroelectric large polaron has been put forward in Refs.^{31,48}, and even more attention has been devoted to the study of exciton polarons. Based on an effective exciton-phonon Hamiltonian, Kandanda and Silva found that a strong exciton-phonon scattering processes should develop when the excitonic binding energy is $\approx \hbar\omega_{LO}$ and the effective mass of electrons and holes are very different. Since these conditions are not fulfilled in 2D MHPs where exciton polarons form (manifested in the excitonic spectral structure), it was proposed that in the 2D limit the formation of exciton polarons is favored by the transformation of the electronic-vibrational landscape, in particular related to the enhancement of short-range-type el-ph interactions²²⁰. As a consequence, the resulting exciton polaron falls in an intermediate regime between the Fröhlich (long-range) and self-trapping (short-range) limits.

A final word before moving to the conclusive outlook. There have been many, sometimes contradictory, hypotheses on the nature and characteristic of polarons in MHPs, most of them derived from computational studies at ideal conditions or from approximated semi-empirical theories. It is the opinion of these authors that the time has come to filter this large amount of data and seek for solid experimental verification and for a complete theoretical treatment in order to achieve a rigorous description and understanding of the role of polarons in charge transport in these materials.

Outlook

As this review has amply shown, the interest in polaron effects in materials is still increasing. It spans theoretical and numerical foundations, emerging experimental probes, and functionalization for a variety of applications. A most interesting development is the growing effort to bridge and connect historically distant research communities in an effort to establish a common playground and a standard language to study and understand the multifaceted complexity of polarons. A prime example in this direction is the merger of Fröhlich and Pekar's formulations into a materials-specific first principles DFT framework^{14,67,73}. A natural, albeit challenging, further development is joining quantum-field theory and *ab initio* methods; this would lead to a genuinely *ab initio* many-body theory of polarons. One of the most promising route to such a unified formalism is the connection between DFT and DiagMC, where all terms of the general polaron Hamiltonian are calculated from first principles. As an added benefit, this combination would transcend the Holstein-Fröhlich (or lattice/continuum) dichotomy, as the electron-phonon coupling term would be treated entirely from first principles, simultaneously including both, small-range and long-range interactions.

Another timely research line that will most likely be explored in coming years involves the extension to larger time/length scales in simulations of polaron properties. We expect that much effort will be devoted to the implementation of efficient, long-range electron-phonon coupling and electron-electron interaction terms in multiscale schemes. Even more attractive is the possibility to accelerate the calculation of polaron properties with machine learning (ML) techniques^{337,338}. For instance, ML could be employed to overtake the prohibitive limits of MD to explore the polaronic configuration space (finding the most probable polaron sites), which would help tremendously in the study and prediction of transport effects³³⁹. Different data driven approaches could be explored to tackle this problem, including atomistic neural networks potential³⁴⁰, kernel ridge regression³⁴¹, or machine learned force field³⁴².

The rapid development in microscopic techniques affords the possibility to image polarons in real space, and could provide a fertile area where innovations in theory and experiment complement each other in an ideal way. As recent examples show^{42,49,244}, imaging single electron polarons is well on its way; at this point similar experiments on hole polarons have not yet been reported but could provide truly novel information. Considering that polaron effects are predominant at the surfaces of materials and manifest themselves with charge confinements detectable by STM and AFM, one could envisage using computer vision methods such as local-structural-state algorithms and agglomerative clustering algorithms³⁴³ to interpret experimental images³⁴⁴.

With shorter and shorter time scales accessible in experiments, the possibility to inspect and follow polaron dynamics opens up another exciting area of research. Ultrafast, x-ray based spectroscopies will further evolve in coming years, and will provide powerful, novel ways to address pending issues in polaron physics such as the clarification of the time-scales in polaron-related excitations, or the time needed for formation and recombination. In this context development of coherent and highly brilliant x-ray lasers promise exciting opportunities, as they enable experiments that address both, extremely short time scales and, by taking advantage of core-hole resonance techniques, also very small length scales.

Of extreme interest, for both theory and experiment, is the possibility to control and functionalize polarons. High-resolution nc-AFM emerges as promising technique that is potentially capable to detect and manipulate the charge²⁷⁶ and spin³⁴⁵ of single electrons. The application of an external electric or magnetic field could open additional channels to act on polaron charge and polaron spin, possibly resulting in a controlled tunability of static and dynamic properties (e.g. coherent polaron motion, polaron clustering, polaron excitations, or formation of spin-polaron lattices, to name just a few). The possibility to create a well-defined polaron (spin-)lattice, for instance, could be used to study the onset of spin-liquid states (in this case spin-polaron liquid) or, even more visionary, spin-polaron confinement could be engineered as an alternative to electron spins in semiconductor quantum dots for quantum information processing.

Regarding novel materials, hybrid perovskites, 2D materials and organic semiconductors represent one of the most exciting front where the role of polarons (in particular dielectric and exciton polarons) is crucial to understand charge transport (and related energy-conversion applications) in these materials.

On the applied side, there is currently a rapid search for efficient thermoelectric generators and Peltier elements³⁴⁶. Novel devices based on ionic crystals nowadays considerably supersede traditional metal-based generators.³⁴⁶ Electron-phonon coupling and polarons contribute to all parameters relevant for thermoelectric generators including the Seebeck effect, electrical conductivity, and heat conduction. Generally, materials with high carrier mobility tend to be more efficient thermoelectrics, meaning that control over polaron formation and dynamics is surely beneficial to device performance.

Molecular functionalization is another possibility to modify polaron-related properties and therefore materials functionalities. For example the polaron formation rate and polaron activation energy can be tuned by molecular absorption³⁴⁷. More generally, polaron-molecule interactions can dramatically change the chemical reactivity of materials, and it is foreseeable that future studies will explore the possibility to customize catalytic activity through direct control of polaron-related energetics.

The field of polaron physics has commenced several decades ago, yet it feels new and exciting. Despite massive research on these quasiparticles, we are only at the beginning of fully understanding their properties and exploiting them for future use.

References

1. Alexandrov, A. S. & Devreese, J. T. *Advances in Polaron Physics* (Springer, 2010).
2. Bredas, J. L. & Street, G. B. Polarons, bipolarons, and solitons in conducting polymers. *Accounts Chem. Res.* **18**, 309–315, DOI: [10.1021/ar00118a005](https://doi.org/10.1021/ar00118a005) (1985).
3. Reticcioli, M., Diebold, U., Kresse, G. & Franchini, C. *Small Polarons in Transition Metal Oxides*, 1–39 (Springer International Publishing, Cham, 2019).
4. Pekar, S. I. *Zh. Eksp. Teor. Fiz* **16**, 341 (1946).
5. Dykman, M. & Rashba, E. The roots of polaron theory. *Phys. Today* **68**, 10, DOI: [10.1063/PT.3.2897](https://doi.org/10.1063/PT.3.2897) (2015).
6. Landau, L. D. über die bewegung der elektronen im kristallgitter. *Phys. Z. Sowjet.* **664** (1933).

7. Fröhlich, H., Pelzer, H. & Zienau, S. XX. properties of slow electrons in polar materials. *The London, Edinburgh, Dublin Philos. Mag. J. Sci.* **41**, 221–242, DOI: [10.1080/14786445008521794](https://doi.org/10.1080/14786445008521794) (1950). <https://doi.org/10.1080/14786445008521794>.
8. Fröhlich, H., Pelzer, H. & Zienau, S. *Philos. Mag.* **41**, 221 (1950).
9. Fröhlich, H. Electrons in lattice fields. *Adv. Phys.* **3**, 325–361, DOI: [10.1080/00018735400101213](https://doi.org/10.1080/00018735400101213) (1954). <https://doi.org/10.1080/00018735400101213>.
10. Holstein, T. *Ann. Phys.* **8**, 325 (1959).
11. Holstein, T. *Ann. Phys.* **8**, 343 (1959).
12. Feynman, R. P. Slow electrons in a polar crystal. *Phys. Rev.* **97**, 660–665, DOI: [10.1103/PhysRev.97.660](https://doi.org/10.1103/PhysRev.97.660) (1955).
13. Ōsaka, Y. Polaron State at a Finite Temperature. *Prog. Theor. Phys.* **22**, 437–446, DOI: [10.1143/PTP.22.437](https://academic.oup.com/ptp/article-pdf/22/3/437/5279184/22-3-437.pdf) (1959). <https://academic.oup.com/ptp/article-pdf/22/3/437/5279184/22-3-437.pdf>.
14. Sio, W. H., Verdi, C., Poncé, S. & Giustino, F. Ab initio theory of polarons: Formalism and applications. *Phys. Rev. B* **99**, 235139, DOI: [10.1103/PhysRevB.99.235139](https://doi.org/10.1103/PhysRevB.99.235139) (2019).
15. Alexandrov, A. S. *Polarons in Advanced Materials* (Springer, 2007).
16. Nagels, P., Denayer, M. & Devreese, J. Electrical properties of single crystals of uranium dioxide. *Solid State Commun.* **1**, 35 – 40, DOI: [https://doi.org/10.1016/0038-1098\(63\)90388-0](https://doi.org/10.1016/0038-1098(63)90388-0) (1963).
17. Crevecoeur, C. & Wit, H. D. Electrical conductivity of li doped mno. *J. Phys. Chem. Solids* **31**, 783 – 791, DOI: [https://doi.org/10.1016/0022-3697\(70\)90212-X](https://doi.org/10.1016/0022-3697(70)90212-X) (1970).
18. Stoneham, A. M. *et al.* Trapping, self-trapping and the polaron family. *J. Physics: Condens. Matter* **19**, 255208, DOI: [10.1088/0953-8984/19/25/255208](https://doi.org/10.1088/0953-8984/19/25/255208) (2007).
19. Coropceanu, V. *et al.* Charge transport in organic semiconductors. *Chem. Rev.* **107**, 926–952, DOI: [10.1021/cr050140x](https://doi.org/10.1021/cr050140x) (2007).
20. Zhugayevych, A. & Tretiak, S. Theoretical description of structural and electronic properties of organic photovoltaic materials. *Annu. Rev. Phys. Chem.* **66**, 305–330, DOI: [10.1146/annurev-physchem-040214-121440](https://doi.org/10.1146/annurev-physchem-040214-121440) (2015). PMID: 25580623, <https://doi.org/10.1146/annurev-physchem-040214-121440>.
21. *Polarons, Solitons, Excitons, and Conducting Polymers*, chap. 9, 301–401 (John Wiley & Sons, Ltd, 2019). <https://onlinelibrary.wiley.com/doi/pdf/10.1002/9783527816590.ch9>.
22. Cobet, C., Gasiorowski, J., Farka, D. & Stadler, P. *Polarons in Conjugated Polymers*, 355–387 (Springer International Publishing, Cham, 2018).
23. De Sio, A. *et al.* Tracking the coherent generation of polaron pairs in conjugated polymers. *Nat. Commun.* **7**, 13742, DOI: [10.1038/ncomms13742](https://doi.org/10.1038/ncomms13742) (2016).
24. Kaminski, A. & Das Sarma, S. Polaron percolation in diluted magnetic semiconductors. *Phys. Rev. Lett.* **88**, 247202, DOI: [10.1103/PhysRevLett.88.247202](https://doi.org/10.1103/PhysRevLett.88.247202) (2002).
25. Teresa, J. M. D. *et al.* Evidence for magnetic polarons in the magnetoresistive perovskites. *Nature* **386**, 256–259, DOI: [10.1038/386256a0](https://doi.org/10.1038/386256a0) (1997).
26. Zhou, J.-S. & Goodenough, J. B. Zener versus de Gennes ferromagnetism in $\text{La}_{1-x}\text{Sr}_x\text{MnO}_3$. *Phys. Rev. B* **62**, 3834–3838, DOI: [10.1103/PhysRevB.62.3834](https://doi.org/10.1103/PhysRevB.62.3834) (2000).
27. Daoud-Aladine, A., Rodríguez-Carvajal, J., Pinsard-Gaudart, L., Fernández-Díaz, M. T. & Revcolevschi, A. Zener polaron ordering in half-doped manganites. *Phys. Rev. Lett.* **89**, 097205, DOI: [10.1103/PhysRevLett.89.097205](https://doi.org/10.1103/PhysRevLett.89.097205) (2002).
28. Yamada, Y. *et al.* Polaron ordering in low-doping $\text{La}_{1-x}\text{Sr}_x\text{MnO}_3$. *Phys. Rev. Lett.* **77**, 904–907, DOI: [10.1103/PhysRevLett.77.904](https://doi.org/10.1103/PhysRevLett.77.904) (1996).
29. Zhao, G.-M., Hunt, M. B., Keller, H. & Müller, K. A. Evidence for polaronic supercarriers in the copper oxide superconductors $\text{La}_{2-x}\text{Sr}_x\text{CuO}_4$. *Nature* **385**, 236–239, DOI: [10.1038/385236a0](https://doi.org/10.1038/385236a0) (1997).
30. Cortecchia, D. *et al.* Polaron self-localization in white-light emitting hybrid perovskites. *J. Mater. Chem. C* **5**, 2771–2780, DOI: [10.1039/C7TC00366H](https://doi.org/10.1039/C7TC00366H) (2017).
31. Miyata, K. *et al.* Large polarons in lead halide perovskites. *Sci. Adv.* **3**, DOI: [10.1126/sciadv.1701217](https://doi.org/10.1126/sciadv.1701217) (2017). <https://advances.sciencemag.org/content/3/8/e1701217.full.pdf>.

32. Chen, Q., Wang, W. & Peeters, F. M. Magneto-polarons in monolayer transition-metal dichalcogenides. *J. Appl. Phys.* **123**, 214303, DOI: [10.1063/1.5025907](https://doi.org/10.1063/1.5025907) (2018). <https://doi.org/10.1063/1.5025907>.
33. Kang, M. *et al.* Holstein polaron in a valley-degenerate two-dimensional semiconductor. *Nat. Mater.* **17**, 676–680, DOI: [10.1038/s41563-018-0092-7](https://doi.org/10.1038/s41563-018-0092-7) (2018).
34. McKenna, K. P., Wolf, M. J., Shluger, A. L., Lany, S. & Zunger, A. Two-dimensional polaronic behavior in the binary oxides $m\text{-HfO}_2$ and $m\text{-ZrO}_2$. *Phys. Rev. Lett.* **108**, 116403, DOI: [10.1103/PhysRevLett.108.116403](https://doi.org/10.1103/PhysRevLett.108.116403) (2012).
35. Natanzon, Y., Azulay, A. & Amouyal, Y. Evaluation of polaron transport in solids from first-principles. *Isr. J. Chem.* **n/a**, DOI: [10.1002/ijch.201900101](https://onlinelibrary.wiley.com/doi/pdf/10.1002/ijch.201900101). <https://onlinelibrary.wiley.com/doi/pdf/10.1002/ijch.201900101>.
36. Nelson, J., Kwiatkowski, J. J., Kirkpatrick, J. & Frost, J. M. Modeling charge transport in organic photovoltaic materials. *Accounts Chem. Res.* **42**, 1768–1778, DOI: [10.1021/ar900119f](https://doi.org/10.1021/ar900119f) (2009).
37. Ortmann, F., Bechstedt, F. & Hannewald, K. Charge transport in organic crystals: Theory and modelling. *physica status solidi (b)* **248**, 511–525, DOI: [10.1002/pssb.201046278](https://doi.org/10.1002/pssb.201046278) (2011). <https://onlinelibrary.wiley.com/doi/pdf/10.1002/pssb.201046278>.
38. Di Valentin, C., Pacchioni, G. & Selloni, A. Reduced and n -type doped TiO_2 : Nature of Ti^{3+} species. *The J. Phys. Chem. C* **113**, 20543–20552, DOI: [10.1021/jp9061797](https://doi.org/10.1021/jp9061797) (2009).
39. Papageorgiou, A. C. *et al.* Electron traps and their effect on the surface chemistry of $\text{TiO}_2(110)$. *Proc. Natl. Acad. Sci.* **107**, 2391–2396, DOI: [10.1073/pnas.0911349107](https://doi.org/10.1073/pnas.0911349107) (2010). <https://www.pnas.org/content/107/6/2391.full.pdf>.
40. Reticcioli, M. *et al.* Interplay between adsorbates and polarons: CO on rutile $\text{TiO}_2(110)$. *Phys. Rev. Lett.* **122**, 016805, DOI: [10.1103/PhysRevLett.122.016805](https://doi.org/10.1103/PhysRevLett.122.016805) (2019).
41. Yin, W.-J., Wen, B., Zhou, C., Selloni, A. & Liu, L.-M. Excess electrons in reduced rutile and anatase TiO_2 . *Surf. Sci. Reports* **73**, 58 – 82, DOI: <https://doi.org/10.1016/j.surfrep.2018.02.003> (2018).
42. Reticcioli, M. *et al.* Polaron-driven surface reconstructions. *Phys. Rev. X* **7**, 031053, DOI: [10.1103/PhysRevX.7.031053](https://doi.org/10.1103/PhysRevX.7.031053) (2017).
43. Millis, A. J., Mueller, R. & Shraiman, B. I. Fermi-liquid-to-polaron crossover. ii. double exchange and the physics of colossal magnetoresistance. *Phys. Rev. B* **54**, 5405–5417, DOI: [10.1103/PhysRevB.54.5405](https://doi.org/10.1103/PhysRevB.54.5405) (1996).
44. Swartz, A. G. *et al.* Polaronic behavior in a weak-coupling superconductor. *Proc. Natl. Acad. Sci.* **115**, 1475–1480, DOI: [10.1073/pnas.1713916115](https://doi.org/10.1073/pnas.1713916115) (2018). <https://www.pnas.org/content/115/7/1475.full.pdf>.
45. Zhang, S. *et al.* Enhanced superconducting state in $\text{FeSe}/\text{SrTiO}_3$ by a dynamic interfacial polaron mechanism. *Phys. Rev. Lett.* **122**, 066802, DOI: [10.1103/PhysRevLett.122.066802](https://doi.org/10.1103/PhysRevLett.122.066802) (2019).
46. Wang, M. *et al.* Thermoelectric seebeck effect in oxide-based resistive switching memory. *Nat. Commun.* **5**, 4598, DOI: [10.1038/ncomms5598](https://doi.org/10.1038/ncomms5598) (2014).
47. Verdi, C., Caruso, F. & Giustino, F. Origin of the crossover from polarons to fermi liquids in transition metal oxides. *Nat. Commun.* **8**, 15769, DOI: [10.1038/ncomms15769](https://doi.org/10.1038/ncomms15769) (2017).
48. Miyata, K. & Zhu, X.-Y. Ferroelectric large polarons. *Nat. Mater.* **17**, 379–381, DOI: [10.1038/s41563-018-0068-7](https://doi.org/10.1038/s41563-018-0068-7) (2018).
49. Setvin, M. *et al.* Direct view at excess electrons in TiO_2 rutile and anatase. *Phys. Rev. Lett.* **113**, 086402, DOI: [10.1103/PhysRevLett.113.086402](https://doi.org/10.1103/PhysRevLett.113.086402) (2014).
50. Dehn, M. H. *et al.* Observation of a charge-neutral muon-polaron complex in antiferromagnetic Cr_2O_3 . *Phys. Rev. X* **10**, 011036, DOI: [10.1103/PhysRevX.10.011036](https://doi.org/10.1103/PhysRevX.10.011036) (2020).
51. Moser, S. *et al.* Tunable polaronic conduction in anatase TiO_2 . *Phys. Rev. Lett.* **110**, 196403, DOI: [10.1103/PhysRevLett.110.196403](https://doi.org/10.1103/PhysRevLett.110.196403) (2013).
52. de Groot, F. & Kotani, A. *Core Level Spectroscopy of Solids* (CRC Press, 2008).
53. Di Valentin, C., Pacchioni, G., Selloni, A., Livraghi, S. & Giamello, E. Characterization of paramagnetic species in N-doped TiO_2 powders by epr spectroscopy and dft calculations. *The J. Phys. Chem. B* **109**, 11414–11419, DOI: [10.1021/jp051756t](https://doi.org/10.1021/jp051756t) (2005).
54. Yang, S., Brant, A. T., Giles, N. C. & Halliburton, L. E. Intrinsic small polarons in rutile TiO_2 . *Phys. Rev. B* **87**, 125201, DOI: [10.1103/PhysRevB.87.125201](https://doi.org/10.1103/PhysRevB.87.125201) (2013).

55. Rho, H. *et al.* Evolution of magnetic polarons and spin-carrier interactions through the metal-insulator transition in $\text{Eu}_{1-x}\text{Gd}_x\text{O}$. *Phys. Rev. Lett.* **88**, 127401, DOI: [10.1103/PhysRevLett.88.127401](https://doi.org/10.1103/PhysRevLett.88.127401) (2002).
56. Storchak, V. G. *et al.* Magnetic polarons in eu-based films of magnetic semiconductors. *Phys. Rev. B* **81**, 153201, DOI: [10.1103/PhysRevB.81.153201](https://doi.org/10.1103/PhysRevB.81.153201) (2010).
57. Matus, M., Kuzmany, H. & Sohmen, E. Self-trapped polaron exciton in neutral fullerene C_{60} . *Phys. Rev. Lett.* **68**, 2822–2825, DOI: [10.1103/PhysRevLett.68.2822](https://doi.org/10.1103/PhysRevLett.68.2822) (1992).
58. Sezen, H. *et al.* Probing electrons in TiO_2 polaronic trap states by IR-absorption: Evidence for the existence of hydrogenic states. *Sci. Reports* **4**, 3808, DOI: [10.1038/srep03808](https://doi.org/10.1038/srep03808) (2014).
59. Devreese, J. T., Klimin, S. N., van Mechelen, J. L. M. & van der Marel, D. Many-body large polaron optical conductivity in $\text{SrTi}_{1-x}\text{Nb}_x\text{O}_3$. *Phys. review. B, Condens. matter* **81**, 1252–9, DOI: [10.1103/PhysRevB.81.125119](https://doi.org/10.1103/PhysRevB.81.125119) (2010).
60. Klimin, S., Tempere, J., Devreese, J. T., Franchini, C. & Kresse, G. Optical response of an interacting polaron gas in strongly polar crystals. *Appl. Sci.* **10**, 2059, DOI: [10.3390/app10062059](https://doi.org/10.3390/app10062059) (2020).
61. Prokof'ev, N. V. & Svistunov, B. V. Polaron problem by diagrammatic quantum monte carlo. *Phys. Rev. Lett.* **81**, 2514–2517, DOI: [10.1103/PhysRevLett.81.2514](https://doi.org/10.1103/PhysRevLett.81.2514) (1998).
62. Mishchenko, A. S., Prokof'ev, N. V., Sakamoto, A. & Svistunov, B. V. Diagrammatic quantum monte carlo study of the fröhlich polaron. *Phys. Rev. B* **62**, 6317–6336, DOI: [10.1103/PhysRevB.62.6317](https://doi.org/10.1103/PhysRevB.62.6317) (2000).
63. Titantah, J. T., Pierleoni, C. & Ciuchi, S. Free energy of the Fröhlich polaron in two and three dimensions. *Phys. Rev. Lett.* **87**, 206406, DOI: [10.1103/PhysRevLett.87.206406](https://doi.org/10.1103/PhysRevLett.87.206406) (2001).
64. Bredow, T. & Pacchioni, G. Electronic structure of an isolated oxygen vacancy at the $\text{TiO}_2(110)$ surface. *Chem. Phys. Lett.* **355**, 417 – 423, DOI: [10.1016/S0009-2614\(02\)00259-2](https://doi.org/10.1016/S0009-2614(02)00259-2) (2002).
65. Lany, S. & Zunger, A. Polaronic hole localization and multiple hole binding of acceptors in oxide wide-gap semiconductors. *Phys. Rev. B* **80**, 085202, DOI: [10.1103/PhysRevB.80.085202](https://doi.org/10.1103/PhysRevB.80.085202) (2009).
66. Kokott, S., Levchenko, S. V., Rinke, P. & Scheffler, M. First-principles supercell calculations of small polarons with proper account for long-range polarization effects. *New J. Phys.* **20**, 033023, DOI: [10.1088/1367-2630/aaaf44](https://doi.org/10.1088/1367-2630/aaaf44) (2018).
67. Verdi, C. & Giustino, F. Fröhlich electron-phonon vertex from first principles. *Phys. Rev. Lett.* **115**, 176401, DOI: [10.1103/PhysRevLett.115.176401](https://doi.org/10.1103/PhysRevLett.115.176401) (2015).
68. Ciuchi, S., de Pasquale, F. & Feinberg, D. *Eur. Lett.* **30**, 151 (1995).
69. Ciuchi, S., de Pasquale, F., Fratini, S. & Feinberg, D. Dynamical mean-field theory of the small polaron. *Phys. Rev. B* **56**, 4494–4512, DOI: [10.1103/PhysRevB.56.4494](https://doi.org/10.1103/PhysRevB.56.4494) (1997).
70. Fratini, S. & Ciuchi, S. Dynamical mean-field theory of transport of small polarons. *Phys. Rev. Lett.* **91**, 256403, DOI: [10.1103/PhysRevLett.91.256403](https://doi.org/10.1103/PhysRevLett.91.256403) (2003).
71. Kerisit, S. & Rosso, K. M. Kinetic monte carlo model of charge transport in hematite ($\alpha\text{-Fe}_2\text{O}_3$). *The J. Chem. Phys.* **127**, 124706, DOI: [10.1063/1.2768522](https://doi.org/10.1063/1.2768522) (2007). <https://doi.org/10.1063/1.2768522>.
72. Wolf, M. J., Irvine, L. A. D. & Walker, A. B. Quantifying polaronic effects on charge-carrier scattering and mobility in lead-halide perovskite. *ArXiv* (2020). [arXiv:2003.00968](https://arxiv.org/abs/2003.00968).
73. Sio, W. H., Verdi, C., Poncé, S. & Giustino, F. Polarons from first principles, without supercells. *Phys. Rev. Lett.* **122**, 246403, DOI: [10.1103/PhysRevLett.122.246403](https://doi.org/10.1103/PhysRevLett.122.246403) (2019).
74. Gono, P., Wiktor, J., Ambrosio, F. & Pasquarello, A. Surface polarons reducing overpotentials in the oxygen evolution reaction. *ACS Catal.* **8**, 5847–5851, DOI: [10.1021/acscatal.8b01120](https://doi.org/10.1021/acscatal.8b01120) (2018). <https://doi.org/10.1021/acscatal.8b01120>.
75. Zhang, D., Han, Z.-K., Murgida, G. E., Ganduglia-Pirovano, M. V. & Gao, Y. Oxygen-vacancy dynamics and entanglement with polaron hopping at the reduced $\text{CeO}_2(111)$ surface. *Phys. Rev. Lett.* **122**, 096101, DOI: [10.1103/PhysRevLett.122.096101](https://doi.org/10.1103/PhysRevLett.122.096101) (2019).
76. Bombile, J. H., Janik, M. J. & Milner, S. T. Polaron formation mechanisms in conjugated polymers. *Phys. Chem. Chem. Phys.* **20**, 317–331, DOI: [10.1039/C7CP04355D](https://doi.org/10.1039/C7CP04355D) (2018).
77. Yuan, S., Wang, Z., Baron, M. L. F. & Bevan, K. H. Ab initio insight into the formation of small polarons: A study across four metal peroxides. *Phys. Rev. B* **100**, 205201, DOI: [10.1103/PhysRevB.100.205201](https://doi.org/10.1103/PhysRevB.100.205201) (2019).
78. Gerosa, M., Gygi, F., Govoni, M. & Galli, G. The role of defects and excess surface charges at finite temperature for optimizing oxide photoabsorbers. *Nat. Mater.* **17**, 1122–1127, DOI: [10.1038/s41563-018-0192-4](https://doi.org/10.1038/s41563-018-0192-4) (2018).

79. Nery, J. P. *et al.* Quasiparticles and phonon satellites in spectral functions of semiconductors and insulators: Cumulants applied to the full first-principles theory and the Fröhlich polaron. *Phys. Rev. B* **97**, 115145, DOI: [10.1103/PhysRevB.97.115145](https://doi.org/10.1103/PhysRevB.97.115145) (2018).
80. Mora-Fonz, D. & Shluger, A. L. Modeling of intrinsic electron and hole trapping in crystalline and amorphous ZnO. *Adv. Electron. Mater.* **6**, 1900760, DOI: [10.1002/aelm.201900760](https://doi.org/10.1002/aelm.201900760) (2020). <https://onlinelibrary.wiley.com/doi/pdf/10.1002/aelm.201900760>.
81. Huang, H. Y. *et al.* Jahn-teller distortion driven magnetic polarons in magnetite. *Nat. Commun.* **8**, 15929, DOI: [10.1038/ncomms15929](https://doi.org/10.1038/ncomms15929) (2017).
82. Zhou, J.-J. & Bernardi, M. Predicting charge transport in the presence of polarons: The beyond-quasiparticle regime in SrTiO₃. *Phys. Rev. Res.* **1**, 033138, DOI: [10.1103/PhysRevResearch.1.033138](https://doi.org/10.1103/PhysRevResearch.1.033138) (2019).
83. Mishchenko, A. S. *et al.* Polaron mobility in the “beyond quasiparticles” regime. *Phys. Rev. Lett.* **123**, 076601, DOI: [10.1103/PhysRevLett.123.076601](https://doi.org/10.1103/PhysRevLett.123.076601) (2019).
84. Ismail, A. S. M. *et al.* Direct observation of the electronic states of photoexcited hematite with ultrafast 2p3d X-ray absorption spectroscopy and resonant inelastic X-ray scattering. *Phys. Chem. Chem. Phys.* **22**, 2685–2692, DOI: [10.1039/C9CP03374B](https://doi.org/10.1039/C9CP03374B) (2020).
85. Pastor, E. *et al.* In situ observation of picosecond polaron self-localisation in a-Fe₂O₃ photoelectrochemical cells. *Nat. Commun.* **10**, 3962, DOI: [10.1038/s41467-019-11767-9](https://doi.org/10.1038/s41467-019-11767-9) (2019).
86. Selcuk, S. & Selloni, A. Facet-dependent trapping and dynamics of excess electrons at anatase TiO₂ surfaces and aqueous interfaces. *Nat. Mater.* **15**, 1107–1112, DOI: [10.1038/nmat4672](https://doi.org/10.1038/nmat4672) (2016).
87. Yim, C. M. *et al.* Visualization of water-induced surface segregation of polarons on rutile TiO₂(110). *The J. Phys. Chem. Lett.* **9**, 4865–4871, DOI: [10.1021/acs.jpcclett.8b01904](https://doi.org/10.1021/acs.jpcclett.8b01904) (2018). PMID: 30081626, <https://doi.org/10.1021/acs.jpcclett.8b01904>.
88. Deák, P., Aradi, B. & Frauenheim, T. Polaronic effects in tio₂ calculated by the hse06 hybrid functional: Dopant passivation by carrier self-trapping. *Phys. Rev. B* **83**, 155207, DOI: [10.1103/PhysRevB.83.155207](https://doi.org/10.1103/PhysRevB.83.155207) (2011).
89. Morgan, B. J., Scanlon, D. O. & Watson, G. W. Small polarons in Nb- and Ta-doped rutile and anatase TiO₂. *J. Mater. Chem.* **19**, 5175–5178, DOI: [10.1039/B905028K](https://doi.org/10.1039/B905028K) (2009).
90. Morgan, B. J. & Watson, G. W. Intrinsic *n*-type defect formation in TiO₂: A comparison of rutile and anatase from GGA+U calculations. *The J. Phys. Chem. C* **114**, 2321–2328, DOI: [10.1021/jp9088047](https://doi.org/10.1021/jp9088047) (2010). <https://doi.org/10.1021/jp9088047>.
91. Janotti, A., Varley, J. B., Choi, M. & Van de Walle, C. G. Vacancies and small polarons in srtio₃. *Phys. Rev. B* **90**, 085202, DOI: [10.1103/PhysRevB.90.085202](https://doi.org/10.1103/PhysRevB.90.085202) (2014).
92. Elmaslmane, A. R., Watkins, M. B. & McKenna, K. P. First-principles modeling of polaron formation in tio2 polymorphs. *J. Chem. Theory Comput.* **14**, 3740–3751, DOI: [10.1021/acs.jctc.8b00199](https://doi.org/10.1021/acs.jctc.8b00199) (2018). PMID: 29874462, <https://doi.org/10.1021/acs.jctc.8b00199>.
93. Rousseau, R., Glezakou, V.-A. & Selloni, A. Theoretical insights into the surface physics and chemistry of redox-active oxides. *Nat. Rev. Mater.* DOI: [10.1038/s41578-020-0198-9](https://doi.org/10.1038/s41578-020-0198-9) (2020).
94. Setvin, M. *et al.* Charge trapping at the step edges of TiO₂ anatase (101). *Angewandte Chemie Int. Ed.* **53**, 4714–4716, DOI: [10.1002/anie.201309796](https://doi.org/10.1002/anie.201309796) (2014). <https://onlinelibrary.wiley.com/doi/pdf/10.1002/anie.201309796>.
95. Reticcioli, M., Setvin, M., Schmid, M., Diebold, U. & Franchini, C. Formation and dynamics of small polarons on the rutile TiO₂(110) surface. *Phys. Rev. B* **98**, 045306, DOI: [10.1103/PhysRevB.98.045306](https://doi.org/10.1103/PhysRevB.98.045306) (2018).
96. Sokolović, I. *et al.* Resolving the adsorption of molecular O₂ on the rutile TiO₂ (110) surface by noncontact atomic force microscopy. *Proc. Natl. Acad. Sci.* **2**, 201922452, DOI: [10.1073/pnas.1922452117](https://doi.org/10.1073/pnas.1922452117) (2020).
97. Castleton, C. W. M., Lee, A. & Kullgren, J. Benchmarking density functional theory functionals for polarons in oxides: Properties of CeO₂. *The J. Phys. Chem. C* **123**, 5164–5175, DOI: [10.1021/acs.jpcc.8b09134](https://doi.org/10.1021/acs.jpcc.8b09134) (2019). <https://doi.org/10.1021/acs.jpcc.8b09134>.
98. Deskins, N. A. & Dupuis, M. Electron transport via polaron hopping in bulk TiO₂: A density functional theory characterization. *Phys. Rev. B* **75**, 195212, DOI: [10.1103/PhysRevB.75.195212](https://doi.org/10.1103/PhysRevB.75.195212) (2007).
99. Pekar, S. I. *Zh. Eksp. Teor. Fiz* **17**, 868 (1947).
100. Pekar, S. I. *Zh. Eksp. Teor. Fiz* **18**, 105 (1948).

101. Landau, L. D. & Pekar, S. I. *Zh. Eksp. Teor. Fiz* **18**, 419 (1948).
102. Lee, T. D., Low, F. E. & Pines, D. The motion of slow electrons in a polar crystal. *Phys. Rev.* **90**, 297–302, DOI: [10.1103/PhysRev.90.297](https://doi.org/10.1103/PhysRev.90.297) (1953).
103. Zienau, S. *E. R. A. Rep. L/T236* (1950).
104. Hellwarth, R. W. & Biaggio, I. Mobility of an electron in a multimode polar lattice. *Phys. Rev. B* **60**, 299–307, DOI: [10.1103/PhysRevB.60.299](https://doi.org/10.1103/PhysRevB.60.299) (1999).
105. Rosenfelder, R. & Schreiber, A. On the best quadratic approximation in feynman's path integral treatment of the polaron. *Phys. Lett. A* **284**, 63 – 71, DOI: [https://doi.org/10.1016/S0375-9601\(01\)00287-0](https://doi.org/10.1016/S0375-9601(01)00287-0) (2001).
106. Frost, J. M. Calculating polaron mobility in halide perovskites. *Phys. Rev. B* **96**, 195202, DOI: [10.1103/PhysRevB.96.195202](https://doi.org/10.1103/PhysRevB.96.195202) (2017).
107. Gelfand, J. M. & Chentsov, N. N. *Zh.Eksp.Teor.Fiz* **3**, 1106 (1956).
108. Sabelfeld, K. K. *USSR Comput. Math. Phys.* **19**, 27 (1980).
109. Becker, W., Gerlach, B. & Schliffke, H. Monte carlo calculation of the ground-state energy of an optical polaron. *Phys. Rev. B* **28**, 5735–5738, DOI: [10.1103/PhysRevB.28.5735](https://doi.org/10.1103/PhysRevB.28.5735) (1983).
110. Yamashita, J. & Kurosawa, T. On electronic current in nio. *J. Phys. Chem. Solids* **5**, 34 – 43, DOI: [https://doi.org/10.1016/0022-3697\(58\)90129-X](https://doi.org/10.1016/0022-3697(58)90129-X) (1958).
111. Sewell, G. L. *Phil. Mag.* **3**, 1361 (1958).
112. Lang, I. G. & Firsov, Y. A. Kinetic theory of semiconductors with low mobility. *Sov. Phys. JETP* **16**, 1301 (1962).
113. Lang, I. G. & Firsov, Y. A. *Zh. Eksp. Teor. Fiz* **45**, 378 (1963).
114. Rongsheng, H., Zijing, L. & Keli, W. Exact solutions for the two-site holstein model. *Phys. Rev. B* **65**, 174303, DOI: [10.1103/PhysRevB.65.174303](https://doi.org/10.1103/PhysRevB.65.174303) (2002).
115. Tayebi, A. & Zelevinsky, V. The holstein polaron problem revisited. *J. Phys. A: Math. Theor.* **49**, 255004, DOI: [10.1088/1751-8113/49/25/255004](https://doi.org/10.1088/1751-8113/49/25/255004) (2016).
116. Emin, D. & Holstein, T. Studies of small-polaron motion IV. adiabatic theory of the Hall effect. *Annals Phys.* **53**, 439 – 520, DOI: [https://doi.org/10.1016/0003-4916\(69\)90034-7](https://doi.org/10.1016/0003-4916(69)90034-7) (1969).
117. Holstein, T. Studies of polaron motion: Part II. the “small” polaron. *Annals Phys.* **281**, 725 – 773, DOI: <https://doi.org/10.1006/aphy.2000.6021> (2000).
118. Austin, I. G. & Mott, N. F. Polarons in crystalline and non-crystalline materials. *Adv. Phys.* **50**, 757–812, DOI: [10.1080/00018730110103249](https://doi.org/10.1080/00018730110103249) (2001). <https://doi.org/10.1080/00018730110103249>.
119. Brunschwig, B. S., Logan, J., Newton, M. D. & Sutin, N. A semiclassical treatment of electron-exchange reactions. application to the hexaaquoiron(II)-hexaaquoiron(III) system. *J. Am. Chem. Soc.* **102**, 5798–5809, DOI: [10.1021/ja00538a017](https://doi.org/10.1021/ja00538a017) (1980). <https://doi.org/10.1021/ja00538a017>.
120. Marcus, R. A. & Sutin, N. *Biochim. Biophys. Acta* **811**, 265 (1985).
121. Marcus, R. A. Electron transfer reactions in chemistry. theory and experiment. *Rev. Mod. Phys.* **65**, 599–610, DOI: [10.1103/RevModPhys.65.599](https://doi.org/10.1103/RevModPhys.65.599) (1993).
122. Alexandrov, A. S., Kabanov, V. V. & Ray, D. K. From electron to small polaron: An exact cluster solution. *Phys. Rev. B* **49**, 9915–9923, DOI: [10.1103/PhysRevB.49.9915](https://doi.org/10.1103/PhysRevB.49.9915) (1994).
123. Mackrodt, W., Simson, E.-A. & Harrison, N. An ab initio Hartree-Fock study of the electron-excess gap states in oxygen-deficient rutile TiO₂. *Surf. Sci.* **384**, 192 – 200, DOI: [https://doi.org/10.1016/S0039-6028\(97\)00219-7](https://doi.org/10.1016/S0039-6028(97)00219-7) (1997).
124. Nelson, J. Continuous-time random-walk model of electron transport in nanocrystalline TiO₂ electrodes. *Phys. Rev. B* **59**, 15374–15380, DOI: [10.1103/PhysRevB.59.15374](https://doi.org/10.1103/PhysRevB.59.15374) (1999).
125. Tempere, J. & Devreese, J. T. Optical absorption of an interacting many-polaron gas. *Phys. Rev. B* **64**, 104504, DOI: [10.1103/PhysRevB.64.104504](https://doi.org/10.1103/PhysRevB.64.104504) (2001).
126. Lemmens, L. F., Brosens, F. & Devreese, J. T. On the ground state energy of a gas of interacting polarons. *Phys. status solidi (b)* **82**, 439–447, DOI: [10.1002/pssb.2220820204](https://doi.org/10.1002/pssb.2220820204) (1977). <https://onlinelibrary.wiley.com/doi/pdf/10.1002/pssb.2220820204>.

127. Kowalski, P. M., Camellone, M. F., Nair, N. N., Meyer, B. & Marx, D. Charge localization dynamics induced by oxygen vacancies on the $\text{TiO}_2(110)$ surface. *Phys. Rev. Lett.* **105**, 146405, DOI: [10.1103/PhysRevLett.105.146405](https://doi.org/10.1103/PhysRevLett.105.146405) (2010).
128. Di Valentin, C., Pacchioni, G. & Selloni, A. Electronic structure of defect states in hydroxylated and reduced rutile $\text{TiO}_2(110)$ surfaces. *Phys. Rev. Lett.* **97**, 166803, DOI: [10.1103/PhysRevLett.97.166803](https://doi.org/10.1103/PhysRevLett.97.166803) (2006).
129. Goodvin, G. L., Berciu, M. & Sawatzky, G. A. Green's function of the holstein polaron. *Phys. Rev. B* **74**, 245104, DOI: [10.1103/PhysRevB.74.245104](https://doi.org/10.1103/PhysRevB.74.245104) (2006).
130. Maxisch, T., Zhou, F. & Ceder, G. Ab initio study of the migration of small polarons in olivine Li_xFePO_4 and their association with lithium ions and vacancies. *Phys. Rev. B* **73**, 104301, DOI: [10.1103/PhysRevB.73.104301](https://doi.org/10.1103/PhysRevB.73.104301) (2006).
131. Nolan, M. & Watson, G. W. Hole localization in al doped silica: A dft+u description. *The J. Chem. Phys.* **125**, 144701, DOI: [10.1063/1.2354468](https://doi.org/10.1063/1.2354468) (2006). <https://doi.org/10.1063/1.2354468>.
132. Franchini, C., Kresse, G. & Podloucky, R. Polaronic hole trapping in doped BaBiO_3 . *Phys. Rev. Lett.* **102**, 256402, DOI: [10.1103/PhysRevLett.102.256402](https://doi.org/10.1103/PhysRevLett.102.256402) (2009).
133. Spreafico, C. & VandeVondele, J. The nature of excess electrons in anatase and rutile from hybrid DFT and RPA. *Phys. Chem. Chem. Phys.* **16**, 26144–26152, DOI: [10.1039/C4CP03981E](https://doi.org/10.1039/C4CP03981E) (2014).
134. Lany, S. Predicting polaronic defect states by means of generalized koopmans density functional calculations. *physica status solidi (b)* **248**, 1052–1060, DOI: [10.1002/pssb.201046274](https://doi.org/10.1002/pssb.201046274) (2011). <https://onlinelibrary.wiley.com/doi/pdf/10.1002/pssb.201046274>.
135. Grusdt, F. All-coupling theory for the Fröhlich polaron. *Phys. Rev. B* **93**, 144302, DOI: [10.1103/PhysRevB.93.144302](https://doi.org/10.1103/PhysRevB.93.144302) (2016).
136. Hohenadler, M., Evertz, H. G. & von der Linden, W. Quantum monte carlo and variational approaches to the Holstein model. *Phys. Rev. B* **69**, 024301, DOI: [10.1103/PhysRevB.69.024301](https://doi.org/10.1103/PhysRevB.69.024301) (2004).
137. Hahn, T., Klimin, S., Tempere, J., Devreese, J. T. & Franchini, C. Diagrammatic monte carlo study of fröhlich polaron dispersion in two and three dimensions. *Phys. Rev. B* **97**, 134305, DOI: [10.1103/PhysRevB.97.134305](https://doi.org/10.1103/PhysRevB.97.134305) (2018).
138. Mishchenko, A. S., Nagaosa, N. & Prokof'ev, N. Diagrammatic monte carlo method for many-polaron problems. *Phys. Rev. Lett.* **113**, 166402, DOI: [10.1103/PhysRevLett.113.166402](https://doi.org/10.1103/PhysRevLett.113.166402) (2014).
139. Diebold, U., Li, S.-C. & Schmid, M. Oxide surface science. *Annu. Rev. Phys. Chem.* **61**, 129–148, DOI: [10.1146/annurev.physchem.012809.103254](https://doi.org/10.1146/annurev.physchem.012809.103254) (2010). PMID: 20055675, <https://doi.org/10.1146/annurev.physchem.012809.103254>.
140. Van Houcke, K., Kozik, E., Prokof'ev, N. & Svistunov, B. Diagrammatic monte carlo. *Phys. Procedia* **6**, 95 – 105, DOI: <https://doi.org/10.1016/j.phpro.2010.09.034> (2010). Computer Simulations Studies in Condensed Matter Physics XXI.
141. Mishchenko, A. S. Diagrammatic monte carlo method as applied to the polaron problems. *Physics-Uspekhi* **48**, 887, DOI: [10.1070/PU2005v048n09ABEH002632](https://doi.org/10.1070/PU2005v048n09ABEH002632) (2005).
142. Mishchenko, A. S., De Filippis, G., Cataudella, V., Nagaosa, N. & Fehske, H. Optical signatures of exciton polarons from diagrammatic monte carlo. *Phys. Rev. B* **97**, 045141, DOI: [10.1103/PhysRevB.97.045141](https://doi.org/10.1103/PhysRevB.97.045141) (2018).
143. Hedin, L. New method for calculating the one-particle green's function with application to the electron-gas problem. *Phys. Rev.* **139**, A796–A823, DOI: [10.1103/PhysRev.139.A796](https://doi.org/10.1103/PhysRev.139.A796) (1965).
144. Ergönenc, Z., Kim, B., Liu, P., Kresse, G. & Franchini, C. Converged gw quasiparticle energies for transition metal oxide perovskites. *Phys. Rev. Mater.* **2**, 024601, DOI: [10.1103/PhysRevMaterials.2.024601](https://doi.org/10.1103/PhysRevMaterials.2.024601) (2018).
145. Becke, A. D. A new mixing of hartree–fock and local density-functional theories. *The J. Chem. Phys.* **98**, 1372–1377, DOI: [10.1063/1.464304](https://doi.org/10.1063/1.464304) (1993). <https://doi.org/10.1063/1.464304>.
146. Franchini, C. Hybrid functionals applied to perovskites. *J. Physics: Condens. Matter* **26**, 253202, DOI: [10.1088/0953-8984/26/25/253202](https://doi.org/10.1088/0953-8984/26/25/253202) (2014).
147. Anisimov, V. I., Zaanen, J. & Andersen, O. K. Band theory and Mott insulators: Hubbard U instead of Stoner I. *Phys. Rev. B* **44**, 943–954, DOI: [10.1103/PhysRevB.44.943](https://doi.org/10.1103/PhysRevB.44.943) (1991).
148. Himmetoglu, B., Floris, A., de Gironcoli, S. & Cococcioni, M. Hubbard-corrected DFT energy functionals: The LDA+U description of correlated systems. *Int. J. Quantum Chem.* **114**, 14–49, DOI: [10.1002/qua.24521](https://doi.org/10.1002/qua.24521) (2014). <https://onlinelibrary.wiley.com/doi/pdf/10.1002/qua.24521>.
149. Baroni, S., de Gironcoli, S., Dal Corso, A. & Giannozzi, P. Phonons and related crystal properties from density-functional perturbation theory. *Rev. Mod. Phys.* **73**, 515–562, DOI: [10.1103/RevModPhys.73.515](https://doi.org/10.1103/RevModPhys.73.515) (2001).

150. Giustino, F. Electron-phonon interactions from first principles. *Rev. Mod. Phys.* **89**, 015003, DOI: [10.1103/RevModPhys.89.015003](https://doi.org/10.1103/RevModPhys.89.015003) (2017).
151. Bjaalie, L. *et al.* Small hole polarons in rare-earth titanates. *Appl. Phys. Lett.* **106**, 232103, DOI: [10.1063/1.4922316](https://doi.org/10.1063/1.4922316) (2015). <https://doi.org/10.1063/1.4922316>.
152. Kohn, W. & Sham, L. J. Self-consistent equations including exchange and correlation effects. *Phys. Rev.* **140**, A1133–A1138, DOI: [10.1103/PhysRev.140.A1133](https://doi.org/10.1103/PhysRev.140.A1133) (1965).
153. Lejaeghere, K. *et al.* Reproducibility in density functional theory calculations of solids. *Science* **351**, DOI: [10.1126/science.aad3000](https://doi.org/10.1126/science.aad3000) (2016). <https://science.sciencemag.org/content/351/6280/aad3000.full.pdf>.
154. Belviso, F. *et al.* Viewpoint: Atomic-scale design protocols toward energy, electronic, catalysis, and sensing applications. *Inorg. Chem.* **58**, 14939–14980, DOI: [10.1021/acs.inorgchem.9b01785](https://doi.org/10.1021/acs.inorgchem.9b01785) (2019). PMID: 31668070, <https://doi.org/10.1021/acs.inorgchem.9b01785>.
155. Seidl, A., Görling, A., Vogl, P., Majewski, J. A. & Levy, M. Generalized Kohn-Sham schemes and the band-gap problem. *Phys. Rev. B* **53**, 3764–3774, DOI: [10.1103/PhysRevB.53.3764](https://doi.org/10.1103/PhysRevB.53.3764) (1996).
156. Marcus, R. A. Chemical and electrochemical electron-transfer theory. *Annu. Rev. Phys. Chem.* **15**, 155–196, DOI: [10.1146/annurev.pc.15.100164.001103](https://doi.org/10.1146/annurev.pc.15.100164.001103) (1964). <https://doi.org/10.1146/annurev.pc.15.100164.001103>.
157. Sun, L., Huang, X., Wang, L. & Janotti, A. Disentangling the role of small polarons and oxygen vacancies in CeO₂. *Phys. Rev. B* **95**, 245101, DOI: [10.1103/PhysRevB.95.245101](https://doi.org/10.1103/PhysRevB.95.245101) (2017).
158. Wang, Z., Brock, C., Matt, A. & Bevan, K. H. Implications of the DFT + *u* method on polaron properties in energy materials. *Phys. Rev. B* **96**, 125150, DOI: [10.1103/PhysRevB.96.125150](https://doi.org/10.1103/PhysRevB.96.125150) (2017).
159. Kick, M., Reuter, K. & Oberhofer, H. Intricacies of DFT+U, Not Only in a Numeric Atom Centered Orbital Framework. *J. Chem. Theory Comput.* **15**, 1705–1718, DOI: [10.1021/acs.jctc.8b01211](https://doi.org/10.1021/acs.jctc.8b01211) (2019).
160. Cococcioni, M. & de Gironcoli, S. Linear response approach to the calculation of the effective interaction parameters in the LDA + U method. *Phys. Rev. B* **71**, 035105, DOI: [10.1103/PhysRevB.71.035105](https://doi.org/10.1103/PhysRevB.71.035105) (2005).
161. Aryasetiawan, F., Karlsson, K., Jepsen, O. & Schönberger, U. Calculations of Hubbard *U* from first-principles. *Phys. Rev. B* **74**, 125106, DOI: [10.1103/PhysRevB.74.125106](https://doi.org/10.1103/PhysRevB.74.125106) (2006).
162. Perdew, J. P. & Zunger, A. Self-interaction correction to density-functional approximations for many-electron systems. *Phys. Rev. B* **23**, 5048–5079, DOI: [10.1103/PhysRevB.23.5048](https://doi.org/10.1103/PhysRevB.23.5048) (1981).
163. Janesko, B. G., Henderson, T. M. & Scuseria, G. E. Screened hybrid density functionals for solid-state chemistry and physics. *Phys. Chem. Chem. Phys.* **11**, 443–454, DOI: [10.1039/B812838C](https://doi.org/10.1039/B812838C) (2009).
164. Pacchioni, G., Frigoli, F., Ricci, D. & Weil, J. A. Theoretical description of hole localization in a quartz al center: The importance of exact electron exchange. *Phys. Rev. B* **63**, 054102, DOI: [10.1103/PhysRevB.63.054102](https://doi.org/10.1103/PhysRevB.63.054102) (2000).
165. Tabriz, M. F., Aradi, B., Frauenheim, T. & Deák, P. Application of the Lany–Zunger polaron correction for calculating surface charge trapping. *J. Physics: Condens. Matter* **29**, 394001, DOI: [10.1088/1361-648x/aa7ebd](https://doi.org/10.1088/1361-648x/aa7ebd) (2017).
166. Elmaslmane, A. R., Wetherell, J., Hodgson, M. J., McKenna, K. P. & Godby, R. W. Accuracy of electron densities obtained via Koopmans-compliant hybrid functionals. *Phys. Rev. Mater.* **2**, 040801, DOI: [10.1103/PhysRevMaterials.2.040801](https://doi.org/10.1103/PhysRevMaterials.2.040801) (2018). [1803.11076](https://doi.org/10.1103/PhysRevMaterials.2.040801).
167. Makov, G. & Payne, M. C. Periodic boundary conditions in ab initio calculations. *Phys. Rev. B* **51**, 4014–4022, DOI: [10.1103/PhysRevB.51.4014](https://doi.org/10.1103/PhysRevB.51.4014) (1995).
168. Schluger, A. L. & Stoneham, A. M. Small polarons in real crystals: concepts and problems. *J. Physics: Condens. Matter* **5**, 3049–3086, DOI: [10.1088/0953-8984/5/19/007](https://doi.org/10.1088/0953-8984/5/19/007) (1993).
169. Pinto, H. & Stashans, A. Computational study of self-trapped hole polarons in tetragonal BaTiO_3 . *Phys. Rev. B* **65**, 134304, DOI: [10.1103/PhysRevB.65.134304](https://doi.org/10.1103/PhysRevB.65.134304) (2002).
170. Eglitis, R., Eglitis, R., Kotomin, E., Kotomin, E. & Borstel, G. Semi-Empirical Calculations of Hole Polarons in MgO and KNbO₃ Crystals. *physica status solidi (b)* **208**, 15–20, DOI: [10.1002/\(SICI\)1521-3951\(199807\)208:1<15::AID-PSSB15>3.0.CO;2-5](https://doi.org/10.1002/(SICI)1521-3951(199807)208:1<15::AID-PSSB15>3.0.CO;2-5) (1998).
171. Neukirch, A. J. *et al.* Polaron Stabilization by Cooperative Lattice Distortion and Cation Rotations in Hybrid Perovskite Materials. *Nano Lett.* **16**, 3809–3816, DOI: [10.1021/acs.nanolett.6b01218](https://doi.org/10.1021/acs.nanolett.6b01218) (2016).

172. Kick, M. & Oberhofer, H. Towards a transferable design of solid-state embedding models on the example of a rutile TiO_2 (110) surface. *The J. Chem. Phys.* **151**, 184114, DOI: [10.1063/1.5125204](https://doi.org/10.1063/1.5125204) (2019).
173. Berger, D., Oberhofer, H. & Reuter, K. First-principles embedded-cluster calculations of the neutral and charged oxygen vacancy at the rutile TiO_2 (110) surface. *Phys. Rev. B* **92**, 075308, DOI: [10.1103/PhysRevB.92.075308](https://doi.org/10.1103/PhysRevB.92.075308) (2015). [1506.00596](https://pubmed.ncbi.nlm.nih.gov/26000596/).
174. Ghosh, D., Welch, E., Neukirch, A. J., Zakhidov, A. & Tretiak, S. Polarons in halide perovskites: A perspective. *The J. Phys. Chem. Lett.* **11**, 3271–3286, DOI: [10.1021/acs.jpclett.0c00018](https://doi.org/10.1021/acs.jpclett.0c00018) (2020). PMID: 32216360, <https://doi.org/10.1021/acs.jpclett.0c00018>.
175. Mishchenko, A. S., Nagaosa, N., De Filippis, G., de Candia, A. & Cataudella, V. Mobility of holstein polaron at finite temperature: An unbiased approach. *Phys. Rev. Lett.* **114**, 146401, DOI: [10.1103/PhysRevLett.114.146401](https://doi.org/10.1103/PhysRevLett.114.146401) (2015).
176. Emin, D. *Polarons* (Cambridge University Press, 2012).
177. Bondarenko, N., Eriksson, O. & Skorodumova, N. V. Polaron mobility in oxygen-deficient and lithium-doped tungsten trioxide. *Phys. Rev. B* **92**, 165119, DOI: [10.1103/PhysRevB.92.165119](https://doi.org/10.1103/PhysRevB.92.165119) (2015).
178. Janotti, A., Franchini, C., Varley, J. B., Kresse, G. & Van de Walle, C. G. Dual behavior of excess electrons in rutile TiO_2 . *physica status solidi (RRL) - Rapid Res. Lett.* **7**, 199–203, DOI: [10.1002/pssr.201206464](https://doi.org/10.1002/pssr.201206464) (2013).
179. Emin, S. I. Small polarons. *Phys. Today* **35**, 34, DOI: [10.1063/1.2938044](https://doi.org/10.1063/1.2938044) (1982).
180. Kadanoff, L. P. Boltzmann equation for polarons. *Phys. Rev.* **130**, 1364–1369, DOI: [10.1103/PhysRev.130.1364](https://doi.org/10.1103/PhysRev.130.1364) (1963).
181. Motta, C. & Sanvito, S. Electron–phonon coupling and polaron mobility in hybrid perovskites from first principles. *The J. Phys. Chem. C* **122**, 1361–1366, DOI: [10.1021/acs.jpcc.7b10163](https://doi.org/10.1021/acs.jpcc.7b10163) (2018). <https://doi.org/10.1021/acs.jpcc.7b10163>.
182. Feynman, R. P., Hellwarth, R. W., Iddings, C. K. & Platzman, P. M. Mobility of slow electrons in a polar crystal. *Phys. Rev.* **127**, 1004–1017, DOI: [10.1103/PhysRev.127.1004](https://doi.org/10.1103/PhysRev.127.1004) (1962).
183. Devreese, J. T. Polarons. *Encycl. Appl. Phys.* **14**, 383–409 (1996).
184. Schirmer, O. *EPR Investigations of Small Electron and Hole Polarons in Oxide Perovskites* (Springer, 2010).
185. Alexandrov, A. S. & Bratkovsky, A. M. Alexandrov and bratkovsky reply:. *Phys. Rev. Lett.* **84**, 2043–2043, DOI: [10.1103/PhysRevLett.84.2043](https://doi.org/10.1103/PhysRevLett.84.2043) (2000).
186. Alexandrov, A. S. & Mott, N. F. *Polarons and Bipolarons* (WORLD SCIENTIFIC, 1996). <https://www.worldscientific.com/doi/pdf/10.1142/2784>.
187. Lanzara, A. *et al.* Evidence for ubiquitous strong electron-phonon coupling in high-temperature superconductors. *Nature* **412**, 510–514, DOI: [10.1038/35087518](https://doi.org/10.1038/35087518) (2001).
188. *Polarons and Bipolarons in High-Tc Superconductors and Related Materials* (Cambridge University Press, 1995).
189. Nishio, T., Ahmad, J. & Uwe, H. Spectroscopic observation of bipolaronic point defects in $\text{Ba}_{1-x}\text{K}_x\text{BiO}_3$. *Phys. Rev. Lett.* **95**, 176403, DOI: [10.1103/PhysRevLett.95.176403](https://doi.org/10.1103/PhysRevLett.95.176403) (2005).
190. Ahmad, J. & Uwe, H. Small-polaron excitations in $\text{Ba}_{1-x}\text{K}_x\text{BiO}_3$ studied by optical reflectivity measurements. *Phys. Rev. B* **72**, 125103, DOI: [10.1103/PhysRevB.72.125103](https://doi.org/10.1103/PhysRevB.72.125103) (2005).
191. de Gennes, P. G. Effects of double exchange in magnetic crystals. *Phys. Rev.* **118**, 141–154, DOI: [10.1103/PhysRev.118.141](https://doi.org/10.1103/PhysRev.118.141) (1960).
192. Mauger, A. Magnetic polaron: Theory and experiment. *Phys. Rev. B* **27**, 2308–2324, DOI: [10.1103/PhysRevB.27.2308](https://doi.org/10.1103/PhysRevB.27.2308) (1983).
193. Lascaray, J., Desfours, J. & Averous, M. Bound magnetic polaron evidence in euo. *Solid State Commun.* **19**, 677 – 679, DOI: [https://doi.org/10.1016/0038-1098\(76\)91103-0](https://doi.org/10.1016/0038-1098(76)91103-0) (1976).
194. Umehara, M. Density-functional approach to doped magnetic semiconductors: Evolution of bound states of electrons as the donor concentration increases. *Phys. Rev. B* **41**, 2421–2433, DOI: [10.1103/PhysRevB.41.2421](https://doi.org/10.1103/PhysRevB.41.2421) (1990).
195. Bondarenko, N. *et al.* Spin polaronics: Static and dynamic properties of spin polarons in La-doped CaMnO_3 . *Phys. Rev. B* **100**, 134443, DOI: [10.1103/PhysRevB.100.134443](https://doi.org/10.1103/PhysRevB.100.134443) (2019).
196. Lenjer, S., Schirmer, O. F., Hesse, H. & Kool, T. W. Conduction states in oxide perovskites: Three manifestations of Ti^{3+} Jahn-Teller polarons in barium titanate. *Phys. Rev. B* **66**, 165106, DOI: [10.1103/PhysRevB.66.165106](https://doi.org/10.1103/PhysRevB.66.165106) (2002).

197. Eglitis, R. I. Ab initio calculations of SrTiO₃, BaTiO₃, PbTiO₃, CaTiO₃, SrZrO₃, PbZrO₃ and BaZrO₃ (001), (011) and (111) surfaces as well as F centers, polarons, KTN solid solutions and Nb impurities therein. *Int. J. Mod. Phys. B* **28**, 1430009, DOI: [10.1142/S0217979214300096](https://doi.org/10.1142/S0217979214300096) (2014). <https://doi.org/10.1142/S0217979214300096>.
198. Höck, K. H., Nickisch, H. & Thomas, H. *Helv. Phys. Act* **56**, 237 (1983).
199. Allen, P. B. & Perebeinos, V. Anti-Jahn-Teller polaron in LaMnO₃. *Phys. Rev. B* **60**, 10747–10753, DOI: [10.1103/PhysRevB.60.10747](https://doi.org/10.1103/PhysRevB.60.10747) (1999).
200. Hao, X., Wang, Z., Schmid, M., Diebold, U. & Franchini, C. Coexistence of trapped and free excess electrons in SrTiO₃. *Phys. Rev. B* **91**, 085204, DOI: [10.1103/PhysRevB.91.085204](https://doi.org/10.1103/PhysRevB.91.085204) (2015).
201. Klyukin, K. & Alexandrov, V. Effect of intrinsic point defects on ferroelectric polarization behavior of SrTiO₃. *Phys. Rev. B* **95**, 035301, DOI: [10.1103/PhysRevB.95.035301](https://doi.org/10.1103/PhysRevB.95.035301) (2017).
202. Xu, T. *et al.* Electron engineering of metallic multiferroic polarons in epitaxial BaTiO₃. *npj Comput. Mater.* **5**, 23, DOI: [10.1038/s41524-019-0163-6](https://doi.org/10.1038/s41524-019-0163-6) (2019).
203. Zheng, G. & Patterson, C. H. Ferromagnetic polarons in La_{0.5}Ca_{0.5}MnO₃ and La_{0.33}Ca_{0.67}MnO₃. *Phys. Rev. B* **67**, 220404, DOI: [10.1103/PhysRevB.67.220404](https://doi.org/10.1103/PhysRevB.67.220404) (2003).
204. Giovannetti, G., Kumar, S., van den Brink, J. & Picozzi, S. Magnetically induced electronic ferroelectricity in half-doped manganites. *Phys. Rev. Lett.* **103**, 037601, DOI: [10.1103/PhysRevLett.103.037601](https://doi.org/10.1103/PhysRevLett.103.037601) (2009).
205. Colizzi, G., Filippetti, A. & Fiorentini, V. Multiferroicity and orbital ordering in Pr_{0.5}Ca_{0.5}MnO₃ from first principles. *Phys. Rev. B* **82**, 140101, DOI: [10.1103/PhysRevB.82.140101](https://doi.org/10.1103/PhysRevB.82.140101) (2010).
206. Bao, E. & L. Xiao, J. Temperature dependence of the properties of the strong-coupling polaron in a slab of polar crystal. *J. Phys. Soc. Jpn.* **72**, 627–633, DOI: [10.1143/JPSJ.72.627](https://doi.org/10.1143/JPSJ.72.627) (2003). <https://doi.org/10.1143/JPSJ.72.627>.
207. Toyozawa, Y. Interband effect of lattice vibrations in the exciton absorption spectra. *J. Phys. Chem. Solids* **25**, 59 – 71, DOI: [https://doi.org/10.1016/0022-3697\(64\)90162-3](https://doi.org/10.1016/0022-3697(64)90162-3) (1964).
208. Nagaev, E. L. Exciton polarons and plasma-exciton waves. *Zh. Eksp. Teor. Fiz* **57**, 469 (1969).
209. Iadonisi, G. & Bassani, F. Polaronic correction to the exciton effective mass. *Il Nuovo Cimento D* **9**, 703–714, DOI: [10.1007/BF02457030](https://doi.org/10.1007/BF02457030) (1987).
210. Hsu, H.-C. & Hsieh, W.-F. Excitonic polaron and phonon assisted photoluminescence of ZnO nanowires. *Solid State Commun.* **131**, 371 – 375, DOI: <https://doi.org/10.1016/j.ssc.2004.05.043> (2004).
211. Williams, R. & Song, K. The self-trapped exciton. *J. Phys. Chem. Solids* **51**, 679 – 716, DOI: [https://doi.org/10.1016/0022-3697\(90\)90144-5](https://doi.org/10.1016/0022-3697(90)90144-5) (1990).
212. Mahrt, R. & Bäessler, H. Light and heavy excitonic polarons in conjugated polymers. *Synth. Met.* **45**, 107 – 117, DOI: [https://doi.org/10.1016/0379-6779\(91\)91850-A](https://doi.org/10.1016/0379-6779(91)91850-A) (1991).
213. Mott, N. F. & Stoneham, A. M. The lifetime of electrons, holes and excitons before self-trapping. *J. Phys. C: Solid State Phys.* **10**, 3391–3398, DOI: [10.1088/0022-3719/10/17/022](https://doi.org/10.1088/0022-3719/10/17/022) (1977).
214. Schein, L. & Borsenberger, P. Hole mobilities in a hydrazone-doped polycarbonate and poly(styrene). *Chem. Phys.* **177**, 773 – 781, DOI: [https://doi.org/10.1016/0301-0104\(93\)85040-F](https://doi.org/10.1016/0301-0104(93)85040-F) (1993).
215. Gartstein, Y. Charges on semiconducting nanotubes in polar media: Polarons and excitons. *Phys. Lett. A* **349**, 377 – 383, DOI: <https://doi.org/10.1016/j.physleta.2005.08.100> (2006).
216. Basko, D. M. & Conwell, E. M. Effect of solvation on hole motion in dna. *Phys. Rev. Lett.* **88**, 098102, DOI: [10.1103/PhysRevLett.88.098102](https://doi.org/10.1103/PhysRevLett.88.098102) (2002).
217. Wiktor, J. & Pasquarello, A. Electron and hole polarons at the BiVO₄–water interface. *ACS Appl. Mater. & Interfaces* **11**, 18423–18426, DOI: [10.1021/acsami.9b03566](https://doi.org/10.1021/acsami.9b03566) (2019). <https://doi.org/10.1021/acsami.9b03566>.
218. Salje, E. K. H. Polarons and bipolarons in tungsten oxide WO_{3-x}. *Eur. J. Solid State Inorg. Chem.* **31**, 805–821 (1994).
219. Li, S., Luo, J., Liu, J. & Tang, J. Self-trapped excitons in all-inorganic halide perovskites: Fundamentals, status, and potential applications. *The J. Phys. Chem. Lett.* **10**, 1999–2007, DOI: [10.1021/acs.jpclett.8b03604](https://doi.org/10.1021/acs.jpclett.8b03604) (2019). <https://doi.org/10.1021/acs.jpclett.8b03604>.
220. Srimath Kandada, A. R. & Silva, C. Exciton polarons in two-dimensional hybrid metal-halide perovskites. *The J. Phys. Chem. Lett.* **11**, 3173–3184, DOI: [10.1021/acs.jpclett.9b02342](https://doi.org/10.1021/acs.jpclett.9b02342) (2020). PMID: 32191488, <https://doi.org/10.1021/acs.jpclett.9b02342>.

221. Zhu, X. *et al.* Charge transfer excitons at van der waals interfaces. *J. Am. Chem. Soc.* **137**, 8313–8320, DOI: [10.1021/jacs.5b03141](https://doi.org/10.1021/jacs.5b03141) (2015). PMID: 26001297, <https://doi.org/10.1021/jacs.5b03141>.
222. Sangalli, D., Perfetto, E., Stefanucci, G. & Marini, A. An ab-initio approach to describe coherent and non-coherent exciton dynamics. *The Eur. Phys. J. B* **91**, 171, DOI: [10.1140/epjb/e2018-90126-5](https://doi.org/10.1140/epjb/e2018-90126-5) (2018).
223. Soriano, D. & Katsnelson, M. I. Magnetic polaron and antiferromagnetic-ferromagnetic transition in doped bilayer CrI₃. *Phys. Rev. B* **101**, 041402, DOI: [10.1103/PhysRevB.101.041402](https://doi.org/10.1103/PhysRevB.101.041402) (2020).
224. Kweon, K. E., Hwang, G. S., Kim, J., Kim, S. & Kim, S. Electron small polarons and their transport in bismuth vanadate: a first principles study. *Phys. Chem. Chem. Phys.* **17**, 256–260, DOI: [10.1039/C4CP03666B](https://doi.org/10.1039/C4CP03666B) (2015).
225. Ambrosio, F. & Wiktor, J. Strong hole trapping due to oxygen dimers in BiVO₄: Effect on the water oxidation reaction. *The J. Phys. Chem. Lett.* **10**, 7113–7118, DOI: [10.1021/acs.jpclett.9b02701](https://doi.org/10.1021/acs.jpclett.9b02701) (2019). PMID: 31657932, <https://doi.org/10.1021/acs.jpclett.9b02701>.
226. Han, Z.-K., Zhang, L., Liu, M., Ganduglia-Pirovano, M. V. & Gao, Y. The structure of oxygen vacancies in the near-surface of reduced CeO₂ (111) under strain. *Front. Chem.* **7**, 436, DOI: [10.3389/fchem.2019.00436](https://doi.org/10.3389/fchem.2019.00436) (2019).
227. Swift, M., Janotti, A. & Van de Walle, C. G. Small polarons and point defects in barium cerate. *Phys. Rev. B* **92**, 214114, DOI: [10.1103/PhysRevB.92.214114](https://doi.org/10.1103/PhysRevB.92.214114) (2015).
228. Bjaalie, L., Janotti, A., Krishnaswamy, K. & Van de Walle, C. G. Point defects, impurities, and small hole polarons in GdTiO₃. *Phys. Rev. B* **93**, 115316, DOI: [10.1103/PhysRevB.93.115316](https://doi.org/10.1103/PhysRevB.93.115316) (2016).
229. Chen, C., Avila, J., Frantzeskakis, E., Levy, A. & Asensio, M. C. Observation of a two-dimensional liquid of Fröhlich polarons at the bare SrTiO₃ surface. *Nat. Commun.* **6**, 8585, DOI: [10.1038/ncomms9585](https://doi.org/10.1038/ncomms9585) (2015).
230. Hauser, A. J., Mikheev, E., Kajdos, A. P. & Janotti, A. Small polaron-related recombination in Ba_xSr_{1-x}TiO₃ thin films by cathodoluminescence spectroscopy. *Appl. Phys. Lett.* **108**, 102901, DOI: [10.1063/1.4943191](https://doi.org/10.1063/1.4943191) (2016). <https://doi.org/10.1063/1.4943191>.
231. Himmetoglu, B., Janotti, A., Bjaalie, L. & Van de Walle, C. G. Interband and polaronic excitations in YTiO₃ from first principles. *Phys. Rev. B* **90**, 161102, DOI: [10.1103/PhysRevB.90.161102](https://doi.org/10.1103/PhysRevB.90.161102) (2014).
232. Himmetoglu, B. & Janotti, A. Transport properties of KTaO₃ from first-principles. *J. Physics: Condens. Matter* **28**, 065502, DOI: [10.1088/0953-8984/28/6/065502](https://doi.org/10.1088/0953-8984/28/6/065502) (2016).
233. Krishnaswamy, K., Himmetoglu, B., Kang, Y., Janotti, A. & Van de Walle, C. G. First-principles analysis of electron transport in BaSnO₃. *Phys. Rev. B* **95**, 205202, DOI: [10.1103/PhysRevB.95.205202](https://doi.org/10.1103/PhysRevB.95.205202) (2017).
234. Körbel, S., Hlinka, J. & Sanvito, S. Electron trapping by neutral pristine ferroelectric domain walls in BiFeO₃. *Phys. Rev. B* **98**, 100104, DOI: [10.1103/PhysRevB.98.100104](https://doi.org/10.1103/PhysRevB.98.100104) (2018).
235. Ahart, C. S., Blumberger, J. & Rosso, K. M. Polaronic structure of excess electrons and holes for a series of bulk iron oxides. *Phys. Chem. Chem. Phys.* –, DOI: [10.1039/C9CP06482F](https://doi.org/10.1039/C9CP06482F) (2020).
236. Zhou, Z., Long, R. & Prezhd, O. V. Why silicon doping accelerates electron polaron diffusion in hematite. *J. Am. Chem. Soc.* **141**, 20222–20233, DOI: [10.1021/jacs.9b10109](https://doi.org/10.1021/jacs.9b10109) (2019). PMID: 31791126, <https://doi.org/10.1021/jacs.9b10109>.
237. Smart, T. J., Pham, T. A., Ping, Y. & Ogitsu, T. Optical absorption induced by small polaron formation in transition metal oxides: The case of Co₃O₄. *Phys. Rev. Mater.* **3**, 102401, DOI: [10.1103/PhysRevMaterials.3.102401](https://doi.org/10.1103/PhysRevMaterials.3.102401) (2019).
238. Wu, F. & Ping, Y. Combining Landau–Zener theory and kinetic monte carlo sampling for small polaron mobility of doped BiVO₄ from first-principles. *J. Mater. Chem. A* **6**, 20025–20036, DOI: [10.1039/C8TA07437B](https://doi.org/10.1039/C8TA07437B) (2018).
239. Ho, Q. D., Frauenheim, T. & Deak, P. Theoretical confirmation of the polaron model for the Mg acceptor in β -Ga₂O₃. *J. Appl. Phys.* **124**, 145702, DOI: [10.1063/1.5049861](https://doi.org/10.1063/1.5049861) (2018). <https://doi.org/10.1063/1.5049861>.
240. Deák, P. *et al.* Defect calculations with hybrid functionals in layered compounds and in slab models. *Phys. Rev. B* **100**, 235304, DOI: [10.1103/PhysRevB.100.235304](https://doi.org/10.1103/PhysRevB.100.235304) (2019).
241. Zhang, S. X. *et al.* Niobium doped TiO₂: Intrinsic transparent metallic anatase versus highly resistive rutile phase. *J. Appl. Phys.* **102**, 013701, DOI: [10.1063/1.2750407](https://doi.org/10.1063/1.2750407) (2007).
242. Urushibara, A. *et al.* Insulator-metal transition and giant magnetoresistance in La_{1-x}Sr_xMnO₃. *Phys. Rev. B* **51**, 14103–14109, DOI: [10.1103/PhysRevB.51.14103](https://doi.org/10.1103/PhysRevB.51.14103) (1995).
243. Krüger, P. *et al.* Defect States at the TiO₂(110) Surface Probed by Resonant Photoelectron Diffraction. *Phys. Rev. Lett.* **100**, 055501, DOI: [10.1103/PhysRevLett.100.055501](https://doi.org/10.1103/PhysRevLett.100.055501) (2008).

244. Yim, C. M. *et al.* Engineering polarons at a metal oxide surface. *Phys. Rev. Lett.* **117**, 116402, DOI: [10.1103/PhysRevLett.117.116402](https://doi.org/10.1103/PhysRevLett.117.116402) (2016).
245. Furubayashi, Y. *et al.* A transparent metal: Nb-doped anatase TiO₂. *Appl. Phys. Lett.* **86**, 252101 (2005).
246. Gratzel, M. Dye-sensitized solar cells. *J. Photochem. Photobiol. C: Photochem. Rev.* **4**, 143–153 (2003).
247. Tuller, H. & Nowick, A. Small polaron electron transport in reduced CeO₂ single crystals. *J. Phys. Chem. Solids* **38**, 859–867, DOI: [10.1016/0022-3697\(77\)90124-X](https://doi.org/10.1016/0022-3697(77)90124-X) (1977).
248. Kang, S. D., Dylla, M. & Snyder, G. J. Thermopower-conductivity relation for distinguishing transport mechanisms: Polaron hopping in CeO₂ and band conduction in SrTiO₃. *Phys. Rev. B* **97**, 235201, DOI: [10.1103/PhysRevB.97.235201](https://doi.org/10.1103/PhysRevB.97.235201) (2018).
249. Mechelen, J. L. M. *et al.* Electron-phonon interaction and charge carrier mass enhancement in SrTiO₃. *Phys. Rev. Lett.* **100**, 226403 (2008).
250. Yoon, S. *et al.* Raman and optical spectroscopic studies of small-to-large polaron crossover in the perovskite manganese oxides. *Phys. Rev. B* **58**, 2795–2801 (1998).
251. Scott, J., Damen, T., Silfvast, W., Leite, R. & Cheesman, L. Resonant raman scattering in zns and znse with the cadmium laser. *Opt. Commun.* **1**, 397 – 399, DOI: [https://doi.org/10.1016/0030-4018\(70\)90081-7](https://doi.org/10.1016/0030-4018(70)90081-7) (1970).
252. Kuroda, N. & Nishina, Y. Resonance raman scattering study on exciton and polaron anisotropies in inse. *Sol. State. Comm.* **34**, 481–484 (1980).
253. Ament, L. J. P., van Veenendaal, M. & van den Brink, J. Determining the electron-phonon coupling strength from resonant inelastic X-ray scattering at transition metal L-edges. *EPL (Europhysics Lett.)* **95**, 27008, DOI: [10.1209/0295-5075/95/27008](https://doi.org/10.1209/0295-5075/95/27008) (2011).
254. Rossi, M. *et al.* Experimental determination of momentum-resolved electron-phonon coupling. *Phys. Rev. Lett.* **123**, 027001, DOI: [10.1103/PhysRevLett.123.027001](https://doi.org/10.1103/PhysRevLett.123.027001) (2019).
255. Kispert, L. D., Joseph, J., Miller, G. G. & Baughman, R. H. Epr study of polarons in a conducting polymer with nondegenerate ground states: Alkali metal complexes of poly (p-phenylene) and phenylene oligomers. *The J. Chem. Phys.* **81**, 2119–2125, DOI: [10.1063/1.447836](https://doi.org/10.1063/1.447836) (1984). <https://doi.org/10.1063/1.447836>.
256. Sang, L., Zhao, Y. & Burda, C. TiO₂ nanoparticles as functional building blocks. *Chem. Rev.* **114**, 9283–9318 (1985).
257. Burroughes, J. H. *et al.* Light-emitting diodes based on conjugated polymers. *Nature* **347**, 539–541 (1990).
258. Furukawa, Y., Sakamoto, A., Ohta, H. & Tasumi, M. Raman characterization of polarons, bipolarons and solitons in conducting polymers. *Synth. Met.* **49**, 335–340 (1992).
259. Grenier, P., Bernier, G., Jandl, S., Salce, B. & Boatner, L. A. Fluorescence and ferroelectric microregions in KTaO₃. *J. Phys. Cond. Matt.* **1**, 2515–2520 (1989).
260. Strocov, V. N., Cancellieri, C. & Mishchenko, A. S. *Electrons and Polarons at Oxide Interfaces Explored by Soft-X-Ray ARPES* (Springer, 2018).
261. Vura-Weis, J. *et al.* Femtosecond M2,3-edge spectroscopy of transition-metal oxides: Photoinduced oxidation state change in α -Fe₂O₃. *The J. Phys. Chem. Lett.* **4**, 3667–3671, DOI: [10.1021/jz401997d](https://doi.org/10.1021/jz401997d) (2013).
262. Citrin, P. H., Eisenberger, P. & Hamann, D. R. Phonon broadening of X-ray photoemission linewidths. *Phys. Rev. Lett.* **33**, 965–969, DOI: [10.1103/PhysRevLett.33.965](https://doi.org/10.1103/PhysRevLett.33.965) (1974).
263. Katz, J. E. *et al.* Electron small polarons and their mobility in iron (oxyhydr)oxide nanoparticles. *Science* **337**, 1200–1203, DOI: [10.1126/science.1223598](https://doi.org/10.1126/science.1223598) (2012). <https://science.sciencemag.org/content/337/6099/1200.full.pdf>.
264. Obara, Y. *et al.* Femtosecond time-resolved x-ray absorption spectroscopy of anatase tio2 nanoparticles using xfel. *Struct. Dyn.* **4**, 044033, DOI: [10.1063/1.4989862](https://doi.org/10.1063/1.4989862) (2017). <https://doi.org/10.1063/1.4989862>.
265. Grübel, G., Stephenson, G., Gutt, C., Sinn, H. & Tschentscher, T. Xpcs at the european x-ray free electron laser facility. *Nucl. Instruments Methods Phys. Res. Sect. B: Beam Interactions with Mater. Atoms* **262**, 357 – 367, DOI: <https://doi.org/10.1016/j.nimb.2007.05.015> (2007).
266. Di Valentin, C. *et al.* Density functional theory and electron paramagnetic resonance study on the effect of N-F codoping of TiO₂. *Chem. Mater.* **20**, 3706–3714, DOI: [10.1021/cm703636s](https://doi.org/10.1021/cm703636s) (2008).
267. Possenriede, E., Kröse, H., Varnhorst, T., Scharfschwerdt, R. & Schirmer, O. F. Shallow acceptor and electron conduction states in BaTiO₃. *Ferroelectrics* **151**, 199–204, DOI: [10.1080/00150199408244743](https://doi.org/10.1080/00150199408244743) (1994).

268. Chiesa, M., Paganini, M. C., Livraghi, S. & Giamello, E. Charge trapping in TiO₂ polymorphs as seen by electron paramagnetic resonance spectroscopy. *Phys. Chem. Chem. Phys.* **15**, 9435–9447, DOI: [10.1039/C3CP50658D](https://doi.org/10.1039/C3CP50658D) (2013).
269. Shengelaya, A., Zhao, G.-m., Keller, H. & Müller, K. A. EPR evidence of Jahn-Teller polaron formation in La_{1-x}Ca_xMnO_{3+y}. *Phys. Rev. Lett.* **77**, 5296–5299, DOI: [10.1103/PhysRevLett.77.5296](https://doi.org/10.1103/PhysRevLett.77.5296) (1996).
270. Allodi, G., Cestelli Guidi, M., De Renzi, R., Caneiro, A. & Pinsard, L. Ultraslow Polaron Dynamics in Low-Doped Manganites from ¹³⁹La NMR-NQR and Muon Spin Rotation. *Phys Rev Lett* **87**, 127206, DOI: [10.1103/PhysRevLett.87.127206](https://doi.org/10.1103/PhysRevLett.87.127206) (2001).
271. Wu, L., Klie, R. F., Zhu, Y. & Jooss, C. Experimental confirmation of Zener-polaron-type charge and orbital ordering in Pr_{1-x}Ca_xMnO₃. *Phys. Rev. B* **76**, 174210, DOI: [10.1103/PhysRevB.76.174210](https://doi.org/10.1103/PhysRevB.76.174210) (2007).
272. Esch, F. *et al.* Electron localization determines defect formation on ceria substrates. *Science* **309**, 752–755 (2005).
273. Minato, T. *et al.* The electronic structure of oxygen atom vacancy and hydroxyl impurity defects on titanium dioxide (110) surface. *J. Chem. Phys.* **130**, 124502 (2009).
274. Giessibl, F. J. The qplus sensor, a powerful core for the atomic force microscope. *Rev. Sci. Instr.* **90**, 011101 (2019).
275. Setvin, M. *et al.* Polarity compensation mechanisms on the perovskite surface KTaO₃(001). *Science* **359**, 572–575 (2018).
276. Gross, L., Mohn, F., Liljeroth, P., Giessibl, F. J. & Meyer, G. Measuring the charge state of an adatom with noncontact atomic force microscopy. *Science* **324**, 1428–1431 (2009).
277. Patera, L., Queck, F., Scheuerer, P. & Repp, J. Mapping orbital changes upon electron transfer with tunnelling microscopy on insulators. *Nature* **566**, 245–248 (2019).
278. Wagner, C. *et al.* Quantitative imaging of electric surface potentials with single-atom sensitivity. *Nat. Mater.* **18**, 853–859 (2019).
279. Frederikse, H. P. R., Thurber, W. R. & Hosler, W. R. Electronic transport in strontium titanate. *Phys. Rev.* **134**, A442–A445, DOI: [10.1103/PhysRev.134.A442](https://doi.org/10.1103/PhysRev.134.A442) (1964).
280. Friend, R. H., Bradley, D. D. C. & Townsend, P. D. Photo-excitation in conjugated polymers. *J. Phys. D* **20**, 1367–1384 (1987).
281. Freytag, F., Corradi, G. & Imlau, M. Atomic insight to lattice distortions caused by carrier self-trapping in oxide materials. *Sci. Reports* **6**, 36929, DOI: [10.1038/srep36929](https://doi.org/10.1038/srep36929) (2016).
282. Dohnálek, Z., Lyubintsky, I. & Rousseau, R. Thermally-driven processes on rutile TiO₂(110)-(1×1): A direct view at the atomic scale. *Prog. Surf. Sci.* **85**, 161–205, DOI: [10.1016/j.progsurf.2010.03.001](https://doi.org/10.1016/j.progsurf.2010.03.001) (2010).
283. Liu, B. *et al.* Intrinsic intermediate gap states of TiO₂ materials and their roles in charge carrier kinetics. *J. Photochem. Photobiol. C: Photochem. Rev.* **39**, 1–57, DOI: [10.1016/j.jphotochemrev.2019.02.001](https://doi.org/10.1016/j.jphotochemrev.2019.02.001) (2019).
284. Yan, B. *et al.* Anatase TiO₂—A model system for large polaron transport. *ACS Appl. Mater. & Interfaces* **10**, 38201–38208, DOI: [10.1021/acsami.8b11643](https://doi.org/10.1021/acsami.8b11643) (2018). <https://doi.org/10.1021/acsami.8b11643>.
285. Garcia, J. C., Nolan, M., Aaron Deskins, N. & Deskins, N. A. The nature of interfaces and charge trapping sites in photocatalytic mixed-phase TiO₂ from first principles modeling. *J. Chem. Phys.* **142**, 024708, DOI: [10.1063/1.4905122](https://doi.org/10.1063/1.4905122) (2015).
286. Kullgren, J., Huy, H. A., Aradi, B., Frauenheim, T. & Deak, P. Theoretical study of charge separation at the rutile–anatase interface. *physica status solidi (RRL) - Rapid Res. Lett.* **8**, 566–570, DOI: [10.1002/pssr.201409048](https://doi.org/10.1002/pssr.201409048) (2014). <https://onlinelibrary.wiley.com/doi/pdf/10.1002/pssr.201409048>.
287. Carey, J. J. & McKenna, K. P. Screening Doping Strategies To Mitigate Electron Trapping at Anatase TiO₂ Surfaces. *The J. Phys. Chem. C* **123**, 22358–22367, DOI: [10.1021/acs.jpcc.9b05840](https://doi.org/10.1021/acs.jpcc.9b05840) (2019).
288. Wang, Y. *et al.* Role of point defects on the reactivity of reconstructed anatase titanium dioxide (001) surface. *Nat. Commun.* **4**, 2214, DOI: [10.1038/ncomms3214](https://doi.org/10.1038/ncomms3214) (2013).
289. Zhang, Q. *et al.* Measurement and Manipulation of the Charge State of an Adsorbed Oxygen Adatom on the Rutile TiO₂(110)-1×1 Surface by nc-AFM and KPFM. *J. Am. Chem. Soc.* **140**, 15668–15674, DOI: [10.1021/jacs.8b07745](https://doi.org/10.1021/jacs.8b07745) (2018).
290. Cao, Y. *et al.* Scenarios of polaron-involved molecular adsorption on reduced TiO₂(110) surfaces. *Sci. Reports* **7**, 6148, DOI: [10.1038/s41598-017-06557-6](https://doi.org/10.1038/s41598-017-06557-6) (2017).

291. Cao, Y. *et al.* Nitric Oxide Reaction Pathways on Rutile TiO₂ (110): The Influence of Surface Defects and Reconstructions. *The J. Phys. Chem. C* **122**, 23441–23450, DOI: [10.1021/acs.jpcc.8b06135](https://doi.org/10.1021/acs.jpcc.8b06135) (2018).
292. Xu, M. *et al.* The Surface Science Approach for Understanding Reactions on Oxide Powders: The Importance of IR Spectroscopy. *Angewandte Chemie Int. Ed.* **51**, 4731–4734, DOI: [10.1002/anie.201200585](https://doi.org/10.1002/anie.201200585) (2012).
293. Kunat, M. *et al.* Formation of weakly bound, ordered adlayers of CO on rutile TiO₂(110): A combined experimental and theoretical study. *The J. Chem. Phys.* **130**, 144703, DOI: [10.1063/1.3098318](https://doi.org/10.1063/1.3098318) (2009).
294. Zhao, Y. *et al.* What are the adsorption sites for CO on the reduced TiO₂(110)-1×1 surface? *J. Am. Chem. Soc.* **131**, 7958–7959, DOI: [10.1021/ja902259k](https://doi.org/10.1021/ja902259k) (2009).
295. Yoon, Y. *et al.* Anticorrelation between surface and subsurface point defects and the impact on the redox chemistry of TiO₂(110). *ChemPhysChem* **16**, 313–321, DOI: [10.1002/cphc.201402599](https://doi.org/10.1002/cphc.201402599) (2015).
296. Yu, Y. Y. & Gong, X. Q. CO Oxidation at Rutile TiO₂(110): Role of Oxygen Vacancies and Titanium Interstitials. *ACS Catal.* **5**, 2042–2050, DOI: [10.1021/cs501900q](https://doi.org/10.1021/cs501900q) (2015).
297. Mu, R. *et al.* Adsorption and Photodesorption of CO from Charged Point Defects on TiO₂(110). *J. Phys. Chem. Lett.* **8**, 4565–4572, DOI: [10.1021/acs.jpcllett.7b02052](https://doi.org/10.1021/acs.jpcllett.7b02052) (2017).
298. Chen, J., Penschke, C., Alavi, A. & Michaelides, A. Small polarons and the Janus nature of TiO₂(110). *Phys. Rev. B* **101**, 115402, DOI: [10.1103/PhysRevB.101.115402](https://doi.org/10.1103/PhysRevB.101.115402) (2020).
299. López-Caballero, P. *et al.* Exploring the properties of Ag_s–TiO₂ interfaces: stable surface polaron formation, UV-Vis optical response, and CO₂ photoactivation. *J. Mater. Chem. A* **8**, 6842–6853, DOI: [10.1039/D0TA00062K](https://doi.org/10.1039/D0TA00062K) (2020).
300. Selli, D., Fazio, G. & Di Valentin, C. Using Density Functional Theory to Model Realistic TiO₂ Nanoparticles, Their Photoactivation and Interaction with Water. *Catalysts* **7**, 357, DOI: [10.3390/catal7120357](https://doi.org/10.3390/catal7120357) (2017).
301. Shirai, K. *et al.* Water-Assisted Hole Trapping at the Highly Curved Surface of Nano-TiO₂ Photocatalyst. *J. Am. Chem. Soc.* **140**, 1415–1422, DOI: [10.1021/jacs.7b11061](https://doi.org/10.1021/jacs.7b11061) (2018).
302. Gerritson, H. J. . In *Proceedings of the First International Conference on Paramagnetic Resonance*, Vol. 1 (Academic Press Inc., New York, 1962).
303. Bogomolov, V. N., Kudinov, E. K., Mirlin, D. N. & Firsov, Y. A. Polaron mechanism of light absorption in rutile crystals TiO₂. *Fiz. tverd. Tela* **9**, 2077 (1967).
304. Bogomolov, V. N. & Mirlin, D. N. Optical Absorption by Polarons in Rutile (TiO₂) Single Crystals. *Phys. Status Solidi (B)* **27**, 443–453, DOI: [10.1002/pssb.19680270144](https://doi.org/10.1002/pssb.19680270144) (1968).
305. Dominik, L. A. K. & MacCrone, R. K. Dielectric Relaxation of Hopping Electrons in Reduced Rutile, TiO₂. *Phys. Rev.* **156**, 910–913, DOI: [10.1103/PhysRev.156.910](https://doi.org/10.1103/PhysRev.156.910) (1967).
306. Yagi, E., Hasiguti, R. R. & Aono, M. Electronic conduction above 4 K of slightly reduced oxygen-deficient rutile TiO_{2-x}. *Phys. Rev. B* **54**, 7945–7956, DOI: [10.1103/PhysRevB.54.7945](https://doi.org/10.1103/PhysRevB.54.7945) (1996).
307. Nowotny, J., Radecka, M. & Rekas, M. Semiconducting properties of undoped TiO₂. *J. Phys. Chem. Solids* **58**, 927–937, DOI: [10.1016/S0022-3697\(96\)00204-1](https://doi.org/10.1016/S0022-3697(96)00204-1) (1997).
308. Finazzi, E., Valentin, C. D. & Pacchioni, G. Nature of Ti interstitials in reduced bulk anatase and rutile TiO₂. *J. Phys. Chem. C* **113**, 3382–3385, DOI: [10.1021/jp8111793](https://doi.org/10.1021/jp8111793) (2009).
309. Pham, T. D. & Deskins, N. A. Efficient Method for Modeling Polarons Using Electronic Structure Methods. *J. Chem. Theory Comput.* **16**, 5264–5278, DOI: [10.1021/acs.jctc.0c00374](https://doi.org/10.1021/acs.jctc.0c00374) (2020).
310. Deskins, N. A., Rousseau, R. & Dupuis, M. Localized electronic states from surface hydroxyls and polarons in TiO₂(110). *J. Phys. Chem. C* **113**, 14583–14586, DOI: [10.1021/jp9037655](https://doi.org/10.1021/jp9037655) (2009).
311. Krüger, P. *et al.* Intrinsic nature of the excess electron distribution at the TiO₂(110) surface. *Phys. Rev. Lett.* **108**, 126803, DOI: [10.1103/PhysRevLett.108.126803](https://doi.org/10.1103/PhysRevLett.108.126803) (2012).
312. Morita, K., Shibuya, T. & Yasuoka, K. Stability of excess electrons introduced by Ti interstitial in rutile TiO₂(110) surface. *J. Phys. Chem. C* **121**, 1602–1607, DOI: [10.1021/acs.jpcc.6b09669](https://doi.org/10.1021/acs.jpcc.6b09669) (2017).
313. Moses, P. G., Janotti, A., Franchini, C., Kresse, G. & Van De Walle, C. G. Donor defects and small polarons on the TiO₂(110) surface. *J. Appl. Phys.* **119**, 181503, DOI: [10.1063/1.4948239](https://doi.org/10.1063/1.4948239) (2016).
314. Deák, P., Aradi, B. & Frauenheim, T. Oxygen deficiency in TiO₂: Similarities and differences between the Ti self-interstitial and the O vacancy in bulk rutile and anatase. *Phys. Rev. B* **92**, 045204, DOI: [10.1103/PhysRevB.92.045204](https://doi.org/10.1103/PhysRevB.92.045204) (2015).

315. Nelson, J., Haque, S. A., Klug, D. R. & Durrant, J. R. Trap-limited recombination in dye-sensitized nanocrystalline metal oxide electrodes. *Phys. Rev. B* **63**, 205321, DOI: [10.1103/PhysRevB.63.205321](https://doi.org/10.1103/PhysRevB.63.205321) (2001).
316. Nelson, J. & Chandler, R. E. Random walk models of charge transfer and transport in dye sensitized systems. *Coord. Chem. Rev.* **248**, 1181–1194, DOI: [10.1016/j.ccr.2004.04.001](https://doi.org/10.1016/j.ccr.2004.04.001) (2004).
317. Barzykin, A. V. & Tachiya, M. Mechanism of charge recombination in dye-sensitized nanocrystalline semiconductors: Random flight model. *J. Phys. Chem. B* **106**, 4356–4363, DOI: [10.1021/jp012957+](https://doi.org/10.1021/jp012957+) (2002).
318. Carey, J. J. & McKenna, K. P. Does polaronic self-trapping occur at anatase TiO₂ surfaces. *The J. Phys. Chem. C* **122**, 27540–27553, DOI: [10.1021/acs.jpcc.8b09437](https://doi.org/10.1021/acs.jpcc.8b09437) (2018). <https://doi.org/10.1021/acs.jpcc.8b09437>.
319. Deak, P., Kullgren, J. & Frauenheim, T. Polarons and oxygen vacancies at the surface of anatase TiO₂. *Phys. Status Solidi (RRL) - Rapid Res. Lett.* **8**, 583–586, DOI: [10.1002/pssr.201409139](https://doi.org/10.1002/pssr.201409139) (2014). <https://onlinelibrary.wiley.com/doi/pdf/10.1002/pssr.201409139>.
320. Di Liberto, G., Tosoni, S. & Pacchioni, G. Nitrogen doping in coexposed (001)–(101) anatase TiO₂ surfaces: A DFT study. *Phys. Chem. Chem. Phys.* **21**, 21497–21505, DOI: [10.1039/C9CP03930A](https://doi.org/10.1039/C9CP03930A) (2019).
321. Chiesa, M., Livraghi, S., Giamello, E., Albanese, E. & Pacchioni, G. Ferromagnetic Interactions in Highly Stable, Partially Reduced TiO₂: The S=2 State in Anatase. *Angewandte Chemie - Int. Ed.* **56**, 2604–2607, DOI: [10.1002/anie.201610973](https://doi.org/10.1002/anie.201610973) (2017).
322. Henrich, V. E., Dresselhaus, G. & Zeiger, H. J. Observation of two-dimensional phases associated with defect states on the surface of TiO₂. *Phys. Rev. Lett.* **36**, 1335–1339, DOI: [10.1103/PhysRevLett.36.1335](https://doi.org/10.1103/PhysRevLett.36.1335) (1976).
323. Gionco, C. *et al.* Al- and Ga-Doped TiO₂, ZrO₂, and HfO₂: The Nature of O 2p Trapped Holes from a Combined Electron Paramagnetic Resonance (EPR) and Density Functional Theory (DFT) Study. *Chem. Mater.* **27**, 3936–3945, DOI: [10.1021/acs.chemmater.5b00800](https://doi.org/10.1021/acs.chemmater.5b00800) (2015).
324. Livraghi, S., Maurelli, S., Paganini, M. C., Chiesa, M. & Giamello, E. Probing the Local Environment of Ti³⁺ Ions in TiO₂ (Rutile) by ¹⁷O. *Angewandte Chemie Int. Ed.* **50**, 8038–8040, DOI: [10.1002/anie.201100531](https://doi.org/10.1002/anie.201100531) (2011).
325. Forro, L. *et al.* High mobility n-type charge carriers in large single crystals of anatase (tio2). *J. Appl. Phys.* **75**, 633–635, DOI: [10.1063/1.355801](https://doi.org/10.1063/1.355801) (1994). <https://doi.org/10.1063/1.355801>.
326. Dou, M. & Persson, C. Comparative study of rutile and anatase SnO₂ and TiO₂ : Band-edge structures, dielectric functions, and polaron effects. *J. Appl. Phys.* **113**, 083703, DOI: [10.1063/1.4793273](https://doi.org/10.1063/1.4793273) (2013).
327. Moser, S. *et al.* Electron-Phonon Coupling in the Bulk of Anatase TiO₂ Measured by Resonant Inelastic X-Ray Spectroscopy. *Phys. Rev. Lett.* **115**, 096404, DOI: [10.1103/PhysRevLett.115.096404](https://doi.org/10.1103/PhysRevLett.115.096404) (2015).
328. Jena, A. K., Kulkarni, A. & Miyasaka, T. Halide perovskite photovoltaics: Background, status, and future prospects. *Chem. Rev.* **119**, 3036–3103, DOI: [10.1021/acs.chemrev.8b00539](https://doi.org/10.1021/acs.chemrev.8b00539) (2019). <https://doi.org/10.1021/acs.chemrev.8b00539>.
329. Welch, E., Scolfaro, L. & Zakhidov, A. Density functional theory + u modeling of polarons in organohalide lead perovskites. *AIP Adv.* **6**, 125037, DOI: [10.1063/1.4972341](https://doi.org/10.1063/1.4972341) (2016). <https://doi.org/10.1063/1.4972341>.
330. Diab, H. *et al.* Narrow linewidth excitonic emission in organic–inorganic lead iodide perovskite single crystals. *The J. Phys. Chem. Lett.* **7**, 5093–5100, DOI: [10.1021/acs.jpclett.6b02261](https://doi.org/10.1021/acs.jpclett.6b02261) (2016). PMID: 27973876, <https://doi.org/10.1021/acs.jpclett.6b02261>.
331. Bokdam, M. *et al.* Role of polar phonons in the photo excited state of metal halide perovskites. *Sci. Reports* **6**, 28618, DOI: [10.1038/srep28618](https://doi.org/10.1038/srep28618) (2016).
332. Zhu, X.-Y. & Podzorov, V. Charge carriers in hybrid organic–inorganic lead halide perovskites might be protected as large polarons. *The J. Phys. Chem. Lett.* **6**, 4758–4761, DOI: [10.1021/acs.jpclett.5b02462](https://doi.org/10.1021/acs.jpclett.5b02462) (2015).
333. Emin, D. Barrier to recombination of oppositely charged large polarons. *J. Appl. Phys.* **123**, 055105, DOI: [10.1063/1.5019834](https://doi.org/10.1063/1.5019834) (2018). <https://doi.org/10.1063/1.5019834>.
334. Mahata, A., Meggiolaro, D. & De Angelis, F. From large to small polarons in lead, tin, and mixed lead–tin halide perovskites. *The J. Phys. Chem. Lett.* **10**, 1790–1798, DOI: [10.1021/acs.jpclett.9b00422](https://doi.org/10.1021/acs.jpclett.9b00422) (2019). <https://doi.org/10.1021/acs.jpclett.9b00422>.
335. Zhou, L. *et al.* Cation alloying delocalizes polarons in lead halide perovskites. *The J. Phys. Chem. Lett.* **10**, 3516–3524, DOI: [10.1021/acs.jpclett.9b01077](https://doi.org/10.1021/acs.jpclett.9b01077) (2019). PMID: 31188606, <https://doi.org/10.1021/acs.jpclett.9b01077>.

336. Neukirch, A. J. *et al.* Geometry distortion and small polaron binding energy changes with ionic substitution in halide perovskites. *The J. Phys. Chem. Lett.* **9**, 7130–7136, DOI: [10.1021/acs.jpcllett.8b03343](https://doi.org/10.1021/acs.jpcllett.8b03343) (2018). <https://doi.org/10.1021/acs.jpcllett.8b03343>.
337. Schmidt, J., Marques, M. R. G., Botti, S. & Marques, M. A. L. Recent advances and applications of machine learning in solid-state materials science. *npj Comput. Mater.* **5**, 83, DOI: [10.1038/s41524-019-0221-0](https://doi.org/10.1038/s41524-019-0221-0) (2019).
338. Wang, C.-I., Braza, M. K. E., Claudio, G. C., Nellas, R. B. & Hsu, C.-P. Machine learning for predicting electron transfer coupling. *The J. Phys. Chem. A* **123**, 7792–7802, DOI: [10.1021/acs.jpca.9b04256](https://doi.org/10.1021/acs.jpca.9b04256) (2019). PMID: 31429287, <https://doi.org/10.1021/acs.jpca.9b04256>.
339. Birschitzky, V., Reticcioli, M. & Franchini, C. *Polaron Configurational Energies using Machine Learning*. Master's thesis, University of Vienna (2020).
340. Behler, J. & Parrinello, M. Generalized neural-network representation of high-dimensional potential-energy surfaces. *Phys. Rev. Lett.* **98**, 146401, DOI: [10.1103/PhysRevLett.98.146401](https://doi.org/10.1103/PhysRevLett.98.146401) (2007).
341. Westermayr, J., Faber, F. A., Christensen, A. S., von Lilienfeld, O. A. & Marquetand, P. Neural networks and kernel ridge regression for excited states dynamics of CH_2NH_2^+ : From single-state to multi-state representations and multi-property machine learning models (2019). [1912.08484](https://arxiv.org/abs/1912.08484).
342. Jinnouchi, R., Karsai, F. & Kresse, G. On-the-fly machine learning force field generation: Application to melting points. *Phys. Rev. B* **100**, 014105, DOI: [10.1103/PhysRevB.100.014105](https://doi.org/10.1103/PhysRevB.100.014105) (2019).
343. Laanait, N., Ziatdinov, M., He, Q. & Borisevich, A. Identifying local structural states in atomic imaging by computer vision. *Adv. Struct. Chem. Imaging* **2**, 14, DOI: [10.1186/s40679-016-0028-8](https://doi.org/10.1186/s40679-016-0028-8) (2016).
344. Ziatdinov, M. *et al.* Deep analytics of atomically-resolved images: manifest and latent features. *arXiv preprint arXiv:1801.05133* (2018).
345. Pielmeier, F. & Giessibl, F. J. Spin resolution and evidence for superexchange on $\text{NiO}(001)$ observed by force microscopy. *Phys. Rev. Lett.* **110**, 266101 (2013).
346. Tan, G., Zhao, L.-D. & Kanatzidis, M. G. Rationally designing high-performance bulk thermoelectric materials. *Chem. Rev.* **116**, 12123–12149 (2016).
347. Biswas, S., Wallentine, S., Bandaranayake, S. & Baker, L. R. Controlling polaron formation at hematite surfaces by molecular functionalization probed by XUV reflection-absorption spectroscopy. *The J. Chem. Phys.* **151**, 104701, DOI: [10.1063/1.5115163](https://doi.org/10.1063/1.5115163) (2019). <https://doi.org/10.1063/1.5115163>.

Acknowledgements

We thank the Erwin Schrödinger Institute (ESI) for hosting the ESI-CECAM workshop "Polarons in the 21st Century and all participants for the many enlightening discussions. CF acknowledges support by the Austrian Science Fund (FWF) projects No. I 2460 and I 4506, and the many enriching discussions with the project partners J. Tempere, G. Kresse, S. Klimin and J. Devreese. MS acknowledges support by the Czech Science Foundation (GAČR 20-21727X) and GAUK Primus/20/SCI/009. UD acknowledges support by the Austrian Science Fund FWF (Wittgenstein Prize Z-250).

Author contributions

All authors contributed equally to the writing of the manuscript.

Competing interests

The authors have no competing interests.